이학박사 학위논문

Optical properties and interaction effects of Dirac materials

디락 물질의 광학적 특성 및 상호작용 효과 연구

2018년 2월

서울대학교 대학원

물리천문학부

안 성 진

Abstract

Topological semimetals with point or line band touchings have emerged as a new frontier in condensed matter study. Electrons near touching points behave as massless Dirac fermions, and thus they exhibit many fascinating and exotic properties. Motivated by this, this thesis is devoted to studying the physics of such Dirac materials.

We begin by investigating optical behaviors of nodal line and multi-Weyl semimetals. For nodal line semimetals, we find that the low-frequency conductivity has a rich spectral structure which can be understood using scaling rules derived from the geometry of the Fermi surface. For multi-Weyl semimetals, we show that the frequency dependence of optical conductivities obeys scaling relations that are derived from the winding number. For both of these materials, we discuss possible experimental implications of our results, suggesting that they can serve as a guidance for optical experiments.

Then we turn to interaction-induced phenomena, particularly focusing on collective modes and their couplings with phonons. We first study plasmon modes in multi-Weyl semimetals within random approximation approximation. We find that chirality-induced interband transitions redshift plasma frequencies. As a result, plasmons in multi-Weyl semimetals remain undamped over a broad range of density and interaction strength. Then, we investigate the coupling between plasmons and the surface polar phonons of the underlying substrate through the long-range polar Fröhlich interaction. We find that the strong coupling between the SO phonon and the plasmon leads to a new decay channel for the quasiparticles through the emis-

sion of the coupled mode and gives rise to an abrupt increase in the scattering rate, which is absent in the uncoupled system.

Keywords: optical conductivity, plasmon, plasmon-phonon coupling, graphene, Weyl semimetal, multi-Weyl semimetal, nodal line semimetal
Student Number: 2012-20369

Contents

List of Figures

Chapter 1

Introduction

In the last decade, topological states of matter have emerged as a promising field of research, bringing novel concepts in modern condensed matter physics. While most phenomena in condensed matter systems are well captured by classical or semiclassical approaches, topological phenomena are purely quantum mechanical because they arise from the topological nature of the Bloch wave functions. The topology encoded in the quantum mechanical wavefunctions is characterized by the topological invariant, which is usually related to a physical observable. The well-known example of topological phase of matter is a two-dimensional quantum Hall systems, whose topological invariant is characterized the Chern number. In quantum Hall systems, chiral states propagate at the edge due to a topologically non-trivial electronic structure and are robust against disorders because the topological invariant does not change under adiabatic deformations of the system.

In 2005, Kane and Mele proposed the quantum spin-Hall insulator (QSHI) which can be viewed as two copies of quantum Hall systems with opposite Chern number and spin[1]. The QSHI is characterized by a spin-orbit induced bulk gap and two

counter-propagating chiral edge states related by time reversal symmetry. The chiral edge states are protected and robust against disorders unless the time reversal symmetry is broken. Remarkably, the quantum spin hall phase is characterized by a Z_2 topological invariant, which is an analogue to the Chern number of the quantum Hall effect. This indicates a new class of topological materials, which is distinguished from normal insulators with a trivial topological invariant. Since the discovery of QSHI, the field of topological insulator has exploded in condensed matter physics.

Interest in topological states of quantum matter has led to the identification of new gapless topological electronic states that can also support topological phases, i.e., topological semimetals. In topological semimetals, the conduction and valence bands contact at points or lines in momentum space, and the band degeneracy at the contact is protected by symmetries such as crystalline and time-reversal symmetries. Among the topological semimetals, Dirac semimetals have degenerate conduction and valence bands which touch at discrete points, which are dubbed Dirac point. Near a Dirac point, electrons in Dirac semimetals behave as massless Dirac fermions. If either time reversal or inversion symmetry is broken, the Dirac point is split into two Weyl nodes. Weyl nodes themselves are topological objects characterized by the winding number and act as a magnetic monopole for the Berry curvature in three dimensional momentum space. When two Weyl nodes with the same monopole charge merge, a new type of Weyl semimetals arises, which are referred as multi-Weyl semimetals[2–4]. These materials are characterized by double (triple) Weyl-nodes in which the band dispersion is anisotropic and the chirality is given by a multiple integer number. In nodal line semimetals, the two bands cross on closed lines in momentum space. A nodal line can be thought of as a collection of two dimensional Dirac points and is associated with many topological phenomena unseen in classical semimetals [5–8]. Such recent developments in topological semimetals provide condensed matter realizations of Dirac physics, which has recently been of

great interest in the field of both condensed matter and high energy physics.

Due to a surge of interest in topological semimetals, recently there have been many efforts into experimentally identifying them using spectroscopic techniques such as angle-resolved photoemission spectroscopy (ARPES), scanning tunneling microscope (STM) and optical absorption spectroscopy [9–27].

Among those spectroscopic techniques, optical spectroscopy is particularly easy to implement and thus has some comparable advantages over other methods. In this regard, this thesis first explores the optical properties of topological semimetals with point and line nodes, particularly focusing on their characteristic behaviors that can serve as a guidance and useful information for optical experiments.

Secondly, this thesis studies interacting phenomena in topological semimetals, which are expected to be distinguishable from those in normal semimetals due to its unique band and topologically non-trivial wavefunctions. In fact, the spin-momentum locking structure and unique band structures have been known to lead to important consequences in topological, transport and interaction-induced properties[28–36]. In this thesis, we first study the winding number dependence of plasmon modes in multi-Weyl semimetals. Then, we investigate the scattering mechanisms of quasiparticles in graphene due to a plasmon-phonon coupled mode.

The outline of the thesis is as follows.

In chapter 2, we introduce Dirac materials along with their electronic band structures and topological origin.

In chapter 3, we study the optical conductivity of nodal line semimetals in the presence of tilt. We show that geometrical changes in the phase space for interband transitions can cause qualitatively different optical behaviors.

In chapter 4, we study the optical response within a model containing multi-Weyl, quantum anomalous Hall and normal insulator phases. We show that the characteristic frequency dependence of multi-Weyl semimetals strongly depends on

the winding number.

In chapter 5, we study plasmon modes in multi-Weyl semimetals within random phase approximation. We show that chirality-induced interband transitions red-shifts plasma frequencies.

In chapter 6, we investigate quasiparticle scattering mechanisms in graphene systems in the presence of the coupling between electrons and surface optical phonons of the polar substrate. We find a new decay channel through the emission of the plasmon-phonon coupled mode.

In chapter 7, we will conclude this thesis by giving a summary

Chapter 2

Dirac physics in condensed matter

2.1 The Dirac Equation

The Schrödinger equation is not consistent with the special relativity since it treats space and time unequally: it contains a first order derivative in time and a second-order derivative in space. In an attempt to integrate quantum mechanics with special relativity, Paul Dirac proposed the Dirac equation in 1928, which is written as

$$(i\gamma^{\mu}\partial_{\mu} - m)\,\Psi = 0, \tag{2.1}$$

where m is mass, Ψ is a relativistic wave function, and γ^{μ} are the Gamma matrices satisfying the Dirac algebra $\{\gamma^{\mu}, \gamma^{\nu}\} = \gamma^{\mu}\gamma^{\nu} + \gamma^{\nu}\gamma^{\mu} = 2g^{\mu\nu} = diag(+ - - - -)$. In the Weyl representation, the gamma matrices are chosen as $\gamma_0 = \sigma_x \otimes I$ and $\gamma_i = i\sigma_y \otimes \sigma_i$, where σ_i are the Pauli matrices. In this representation, the Dirac equation reads as

$$\begin{pmatrix} -m & i(\partial_0 + \sigma^i\partial_i) \\ i(\partial_0 - \sigma^i\partial_i) & -m \end{pmatrix} \begin{pmatrix} \psi_{\mathrm{L}} \\ \psi_{\mathrm{R}} \end{pmatrix} = 0. \tag{2.2}$$

With $m = 0$, the Dirac equation can be decomposed into two independent equations for ψ_{L} and ψ_{R}: $i(\partial_0 + \sigma^i \partial_i)\psi_{\mathrm{R}} = 0$ and $i(\partial_0 - \sigma^i \partial_i)\psi_{\mathrm{L}} = 0$. These are Weyl equations and ψ_{R} and ψ_{L} are the left- and right-handed Weyl spinors, respectively. The chirality of Weyl spinors is obtained by the action of $\gamma_5 = -\sigma_z \otimes I$ on Weyl spinors, giving us the chirality $\chi = \pm 1$ for $\psi_{\substack{R \\ L}}$. Note that a massless Dirac fermion can be viewed as a superimposed of two independent Weyl spinors with opposite chirality.

2.2 Weyl nodes and band touching

Here we examine how Weyl or Dirac Fermions can arise in condensed matter systems. Let us first suppose that $\boldsymbol{k}_0$ is a point where the conduction and valance bands contact. The first order taylor expansion of the Hamiltonian around $\boldsymbol{k}_0$ is given by

$$H(\boldsymbol{k}) \approx f_0(\boldsymbol{k}_0) + \sum_{i=1}^{d} \partial_{\boldsymbol{k}} f_i(\boldsymbol{k})|_{\boldsymbol{k}=\boldsymbol{k}_0} \cdot (\boldsymbol{k} - \boldsymbol{k}_0)\sigma_i, \tag{2.3}$$

which is essentially the same as the Weyl Hamiltonian $H(\boldsymbol{k}) = \hbar v_F \boldsymbol{k} \cdot \boldsymbol{\sigma}$ with energy and momentum shifts, albeit distorted and anisotropic. This implies that around such a two band touching quasiparticles behave as Weyl Fermions, and thus it is called 'Weyl node'. Note that the two component Hamiltonian has pseudospin degrees of freedom in addition to spin. Defining pseudospin vectors $\boldsymbol{\sigma} = (\sigma_x, \sigma_y, \sigma_z)$, we can write the Hamiltonian as $H = v_F |\boldsymbol{k}| \, \hat{\boldsymbol{n}} \cdot \boldsymbol{\sigma}$, which indicates that the direction of pseudospin is coupled to the momentum, meaning that Weyl fermions carry chirality.

A natural question we can ask here is under what conditions Weyl nodes appear. Consider the following generic two band Hamiltonian,

$$H(\boldsymbol{k}) = \sum_{i=0}^{d} f_i(\boldsymbol{k})\sigma_i, \tag{2.4}$$

where d is the dimension of the system. The energy eigenvalues of the Hamiltonian

are

$$\varepsilon_{\pm}(\boldsymbol{k}) = f_0(\boldsymbol{k}) \pm \sqrt{\sum_{i=1}^{d} f_i(\boldsymbol{k})^2}, \tag{2.5}$$

where $+(-)$ represents the conduction (valance) band. The condition for the two bands to touch is given as $f_1(\boldsymbol{k}) = f_2(\boldsymbol{k}) = f_3(\boldsymbol{k}) = 0$. Thus the problem for finding a point degeneracy is reduced to solving three independent equations, requiring three tunable variables for the existence of solution. Two dimensional systems have only two momentum components that can serve as tunable variables, and thus stable contact points generally do not exist in two dimensional materials. When the system respects some symmetries, however, the number of constraints can be reduced, and the system can contain a Weyl node even in the two dimensional momentum space. A good example of this is graphene: the Dirac cone stays intact due to time reversal and inversion symmetries, which require $f_3(\boldsymbol{k}) = 0$ that plays a role as the mass term in the Dirac equation that lifts the point degeneracy and creates a gap. For three dimensional materials, there are three momentum components that can serve as tunable parameters, and thus stable contact points can be achieved without any additional symmetries.

2.3 Weyl nodes and symmetries

The time reversal operator flips the sign of the crystal momentum and conjugate the Hamiltonian, while the inversion operator only flips the crystal momentum. Thus, in the presence of both the time reversal and inversion symmetries, $H(\boldsymbol{k}) = H(-\boldsymbol{k}) = H^*(\boldsymbol{k})$. Applying this to a single node, we can immediately find that two Weyl nodes with the opposite chirality are degenerate when both the symmetries are present. As a consequence, there arises a Dirac node, whose Hamiltonian is described by the

4 by 4 matrix,

$$H(\boldsymbol{k}) = \begin{pmatrix} 0 & v_{\mathrm{F}}\boldsymbol{k}\cdot\boldsymbol{\sigma}^* \\ v_{\mathrm{F}}\boldsymbol{k}\cdot\boldsymbol{\sigma} & 0 \end{pmatrix}. \tag{2.6}$$

Note that the two Weyl nodes are susceptible to a perturbation in the form of $I\otimes\sigma_z$, which annihilates both the Weyl nodes via opening a gap. Thus for a Dirac node to be stable, some symmetries are required that prevent such gap-opening terms.

If either the time reversal symmetry or inversion symmetry is broken, the Dirac node is split into two Weyl nodes: when the time reversal symmetry is broken, the Dirac node is split into two Weyl pairs with the opposite chirality at $\pm\boldsymbol{k}_0$. This implies that the minimum number of Weyl nodes is two. On the other hand, when the inversion symmetry is broken, the Dirac node is split into two separate pairs with the same chirality at $\pm\boldsymbol{k}_0$. Since there should be the same number of left- and right-handed Weyl nodes, two additional Weyl nodes having the opposite chirality must exist. Thus there are at least four Weyl nodes in reversal breaking systems.

2.4 Weyl node as a source of Berry curvature

While discussing the minimum number of Weyl nodes in the previous section, we required the net chirality over the Brillouin zone to be zero. In fact, this is related to the topological aspect of Weyl nodes. The Berry curvature of a single Weyl node is written as

$$\boldsymbol{\Omega}(\boldsymbol{k}) = \frac{J}{2}\frac{\boldsymbol{k}}{|\boldsymbol{k}|^3}, \tag{2.7}$$

where $J = \pm 1$ denotes the chirality. The integral of the Berry curvature over a closed surface enclosing a Weyl node is a quantized Chern number, which is equal to the chirality:

$$C = \frac{1}{2\pi}\int \boldsymbol{\nabla}\cdot\boldsymbol{\Omega}(\boldsymbol{k})d\boldsymbol{k} = J\int \delta(\boldsymbol{k}-\boldsymbol{k}_0)d\boldsymbol{k} = J, \tag{2.8}$$

where we assume that the Weyl node is located at $\boldsymbol{k}_0$. This quantity serves as a topological invariant of Weyl nodes. In analogy to electrodynamics, the Berry

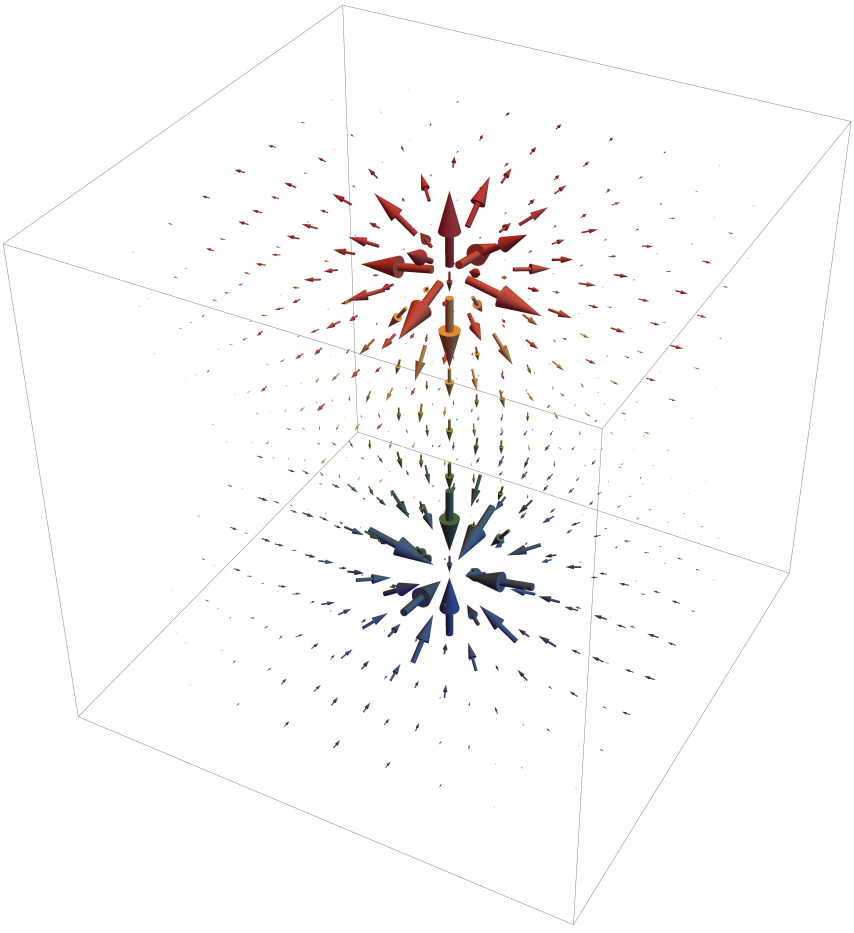

Figure 2.1 Berry curvature vectors of two Weyl nodes with opposite chirality in momentum space. Note that they flow from the Weyl node with positive chirality (red) to the one with negative chirality (blue).

curvature and Weyl nodes can be viewed as a magnetic field and magnetic monopoles in momentum space, respectively. Thus, a Weyl nodes act as sources or sinks of the Berry curvature and carries a topological charge equal to its chirality. This implies that Weyl nodes must appear in pairs for the flux of the Berry curvature to be non-divergent.

2.5 multi-Weyl node

Weyl nodes are robust against small adiabatic perturbations due to their topological nature. Merging two Weyl nodes, however, can modify the node structure and thus produce new types of Weyl semimetal. Among them are multi-Weyl semimetals[2, 3], which are produced by merging two Weyl nodes with the same chirality. In these states, the merger of the nodes is robust if it is protected by a point group symmetry. The low energy dispersion can then be characterized by double (triple) Weyl nodes with linear dispersion along one symmetry direction and quadratic (cubic) dispersion along the remaining two directions.

The low-energy effective Hamiltonian for multi-Weyl semimetals of order J near a single Weyl point can be described by the Hamiltonian:

$$H_J = \varepsilon_0 \left(\tilde{k}_-^J \sigma_+ + \tilde{k}_+^J \sigma_- \right) + \hbar v_z k_z \sigma_z, \tag{2.9}$$

where $\tilde{k}_\pm = k_\pm / k_0$ with $k_\pm = k_x \pm i k_y$, $\sigma_\pm = \frac{1}{2}(\sigma_x \pm i\sigma_y)$, and $\boldsymbol{\sigma}$ are Pauli matrices acting in the space of two bands that make contact at the Weyl point. Here, v_z is the effective velocity along the k_z direction, and k_0 and ε_0 are material dependent parameters in units of momentum and energy, respectively. For simplicity, we assumed the axial symmetry around the k_z-axis. Note that the eigenenergies of the Hamiltonian are given by $\varepsilon_\pm = \pm\sqrt{\varepsilon_0^2 \tilde{k}_\parallel^{2J} + (\hbar v_z k_z)^2}$ where $\tilde{k}_\parallel = \sqrt{\tilde{k}_x^2 + \tilde{k}_y^2}$, and the in-plane energy dispersion is characterized by J. Thus the winding number determines not only the topological nature of the wave function but also the anisotropic

energy dispersion of the system.

Chapter 3

Optical conductivity of nodal line semimetals

3.1 Introduction

When a nodal line is protected by a mirror symmetry, such a nodal line is "flat" in the sense that it lies in a single plane in $\boldsymbol{k}$ space. However, the contact line is not similarly constrained to occur on a constant energy surface. An energy dispersion on the nodal line has no effect on its topological character, which is determined by the phase winding of the Bloch states around the singularity. However it generically forces the system into a semimetallic state with coexisting electron and hole pockets and an unconventional Fermi surface (FS) geometry, exhibiting the rich structures of Dupin cyclide geometries [37], as shown in Fig. 3.1. Here the geometry of the FS is determined by a combination of the energy dispersion of the contact line (tilt) and the Fermi energy which play a crucial role in determining various physical properties in nodal line semimetals (NLSMs).

The optical conductivity of a low-energy model for a NLSM in the absence of tilt

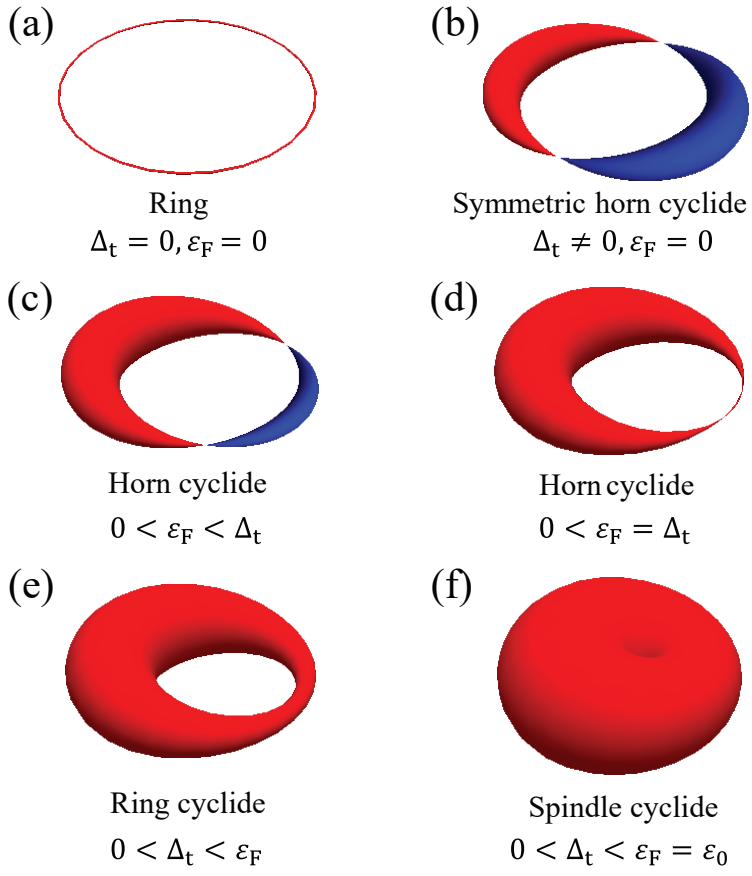

Figure 3.1 Evolution of the Fermi surface (FS) as a function of tilt Δ_t and Fermi energy ε_F with red (blue) indicating the electron (hole) pocket. (a) At zero Fermi energy with zero tilt, the FS has a one-dimensional ring shape sitting on the zero-energy plane. (b) With a finite tilt, the ring shape evolves into a symmetric horn cyclide containing both electron and hole pockets symmetrically, which vanish at two contact points. Upon increasing the Fermi energy, the electron and hole pockets (c) become asymmetric and the contact points move out from the symmetrical axis, (d) converge into a single point when the Fermi energy equals the tilt energy, and (e) vanish when the Fermi energy becomes larger than the tilt energy. (f) When the Fermi energy equals the energy scale of the ring radius, the FS is merged into a spherelike shape with no holes in the center, similar to that of Weyl semimetals.

has recently been studied [38]. However, once an energy tilt is introduced, there is a competition between two energy scales set by the amount of dispersion and by the chemical potential. In this chapter, we study the consequences of this competition for the low-frequency conductivity of a NLSM and analyze its characteristic frequency dependence using the geometry of the Dupin cyclide. We find new spectral features that occur as a result of its unconventional geometry. For a nonzero Fermi energy smaller than the tilt energy scale, full Pauli blocking is prevented and instead all three diagonal components of the optical conductivity tensor show linear scaling with frequency. For the Fermi energy larger than the tilt energy, the interband optical conductivity recovers a gap due to Pauli blocking. We find nonanalytic features in both the frequency dependence of the interband conductivity and the chemical potential dependence of the Drude stiffness which arises from Lifshitz transitions of the FS.

3.2 Model

In the continuum approximation, the minimal Hamiltonian for tilted NLSMs that captures the essential features of its low-energy excitations takes the form of a 2 by 2 matrix given by [39, 40]

$$H = \hbar v q_\rho \sigma_x + \hbar v k_z \sigma_y + \hbar \boldsymbol{v}_\mathrm{t} \cdot \boldsymbol{k} \sigma_0, \tag{3.1}$$

where σ_x and σ_y are the Pauli matrices, σ_0 is the identity matrix, $\boldsymbol{v}_\mathrm{t}$ is the tilt velocity, $q_\rho = k_\rho - k_0$, $k_\rho = \sqrt{k_x^2 + k_y^2}$, and k_0 is the radius of the nodal ring. The eigenenergies of the Hamiltonian are given by

$$\varepsilon_\pm(\boldsymbol{k}) = \pm \hbar v \sqrt{q_\rho^2 + k_z^2} + \hbar \boldsymbol{v}_\mathrm{t} \cdot \boldsymbol{k}, \tag{3.2}$$

which has a ring shape zero-energy contour with a slope of $\boldsymbol{v}_\mathrm{t}$. In the following, we consider tilt only in the in-plane direction because it produces electron-hole pockets,

leading to qualitative changes in the optical conductivity, whereas tilt along the perpendicular axis has little effect on the optical conductivity unless it is so extreme that the system is in a type-II semimetallic state. Without the loss of generality, we therefore set $\boldsymbol{v}_{\rm t} = v_{\rm t}\hat{x}$.

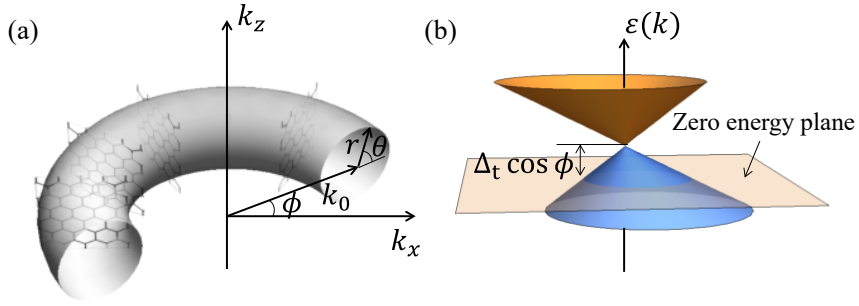

Figure 3.2 (a) Schematic illustration of toroidal coordinates and graphene sheets standing perpendicular to the nodal-line plane. (b) The Dirac cone energy dispersion of the graphene sheet located at ϕ. cone is shifted from the zero energy by $\Delta_{\rm t}\cos\phi$.

Let us consider the following coordinate transformation

$$\begin{aligned} k_x &\to (k_0 + r\cos\theta)\cos\phi, \\ k_y &\to (k_0 + r\cos\theta)\sin\phi, \\ k_z &\to r\sin\theta. \end{aligned} \tag{3.3}$$

Here, the Jacobian is given by $\mathcal{J}(r,\theta) = r(k_0 + r\cos\theta)$. In this coordinate, the NLSM Hamiltonian Eq.(3.1) is transformed into

$$H = \varepsilon_0 \begin{pmatrix} 0 & \tilde{r}e^{-i\theta} \\ \tilde{r}e^{i\theta} & 0 \end{pmatrix} + \Delta_{\rm t}(1 + \tilde{r}\cos\theta)\cos\phi\sigma_0, \tag{3.4}$$

where $\tilde{r} = r/k_0$, $\varepsilon_0 = \hbar v k_0$, and $\Delta_{\rm t} = \hbar v_{\rm t} k_0$. Remarkably, in toroidal coordinates, this NLSM Hamiltonian in Eq. (3.1) is written in the same form as the low-energy graphene Hamiltonian, but expressed in polar coordinates (r, θ) centered at $\boldsymbol{k}_0$ [see

Fig. 3.2(a)]. Thus, in the energy range where the toroidal structure is maintained, we can consider NLSMs as a collection of graphene sheets with tilt in the x direction and the Dirac point shifted from zero energy by $\Delta_{\rm t}\cos\phi$ [see Fig. 3.2(b)].

3.3 Optical conductivity obtained from a collection of graphene sheets

In the linear response limit, we can obtain the optical conductivity of NLSMs by summing up individual contributions from each of the graphene sheets:

$$\sigma_{ii}^{\rm NLSM} = k_0 \int_0^{2\pi} \frac{d\phi}{2\pi}\, \sigma^{\rm gr}(\phi)\mathcal{F}_{ii}(\phi), \tag{3.5}$$

where $i = x, y, z$, $\sigma^{\rm gr}(\phi)$ is the optical conductivity of a graphene sheet located at ϕ with tilt in the x direction, and $\mathcal{F}_{xx}(\phi) = \cos^2\phi$, $\mathcal{F}_{yy}(\phi) = \sin^2\phi$, $\mathcal{F}_{zz}(\phi) = 1$ are geometric factors from the projection of an external electric field on the graphene sheet and that of the in-plane velocity of graphene on the current direction. Note that Eq. (3.5) is valid for $\hbar\omega < 2\varepsilon_0$ where the toroidal structure is maintained.

First, consider the case of $\Delta_{\rm t} = 0$. Since the optical conductivity from a single Dirac cone filled to energy $\varepsilon_{\rm F}$ is given by $\sigma^{\rm gr}(\phi) = \frac{e^2}{16\hbar}\Theta\left(\hbar\omega - 2|\varepsilon_{\rm F}|\right)$ [41], the optical conductivity of the NLSM is

$$\frac{\sigma_{ii}}{\sigma_0} \approx \begin{cases} \frac{1}{2}\Theta\left(\hbar\omega - 2|\varepsilon_{\rm F}|\right) & \text{for } i = x, y, \\ \Theta\left(\hbar\omega - 2|\varepsilon_{\rm F}|\right) & \text{for } i = z, \end{cases} \tag{3.6}$$

where $\sigma_0 = \frac{e^2 k_0}{16\hbar}$. Thus, for $\hbar\omega < 2|\varepsilon_{\rm F}|$ the optical conductivity vanishes due to Pauli blocking, whereas for $2|\varepsilon_{\rm F}| < \hbar\omega < 2\varepsilon_0$, it remains constant [38].

For $\Delta_{\rm t} \neq 0$, the conductivity should be modified to take into account (i) the shift of the Dirac point from zero energy [first term of σ_0 in Eq. (3.4)] and (ii) the tilted linear band dispersion (second term). At low frequencies ($\hbar\omega \ll \varepsilon_0$), however, when the Dirac points lie close to zero energy, the tilt in the band disper-

sion is negligible. Thus, $\sigma_{ii}(\omega)$ at low frequencies can be obtained using $\sigma^{\rm gr}(\phi) \approx \frac{e^2}{16\hbar}\Theta\left(\hbar\omega - 2|\varepsilon_{\rm F} - \Delta_{\rm t}\cos\phi)|\right)$ in Eq. (3.5), giving

$$\frac{\sigma_{ii}}{\sigma_0} \approx \int_0^{2\pi} \frac{d\phi}{2\pi}\,\Theta(\hbar\omega - 2\,|\varepsilon_{\rm F} - \Delta_{\rm t}\cos\phi|)\mathcal{F}_{ii}(\phi). \tag{3.7}$$

3.4 Kubo formula for optical conductivity

In thie section, we present the Kubo formula for the optical conductivity and derive the low frequency asymptotic expressions directly from the Kubo formula. In the linear response and non-interacting limit, the optical conductivity can be calculated by using the Kubo Formula[42]:

$$\sigma_{ij}(\omega) = -\frac{ie^2}{\hbar}\sum_{s,s'}\int \frac{d^3k}{(2\pi)^3}\frac{f_{s,\boldsymbol{k}} - f_{s',\boldsymbol{k}}}{\varepsilon_{s,\boldsymbol{k}} - \varepsilon_{s',\boldsymbol{k}}}\frac{M_i^{ss'}(\boldsymbol{k})M_j^{s's}(\boldsymbol{k})}{\hbar\omega + \varepsilon_{s,\boldsymbol{k}} - \varepsilon_{s',\boldsymbol{k}} + i0^+}, \tag{3.8}$$

where $i,j = x,y,z$, $\varepsilon_{s,\boldsymbol{k}}$ and $f_{s,\boldsymbol{k}} = 1/[1 + e^{(\varepsilon_{s,\boldsymbol{k}}-\mu)/k_{\rm B}T}]$ are the eigenenergy and the Fermi distribution function for the band index $s = \pm$ and wave vector $\boldsymbol{k}$, respectively, μ is the chemical potential and $M_i^{ss'}(\boldsymbol{k}) = \langle s,\boldsymbol{k}|\hbar\hat{v}_i|s',\boldsymbol{k}\rangle$ with the velocity operator $\hat{v}_i = \frac{1}{\hbar}\frac{\partial\hat{H}}{\partial k_i}$. We can separate the real part of the longitudinal optical conductivity to the intraband and interband contributions:

$$\sigma_{ii}^{\rm intra}(\omega) = -\frac{\pi e^2}{\hbar}\sum_{s=\pm}\int \frac{d^3k}{(2\pi)^3}\frac{\partial f_{s,\boldsymbol{k}}}{\partial\varepsilon_{s,\boldsymbol{k}}}|M_i^{ss}(\boldsymbol{k})|^2\delta(\hbar\omega), \tag{3.9}$$

$$\sigma_{ii}^{\rm inter}(\omega) = -\frac{\pi e^2}{\hbar}\int \frac{d^3k}{(2\pi)^3}\frac{f_{-,\boldsymbol{k}} - f_{+,\boldsymbol{k}}}{\varepsilon_{-,\boldsymbol{k}} - \varepsilon_{+,\boldsymbol{k}}}|M_i^{-+}(\boldsymbol{k})|^2\delta(\hbar\omega + \varepsilon_{-,\boldsymbol{k}} - \varepsilon_{+,\boldsymbol{k}}). \tag{3.10}$$

In the following we obtain the optical conductivity of NLSMs in the absence of tilt at zero Fermi energy. We show that for $\hbar\omega < 2\varepsilon_0$ the results are in agreement with those obtained by averaging graphene optical conductivities [Eq. (3.6)], whereas for $\hbar\omega > 2\varepsilon_0$ the optical conductivity of NLSMs shows linear frequency dependence as Weyl semimetal at high frequencies. In cylindrical coordinates ($k_x \to \rho\cos\phi$, $k_y \to \rho\sin\phi$), the eigenenergies of NLSMs are given by $\varepsilon_\pm(\rho,\phi,k_z) = \pm\hbar v\sqrt{k_z^2 + (\rho - k_0)^2}$

and the interband matrix elements are calculated to be

$$M_x^{-+}(\theta,\phi) = -i\hbar v\frac{k_z\cos\phi}{\sqrt{k_z^2+(\rho-k_0)^2}}, \tag{3.11}$$

$$M_z^{-+}(\theta,\phi) = -i\hbar v\frac{\rho-k_0}{\sqrt{k_z^2+(\rho-k_0)^2}}. \tag{3.12}$$

By inserting these into Eq. (B.3), we obtain

$$\sigma_{xx}^{\rm inter}(\omega) = \frac{1}{2}\sigma_0\left\{\Theta(2-\widetilde{\omega})+\Theta(\widetilde{\omega}-2)\left[A(\omega)\left(1+\frac{2}{\widetilde{\omega}^2}\right)+B(\omega)\right]\right\}, \tag{3.13}$$

and

$$\sigma_{zz}^{\rm inter}(\omega) = \sigma_0\left\{\Theta(2-\widetilde{\omega})+\Theta(\widetilde{\omega}-2)\left[2A(\omega)\left(1-\frac{1}{\widetilde{\omega}^2}\right)+B(\omega)\right]\right\}, \tag{3.14}$$

where $A(\omega)=\frac{1}{3\pi}\sqrt{\widetilde{\omega}^2-4}$, $B(\omega)=\frac{1}{2}+\frac{1}{\pi}\tan^{-1}\left(\frac{2}{\sqrt{\widetilde{\omega}^2-4}}\right)$, $\sigma_0=\frac{e^2k_0}{16\hbar}$ and $\widetilde{\omega}=\hbar\omega/\varepsilon_0$. Note that the optical conductivity is constant for $\hbar\omega<2\varepsilon_0$, and begins to increase at $\hbar\omega=2\varepsilon_0$. In the high frequency limit, $\sigma_{xx}^{\rm inter}(\omega)\approx\frac{e^2}{96\hbar v}\omega$ and $\sigma_{zz}^{\rm inter}(\omega)\approx\frac{e^2}{24\hbar v}\omega$, showing linear behaviors as Weyl semimetals.

In the following, we show derivations of the low frequency analytical expressions of the optical conductivity in the presence of tilt and Fermi energy. For obtaining low frequency asymptotic expressions, it is not convenient to use cylindrical coordinates because the band structure appearing in the low-energy regime has a torus-like shape. Thus, we use the toroidal coordinates for the derivation of low frequency asymptotic forms.

The eigenenergies and eigenstates of the Hamiltonian of NLSMs in toroidal coordinates are given by $\varepsilon_\pm(r,\theta,\phi)=\pm\varepsilon_0\tilde{r}+\Delta_t(1+\tilde{r}\cos\theta)\cos\phi$ where $\tilde{r}=r/k_0$ and $|\pm,\boldsymbol{k}\rangle=\frac{1}{\sqrt{2}}(\pm1,e^{i\phi})^{\rm T}$, respectively. The velocity matrices are expressed as $\hat{v}_x=\cos\phi\ \sigma_x$, $\hat{v}_y=\sin\phi\ \sigma_x$, and $\hat{v}_z=\sigma_y$. It follows that the interband matrix

elements used in the optical conductivity are

$$M_x^{-+}(\theta,\phi) = -i\hbar v\sin\theta\cos\phi, \tag{3.15}$$

$$M_y^{-+}(\theta,\phi) = -i\hbar v\sin\theta\sin\phi, \tag{3.16}$$

$$M_z^{-+}(\theta,\phi) = i\hbar v\cos\theta. \tag{3.17}$$

By inserting these into Eq. (B.3), we can obtain the interband part of the optical conductivity at zero temperature:

$$\begin{aligned}\sigma_{ii}^{\rm inter}(\omega) &= \frac{\pi e^2}{\hbar}\int_0^{k_0} dr\int_0^{2\pi} d\theta\int_0^{2\pi} d\phi\frac{\mathcal{J}(r,\theta)}{(2\pi)^3}\frac{\mathcal{A}(\tilde{r},\theta,\phi)}{2\varepsilon_0\tilde{r}} \\ &\quad\times|M_i^{-+}(\theta,\phi)|^2\delta(\hbar\omega-2\varepsilon_0\tilde{r}) \\ &= \sigma_0 I_i(\omega),\end{aligned} \tag{3.18}$$

where $\widetilde{M}_i^{-+}(\theta,\phi)=M_i^{-+}(\theta,\phi)/(\hbar v)$ and $\mathcal{A}(\tilde{r},\theta,\phi)=\Theta\left[\varepsilon_F-\varepsilon_-(r,\theta,\phi)\right]-\Theta\left[\varepsilon_F-\varepsilon_+(r,\theta,\phi)\right]$ is the difference between the Fermi distribution functions (i.e., $f_{-,\boldsymbol{k}}-f_{+,\boldsymbol{k}}$) at zero temperature, which determines the integral area. Here $\hbar\omega<2\varepsilon_0$ is assumed, and

$$\begin{aligned}I_i(\omega) &= \frac{1}{2\pi^2}\int_0^{2\pi} d\theta\left(1+\frac{\hbar\omega}{2\varepsilon_0}\cos\theta\right)\int_0^{2\pi} d\phi\,\mathcal{A}\left(\frac{\hbar\omega}{2\varepsilon_0},\theta,\phi\right)\left|\widetilde{M}_i^{-+}(\theta,\phi)\right|^2 \\ &= \frac{1}{2\pi^2}\int_0^{2\pi} d\theta\left(1+\frac{\hbar\omega}{2\varepsilon_0}\cos\theta\right)\sum_{s=\pm}\int_{s\phi_{-s}(\theta,\omega)}^{s\phi_s(\theta,\omega)} d\phi\left|\widetilde{M}_i^{-+}(\theta,\phi)\right|^2 \\ &= \frac{1}{\pi^2}\int_0^{2\pi} d\theta\left(1+\frac{\hbar\omega}{2\varepsilon_0}\cos\theta\right)\int_{\phi_-(\theta,\omega)}^{\phi_+(\theta,\omega)} d\phi\left|\widetilde{M}_i^{-+}(\theta,\phi)\right|^2,\end{aligned} \tag{3.19}$$

where $\phi_\pm(\omega)=\cos^{-1}\left[\frac{\varepsilon_F\mp\frac{\hbar\omega}{2}}{\Delta_t\left(1+\frac{\hbar\omega}{2\varepsilon_0}\cos\theta\right)}\right]$. In the last line, we used $\left|\widetilde{M}_i^{-+}(\theta,\phi)\right|^2=\left|\widetilde{M}_i^{-+}(\theta,-\phi)\right|^2$.

Assuming $\varepsilon_F<\Delta_t$, we can expand $\phi_\pm(\theta,\omega)$ around $\omega=0$ as $\phi_\pm(\theta,\omega)\approx\phi_0+\Delta_\pm(\theta,\omega)$ where $\phi_0=\cos^{-1}\left(\frac{\varepsilon_F}{\Delta_t}\right)$ and

$$\Delta_\pm(\theta,\omega)=\pm\frac{\varepsilon_0\pm\varepsilon_F\cos\theta}{2\sqrt{\Delta_t^2-\varepsilon_F^2}}\frac{\hbar\omega}{2\varepsilon_0}. \tag{3.20}$$

Thus, at low frequencies $I_i(\omega)$ is calculated to be

$$I_i(\omega) \approx \frac{1}{\pi^2}\int_0^{2\pi} d\theta \left(1+\frac{\hbar\omega}{2\varepsilon_0}\cos\theta\right)\int_{\Delta_-(\theta,\omega)}^{\Delta_+(\theta,\omega)} d\phi \left|\widetilde{M}_i^{-+}(\theta,\phi+\phi_0)\right|^2. \quad (3.21)$$

Note that the integral range of ϕ is $\Delta_-(\theta,\omega) < \phi < \Delta_+(\theta,\omega)$ and $\Delta_\pm(\theta,\omega) \propto \hbar\omega$ is small at low frequencies, thus the integrand can be expanded around $\phi = 0$. For $I_x(\omega)$, $\left|\widetilde{M}_x^{-+}(\theta,\phi)\right|^2 = \sin^2\theta\cos^2\phi$ thus we can obtain

$$\begin{aligned} I_x(\omega) &= \frac{1}{\pi^2}\int_0^{2\pi} d\theta \left(1+\frac{\hbar\omega}{2\varepsilon_0}\cos\theta\right)\int_{\Delta_-(\theta,\omega)}^{\Delta_+(\theta,\omega)} d\phi\, \sin^2\theta\cos^2(\phi+\phi_0) \\ &\approx \frac{1}{\pi^2}\int_0^{2\pi} d\theta \left(1+\frac{\hbar\omega}{2\varepsilon_0}\cos\theta\right)\sin^2\theta \\ &\quad \times\int_{\Delta_-(\theta,\omega)}^{\Delta_+(\theta,\omega)} d\phi \left[\cos^2\phi_0 - \sin(2\phi_0)\phi - \cos(2\phi_0)\phi^2\right] \\ &\approx \frac{\left(\frac{\varepsilon_F}{\Delta_t}\right)^2}{\sqrt{1-\left(\frac{\varepsilon_F}{\Delta_t}\right)^2}}\frac{\hbar\omega}{\pi\Delta_t}. \end{aligned} \quad (3.22)$$

Similarly, at low frequencies we can obtain the remaining components of the optical conductivity in units of σ_0 as

$$I_y(\omega) \approx \sqrt{1-\left(\frac{\varepsilon_F}{\Delta_t}\right)^2}\frac{\hbar\omega}{\pi\Delta_t}, \quad (3.23)$$

$$I_z(\omega) \approx \frac{1}{\sqrt{1-\left(\frac{\varepsilon_F}{\Delta_t}\right)^2}}\frac{\hbar\omega}{\pi\Delta_t}. \quad (3.24)$$

Note that for $\varepsilon_F = 0$, $\phi_0 = \frac{\pi}{2}$ and thus $I_x(\omega)$ is written as

$$\begin{aligned} I_x(\omega) &\approx \frac{1}{\pi^2}\int_0^{2\pi} d\theta \left(1+\frac{\hbar\omega}{2\varepsilon_0}\cos\theta\right)\sin^2\theta\int_{\Delta_-(\theta,\omega)}^{\Delta_+(\theta,\omega)} d\phi\, \phi^2 \\ &\approx \frac{1}{12\pi^3}\left(\frac{\hbar\omega}{\Delta_t}\right)^3. \end{aligned} \quad (3.25)$$

3.5 Optical conductivity with $\varepsilon_F = 0$

In this section, we show that the low frequency asymptotic forms obtained in the previous section can also be derived from Eq. (3.7). In addition, we analyze the

results by investigating the geometry of the phase space (PS) for interband transitions. Here, the PS for interband transitions is given by the intersection between the outside of the FS and the PS allowed by energy conservation.

For a given frequency ω, the PS for NLSMs allowed by energy conservation is the surface of the momentum space torus which satisfies $\hbar\omega = \varepsilon_+(\boldsymbol{k}) - \varepsilon_-(\boldsymbol{k})$ We first consider the case where $\varepsilon_{\rm F} = 0$ in the presence of tilt. Figures 3.3(a) and 3.3(b) show calculated optical conductivities with tilt energies of $\Delta_{\rm t} = 0.3\varepsilon_0$ and $\Delta_{\rm t} = 0.6\varepsilon_0$, respectively. Note that the optical conductivities show kink structures at transitions between different frequency domains (I, II and III) and characteristic frequency dependences determined by the tilt energies.

In region I, the optical conductivity in the tilt direction is $\sigma_{xx} \propto \omega^3$ at low frequencies while those in the other directions (σ_{yy} and σ_{zz}) are $\propto \omega$ [see region I in Figs. 3.3(a) and 3.3(b)]. Figures 3.3(c) and 3.3(d) show the corresponding PS for interband transitions, which is divided into two separated islands located at $\phi = \pm\frac{\pi}{2}$. As demonstrated above in Eq. (3.7), we can express the optical conductivity by averaging contributions from the graphene sheets that occupy these two isolated regions. In the low-frequency limit, in the vicinity of the contact points, the optical conductivity is approximately given by

$$\begin{aligned} \frac{\sigma_{ii}}{\sigma_0} &\approx \int_{\phi\sim\pm\frac{\pi}{2}} \frac{d\phi}{2\pi}\, \Theta(\hbar\omega - 2\left|\Delta_{\rm t}\cos\phi\right|)\mathcal{F}_{ii}(\phi) \\ &\approx \frac{2}{\pi}\int_0^{\frac{\hbar\omega}{2\Delta_{\rm t}}} d\phi\, \mathcal{F}_{ii}\left(\phi+\frac{\pi}{2}\right). \end{aligned} \tag{3.26}$$

With the expansion of $\mathcal{F}_{ii}\left(\phi+\frac{\pi}{2}\right)$ around $\phi = 0$, the resulting conductivities in the lowest order are

$$\frac{\sigma_{ii}}{\sigma_0} = \begin{cases} \frac{1}{12\pi}\left(\frac{\hbar\omega}{\Delta_{\rm t}}\right)^3 & \text{for } i = x, \\ \frac{\hbar\omega}{\pi\Delta_{\rm t}} & \text{for } i = y, z, \end{cases} \tag{3.27}$$

which agree with our numerical results.

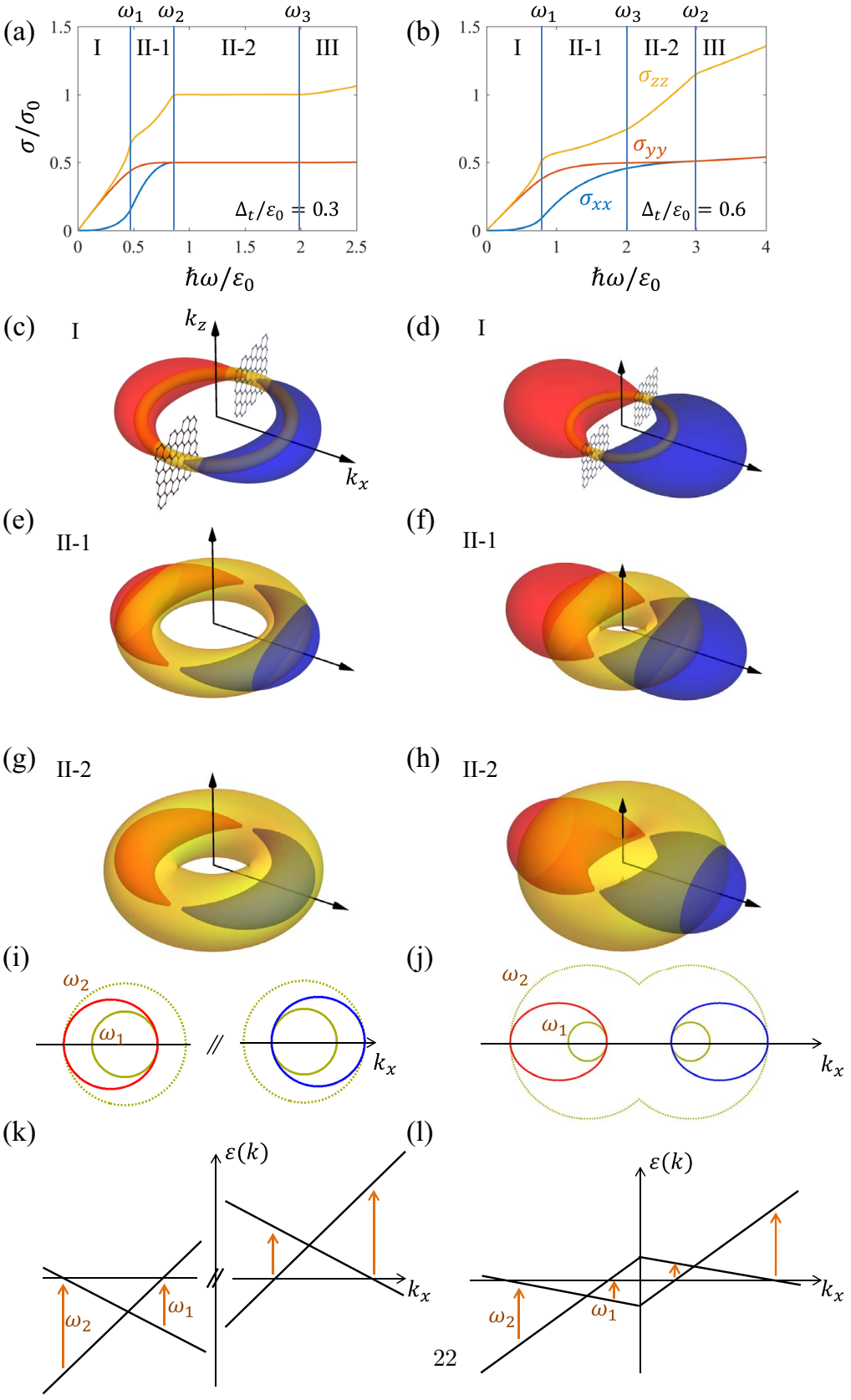
(a)
ω_1 ω_2 ω_3
I
II-1
II-2
III
σ/σ_0
$\Delta_t/\varepsilon_0 = 0.3$
$\hbar\omega/\varepsilon_0$
(b)
ω_1 ω_3 ω_2
σ_{zz}
σ_{yy}
σ_{xx}
$\Delta_t/\varepsilon_0 = 0.6$
(c) I
k_z
k_x
(d) I
(e) II-1
(f) II-1
(g) II-2
(h) II-2
(i)
ω_2
ω_1
k_x
(j)
ω_2
ω_1
k_x
(k)
$\varepsilon(k)$
ω_2
ω_1
k_x
(l)
$\varepsilon(k)$
ω_2
ω_1
k_x

At the intersection between regions I and II-1, the PS allowed by energy conservation (yellow torus) begins to touch the boundary of electron (red) and hole (blue) pockets, and the two isolated PS regions for interband transitions merge forming a connected geometry distinguished from that in region I [see Figs. 3.3(e) and 3.3(f)]. Note that this change of geometry produces a kink in σ_{ii} seen most clearly in σ_{zz} because of its ϕ-independent projection factor [$\mathcal{F}_{zz}(\phi) = 1$; see Eq. (3.5)]. Such a geometrical change also occurs at the intersection between II-1 and II-2 regions giving a kink in σ_{zz}. By observing the cross-sectional view of the PS allowed by energy conservation and the FS in the $k_x - k_z$ plane [see Figs. 3.3(i) and 3.3(j)], we can calculate the frequencies at which kinks appear. Alternatively, since the geometrical changes associated with additional interband transitions occur along the k_x axis, the

---

Figure 3.3 *(preceding page)* (a), (b) Calculated optical conductivities of NLSMs for $\varepsilon_{\rm F} = 0$ with two different tilt energies of (a) $\Delta_{\rm t} = 0.3\varepsilon_0$ and (b) $\Delta_{\rm t} = 0.6\varepsilon_0$. Regions I, II-1, II-2, III represent the frequency domains in which the PS for interband transitions grows continuously without any abrupt changes. (c)-(h) The PS allowed by energy conservation indicated by a yellow torus along with electron (red) and hole (blue) pockets in different frequency domains. Note that in region I the PS allowed for interband transitions consists of two local domains, while in region II they merge together to form a connected geometry. (i), (j) Cross-sectional views of the electron-hole pockets and the PS allowed by energy conservation in the $k_x - k_z$ plane at the frequencies of $\omega = \omega_1$ (yellow solid lines) and $\omega = \omega_2$ (yellow dashed lines), where the PS allowed for interband transitions changes its geometry leading to kink structures in the optical conductivity. (k), (l) Energy band dispersions along the k_x axis with $k_y = k_z = 0$ for (k) $\Delta_{\rm t} = 0.3\varepsilon_0$ and (l) $\Delta_{\rm t} = 0.6\varepsilon_0$. The geometrical changes occur at frequencies corresponding to the onset of interband transitions indicated by arrows.

problem of finding kink frequencies is reduced to obtaining ω_1 and ω_2 in Figs. 3.3(k) and 3.3(l): $\hbar\omega_1 = \frac{2\Delta_t}{\varepsilon_0+\Delta_t}\varepsilon_0$, $\hbar\omega_2 = \frac{2\Delta_t}{\varepsilon_0-\Delta_t}\varepsilon_0$.

In region II-2, for $\Delta_t = 0.3\varepsilon_0$, the PS allowed by energy conservation [yellow torus in Fig. 3.3(g)] covers the whole FS while keeping its toroidal structure similar to the untilted case, thus the optical conductivity shows flat behavior with *exactly the same height as that of untilted NLSMs*. For $\Delta_t = 0.6\varepsilon_0$, however, the PS allowed by energy conservation [yellow spherelike manifold in Fig. 3.3.(h)] is no longer a torus and does not fully cover the whole FS, exhibiting a monotonic increase in σ_{zz} instead of the flat behavior. Note that the PS allowed by energy conservation changes its geometry from a torus to a spherelike manifold at the frequency $\hbar\omega_3 = 2\varepsilon_0$. Thus, the condition for the existence (absence) of the flat region can be obtained from the condition $\omega_2 < \omega_3$ ($\omega_2 > \omega_3$), leading to $\Delta_t < 0.5\varepsilon_0$ ($\Delta_t > 0.5\varepsilon_0$).

In region III, the PS allowed by energy conservation for both $\Delta_t = 0.3\varepsilon_0$ and $\Delta_t = 0.6\varepsilon_0$ merge into a sphere-like geometry covering the whole FS, similar to that of Weyl semimetals. Thus, at high frequencies in this frequency domain, the optical conductivity shows a linear behavior, as already shown in previous studies [38].

3.6 Optical conductivity with $\varepsilon_F \neq 0$

Next, we consider the case where $\varepsilon_F \neq 0$ in the presence of tilt. Figures 3.4(a) and 3.4(b) show calculated optical conductivities of NLSMs for $\varepsilon_F = 0.1\varepsilon_0$ and $\varepsilon_F = 0.5\varepsilon_0$, respectively, with $\Delta_t = 0.3\varepsilon_0$. At low frequencies, the optical conductivity for $\varepsilon_F = 0.1\varepsilon_0$ increases linearly with increasing ω, whereas that for $\varepsilon_F = 0.5\varepsilon_0$ exhibits an optical gap.

To address the difference in the low-frequency behaviors, in Figs. 3.4(c) and 3.4(d) we show the PS allowed by energy conservation corresponding to a low-frequency range along with electron-hole pockets. For $\varepsilon_F = 0.1\varepsilon_0$, there is an available PS for interband transitions consisting of two separate local domains located

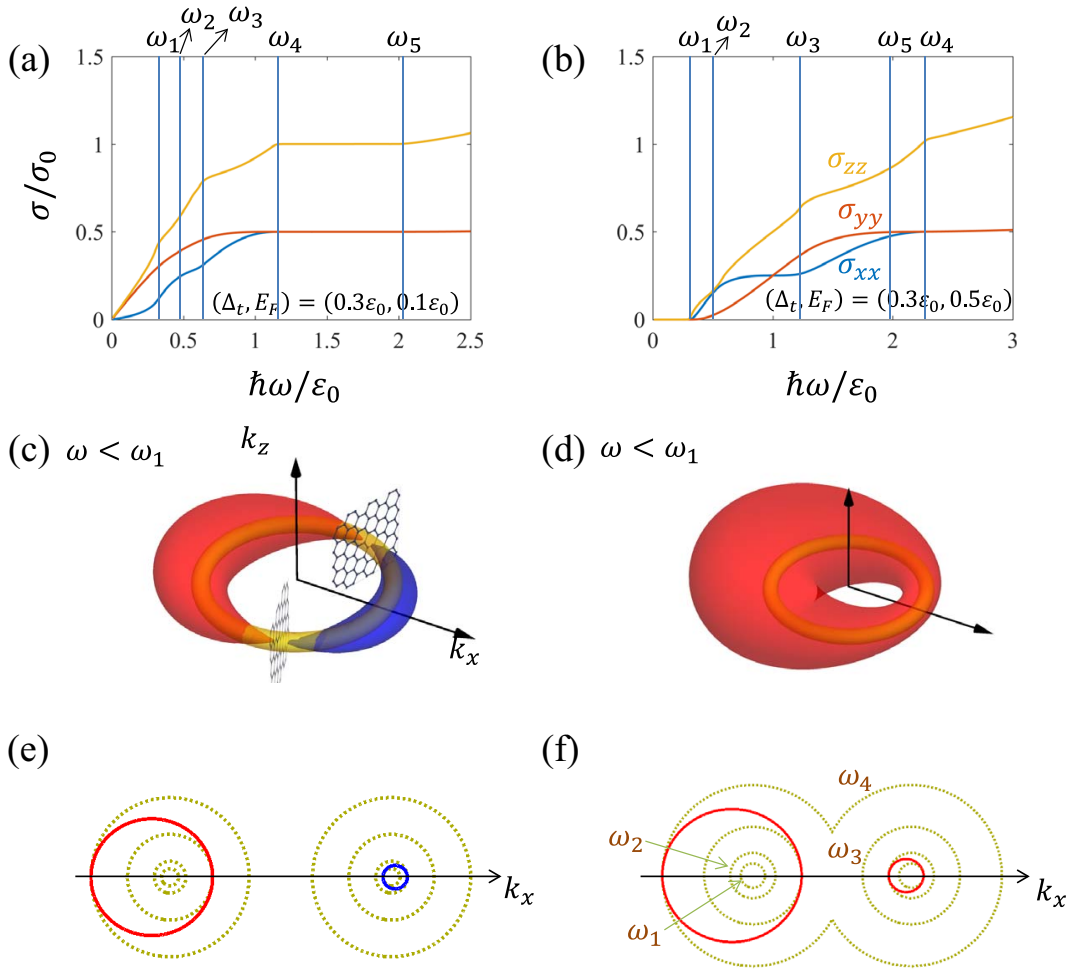

Figure 3.4 (a), (b) Calculated optical conductivities of tilted NLSMs with $\Delta_t = 0.3\varepsilon_0$ for two different Fermi energies of (a) $\varepsilon_F = 0.1\varepsilon_0$ and (b) $\varepsilon_F = 0.5\varepsilon_0$. (c), (d) The PS allowed by energy conservation indicated by a yellow torus along with electron (red) and hole (blue) pockets in the low frequency domain for (c) $\varepsilon_F = 0.1\varepsilon_0$ and (d) $\varepsilon_F = 0.5\varepsilon_0$. (e), (f) Cross-sectional views of the electron-hole pockets and the PS allowed by energy conservation in the $k_x - k_z$ plane at frequencies where kinks appear in the optical conductivity.

around the contact points between the electron and hole pockets. Similarly as we did for $\varepsilon_{\mathrm{F}}=0$, after replacing $|\Delta_{\mathrm{t}}\cos\phi|$ with $|\varepsilon_{\mathrm{F}}-\Delta_{\mathrm{t}}\cos\phi|$ in Eq. (3.26), we obtain the low-frequency optical conductivity as $\frac{\sigma_{ii}}{\sigma_0}\approx C_i\frac{\hbar\omega}{\pi\Delta_{\mathrm{t}}}$ where $i=x,y,z$, $\phi_0=\cos^{-1}\left(\frac{\varepsilon_{\mathrm{F}}}{\Delta_{\mathrm{t}}}\right)$ is the location of graphene sheets sitting around the PS for interband transitions, $C_x=\frac{\left(\frac{\varepsilon_{\mathrm{F}}}{\Delta_{\mathrm{t}}}\right)^2}{\sqrt{1-\left(\frac{\varepsilon_{\mathrm{F}}}{\Delta_{\mathrm{t}}}\right)^2}}$, $C_y=\sqrt{1-\left(\frac{\varepsilon_{\mathrm{F}}}{\Delta_{\mathrm{t}}}\right)^2}$, and $C_z=\frac{1}{\sqrt{1-\left(\frac{\varepsilon_{\mathrm{F}}}{\Delta_{\mathrm{t}}}\right)^2}}$. Note that in the presence of finite ε_{F}, the linear term dominates over the cubic one in the optical conductivity along the tilt direction, in contrast to the $\varepsilon_{\mathrm{F}}=0$ case [see Eq. (3.26)]. (For $\varepsilon_{\mathrm{F}}=\Delta_{\mathrm{t}}$ case, see Sec. III in SM.)

For $\varepsilon_{\mathrm{F}}=0.5\varepsilon_0$, there is no available PS for interband transitions at low frequencies because the electron pocket becomes large enough to cover the entire PS allowed by energy conservation, leading to an optical gap due to Pauli blocking [see Fig. 3.4(d)]. The optical gap persists up to the frequency where the PS allowed by energy conservation touches the boundary of the electron pocket. Similarly as in the $\varepsilon_{\mathrm{F}}=0$ case, we can obtain the size of the optical gap to be $\hbar\omega_{\mathrm{gap}}=2\frac{\varepsilon_{\mathrm{F}}-\Delta_{\mathrm{t}}}{\varepsilon_0+\Delta_{\mathrm{t}}}\varepsilon_0$, and thus the condition for the existence of an optical gap: $\varepsilon_{\mathrm{F}}>\Delta_{\mathrm{t}}$.

As ε_{F} increases, the electron (hole) pocket grows (shrinks), because the number of electrons in the system increases. The imbalanced sizes of the electron and hole pockets lead to two more kinks compared with the $\varepsilon_{\mathrm{F}}=0$ case, as shown in Figs. 3.4(e) and 3.4(f). Similarly as in the $\varepsilon_{\mathrm{F}}=0$ case, we can obtain $\hbar\omega_1=2\left|\frac{\varepsilon_{\mathrm{F}}-\Delta_{\mathrm{t}}}{\varepsilon_0+\Delta_{\mathrm{t}}}\right|\varepsilon_0$, $\hbar\omega_2=2\left|\frac{\varepsilon_{\mathrm{F}}-\Delta_{\mathrm{t}}}{\varepsilon_0-\Delta_{\mathrm{t}}}\right|\varepsilon_0$, $\hbar\omega_3=2\left|\frac{\varepsilon_{\mathrm{F}}+\Delta_{\mathrm{t}}}{\varepsilon_0+\Delta_{\mathrm{t}}}\right|\varepsilon_0$, and $\hbar\omega_4=2\left|\frac{\varepsilon_{\mathrm{F}}+\Delta_{\mathrm{t}}}{\varepsilon_0-\Delta_{\mathrm{t}}}\right|\varepsilon_0$. It follows that the condition for the existence of a flat region can be obtained from $\hbar\omega_4>\hbar\omega_5\equiv 2\varepsilon_0$, leading to $\Delta_{\mathrm{t}}<\frac{1}{2}(\varepsilon_0-\varepsilon_{\mathrm{F}})$. Here ω_5 is the frequency where the PS allowed by energy conservation changes its geometry from a torus to a spherelike manifold.

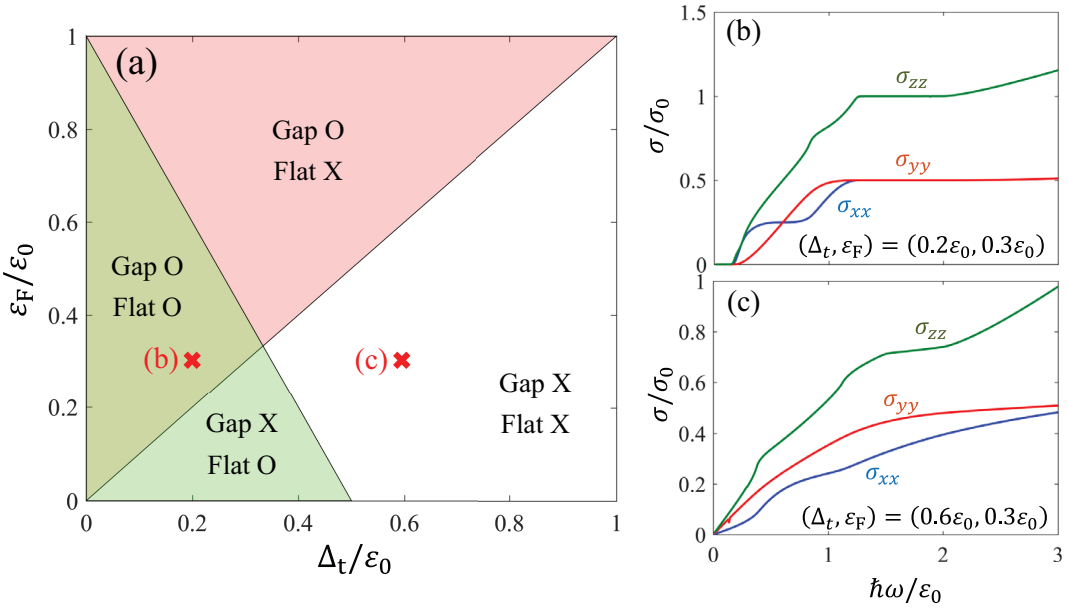

Figure 3.5 (a) Phase diagram for the existence of an optical gap in all components of optical conductivity and a flat region in σ_{zz}. (b), (c) Optical conductivities corresponding to the cross marks indicated in (a). Note that in (b), both the gap and flat region are present, whereas in (c), both are absent.

3.7 Phase diagram for the existence of an optical gap and a flat region

Results in the previous section show that the appearance of an optical gap is not soley determined by the Fermi energy, but also the magnitude of tilt. In addition, the typical flat behavior observed in untilted nodal line systems could not appear in a certain range of parameters of Δ_t and ε_F. In the following, we present conditions for the existence of an optical gap and a flat region. The condition for the appearance of an optical gap in all components of optical conductivity ($\varepsilon_F > \Delta_t$) and that of a flat region in σ_{zz} at intermediate frequencies [$\Delta_t < \frac{1}{2}(\varepsilon_0 - \varepsilon_F)$] are independent of each other, creating four possible scenarios where an optical gap is present/absent at low

frequencies with/without a flat region. Figure 3.5 (a) shows the corresponding phase diagram on the Δ_t/ε_0 and $\varepsilon_F/\varepsilon_0$ plane. Figures 3.5 (b) and (c) show the remaining cases, where both the gap and flat region are present or absent.

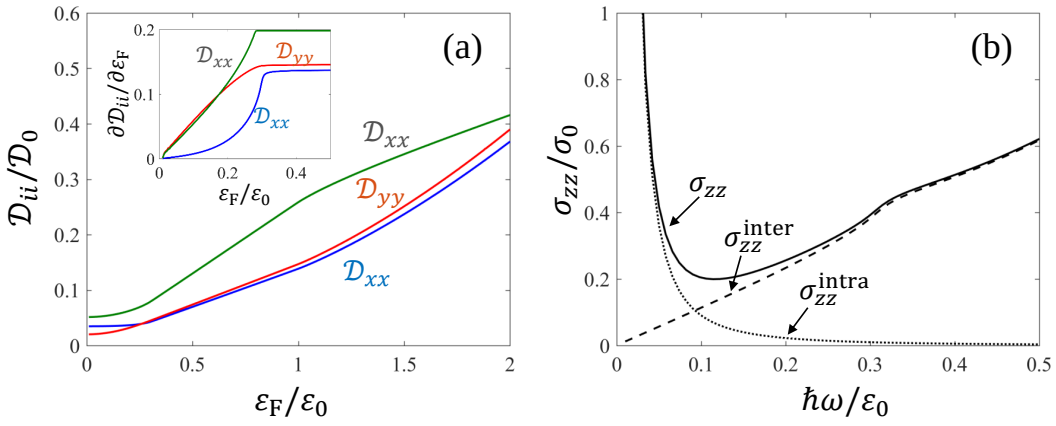

Figure 3.6 (a) The Drude weight of tilted NLSMs with $\Delta_t = 0.3\varepsilon_0$ and (b) the intraband ($\sigma_{zz}^{\text{intra}}$, dotted line) and interband ($\sigma_{zz}^{\text{inter}}$, dashed line) contributions to the optical conductivity σ_{zz} (solid line). The inset to (a) shows the derivative of the Drude weight near $\varepsilon_F = \Delta_t$, where the Drude weight exhibits a nonanalytic kink behavior due to an abrupt change in the geometry of the FS. Here $\mathcal{D}_0 = \frac{e^2}{\hbar} k_0 \varepsilon_0$ and the Drude weight is defined to be $\sigma_{ii}^{\text{intra}} = \mathcal{D}_{ii}\delta(\hbar\omega)$.

3.8 Drude Weight

The intraband contribution to optical conductivity gives rise to a Drude peak at low frequencies whose weight also inherits a nonanalytic density dependence from the geometry of the FS. Interestingly, these are seen most clearly in the *derivatives* of the weight with respect to Fermi energy, as shown in Fig. 3.6.

3.9 Discussion

3.9.1 Nodal lines with SOC

Introducing spin-orbit coupling (SOC) can gap out a nodal line and produce pairs of Weyl points [40]. In such cases, at frequencies below the SOC scale, the PS for interband transitions are spheres enclosing the Weyl nodes, and the conductivity will revert to linear frequency scaling known for Weyl semimetals (WSMs). Above the SOC energy, however, the separated PS recovers a toroidal shape, and this will have the characteristic dependence found in our work. Recent calculations for WSMs in the TaAs class indicate that these materials are weakly broken line node systems where the tilt scale dominates the SOC scale. Thus, our analysis is applicable over a wide frequency range and can be used as a signature of these new states of matter in optical experiments.

3.10 Conclusion

We studied the frequency-dependent conductivity of NLSMs focusing on the effects of carrier density and energy dispersion on the nodal line. We find that the low-frequency conductivity has a rich spectral structure which can be understood using scaling rules derived from the geometry of their Dupin cyclide Fermi surfaces. We identify different frequency regimes, find scaling rules for the optical conductivity in each and demonstrate them with numerical calculations of the inter- and intraband contributions to the optical conductivity using a low-energy model for a generic NLSM.

Chapter 4

Optical Conductivity of multi-Weyl semimetals

4.1 Introduction

In this chapter, we report calculations of the optical conductivity in multi-Weyl semimetals (m-WSMs), and analyze their characteristic frequency dependence in the semimetallic state and in nearby insulating states, focusing on the effects of the winding number, lattice regularization and phase transitions. We find that the results for m-WSMs can be clearly distinguished from those for WSM's by their low-energy frequency dependence, which is determined by the winding number of the m-WSM phase.

4.2 Model

Let us consider a lattice model that shows at some parameter range the m-WSM phase described by Eq. (2.9). A simple lattice model for the Weyl semimetals with $J = 1$ which has inversion symmetry with broken time-reversal symmetry is given

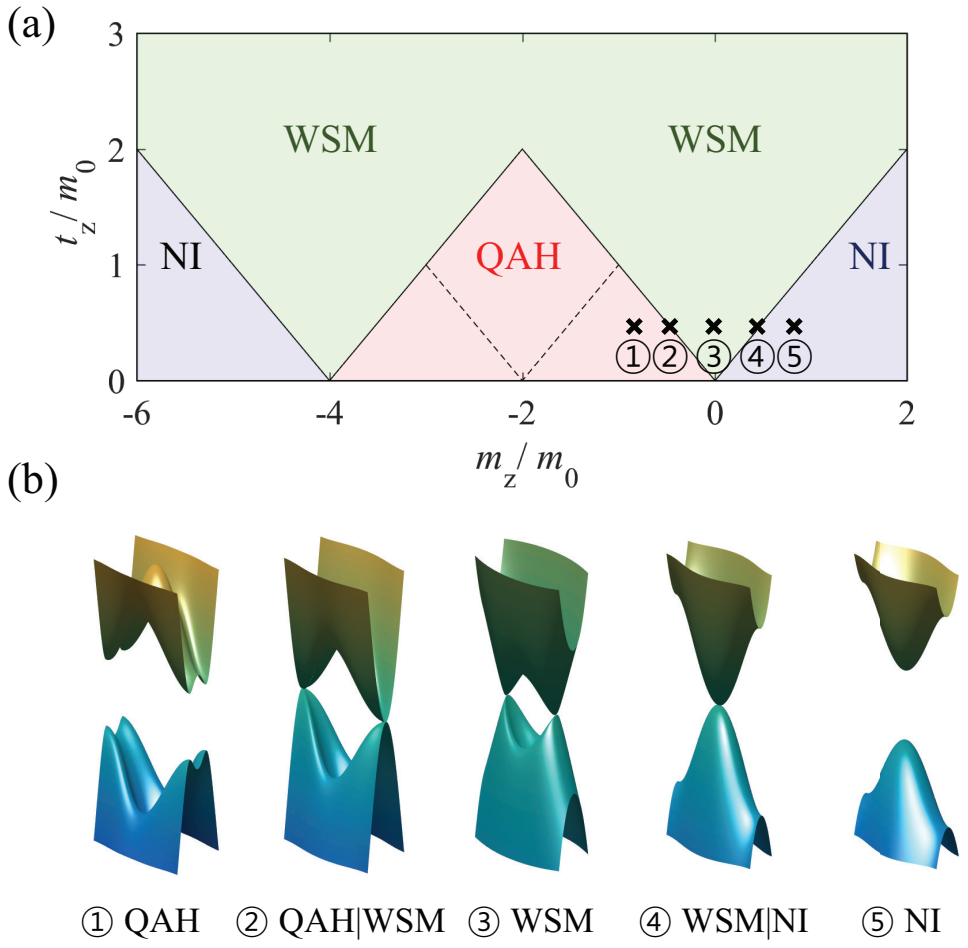

Figure 4.1 (a) Phase diagrams of $J = 2$ lattice models on the t_z/m_0 and m_z/m_0 plane and (b) evolution of the energy band structure from the 3D quantum anomalous Hall (QAH) phase to the normal insulator (NI) phase. Here, we use several values of m_z/m_0 corresponding to different phases, indicated by circled numbers in the phase diagram. QAH|WSM and WSM|NI denote the transition phase between 3D QAH and WSM, and WSM and NI, respectively. The phase diagram for $J = 1$ has a similar shape, but has a different phase boundary between the WSM and 3D QAH represented by the dashed line [16].

by [16, 43, 44]

$$\begin{aligned} H_1 &= t_x \sin(k_x a)\sigma_x + t_y \sin(k_y a)\sigma_y + M_z \sigma_z, \\ M_z &= m_z - t_z \cos(k_z a) + m_0[2 - \cos(k_x a) - \cos(k_y a)], \end{aligned} \tag{4.1}$$

where a is the lattice spacing, and $t_{x,y,z}$, m_z and m_0 are material dependent parameters. Similarly, we can generalize the above lattice model in Eq. (4.1) to $J = 2$ so that near the Weyl points the low-energy Hamiltonian reduces to the form of Eq. (2.9) [30]:

$$\begin{aligned} H_2 &= t_x[\cos(k_y a) - \cos(k_x a)]\sigma_x \\ &\quad + t_y \sin(k_x a)\sin(k_y a)\sigma_y + M_z \sigma_z. \end{aligned} \tag{4.2}$$

Depending on the model parameters, the Hamiltonian in Eqs. (4.1) and (4.2) shows various phases such as normal insulators (NIs), Weyl semimetals, and three-dimensional (3D) quantum anomalous Hall (QAH) states, as shown in Fig. 4.1 along with the corresponding energy band structures. The phase diagram for $J = 2$ has a similar shape to that for $J = 1$ [16], but because of the change in the electronic structure, the optical properties in the m-WSMs show a strong dependence on their chirality.

For the continuum model corresponding to each phase, we choose the parameter range where Weyl nodes arise at $(k_x, k_y) = (0, 0)$. Other choices of parameter ranges give fundamentally identical settings. Using the $\boldsymbol{k} \cdot \boldsymbol{p}$ method, we can write a generic continuum model for various phases as

$$H = \varepsilon_0 \left(\tilde{k}_-^J \sigma_+ + \tilde{k}_+^J \sigma_- \right) + M_z \sigma_z, \tag{4.3}$$

where the mass term is given by $M_z \approx \hbar v_z q_z + \alpha + \beta q_z^2 + \gamma(k_x^2 + k_y^2)$. Here we set $\gamma = \frac{m_0 a^2}{2} > 0$ except for the WSM phase with $\gamma = 0$ where the linear term in M_z dominates over the quadratic term associated with γ at low energies. Note that for

the NI (3D QAH) phase, $\alpha = m_z \mp t_z$ and $\beta = \pm\frac{t_z a^2}{2}$. Then, for each phase, we find

$$\begin{array}{lcccc} \text{NI} & : & q_z = k_z; & v_z = 0; & \alpha, \beta > 0, \\ \text{NI|WSM} & : & q_z = k_z; & v_z = 0; & \alpha = 0, \beta > 0, \\ \text{WSM} & : & q_z = k_z \mp b; & v_z \neq 0; & \alpha = \beta = 0, \\ \text{WSM|QAH} & : & q_z = k_z \mp \frac{\pi}{a}; & v_z = 0; & \alpha = 0, \beta < 0, \\ \text{QAH} & : & q_z = k_z \mp \frac{\pi}{a}; & v_z = 0; & \alpha, \beta < 0, \end{array} \tag{4.4}$$

where $\cos(ba) \equiv m_z/t_z$ with $|m_z|/t_z < 1$. For calculation, we set $k_0 = 1/a$, $t_x = t_y = 4m_0$ and $t_z = 0.5m_0$ with $m_0 > 0$, and vary $-m_0 < m_z < m_0$ with other parameters fixed to induce various phases.

4.3 Continuum model for each phase in multi-Weyl semimetals

In this section, we discuss a continuum model for each phase in the phase diagram, including the transition point. For the calculation, we set $k_0 = 1/a$, $t_x = t_y = 4m_0$ and $t_z = 0.5m_0$ with $m_0 > 0$, and vary $-m_0 < m_z < m_0$ with other parameters fixed to induce various phases.

4.3.1 WSM phase

First, consider a continuum model for the WSM phase. For $|m_z|/t_z < 1$ with $\cos(ba) \equiv m_z/t_z$, two Weyl points appear at $\boldsymbol{k} = \pm b\hat{\boldsymbol{z}}$, at which the conduction and valence bands touch at zero energy. Then, the Hamiltonian for $J = 1$ reduces to the form for Weyl semimetals:

$$H_1 \approx \hbar v_x k_x \sigma_x + \hbar v_y k_y \sigma_y \pm \hbar v_z q_z \sigma_z, \tag{4.5}$$

where $q_z = k_z \mp b$, $\frac{\hbar v_x}{a} = t_x$, $\frac{\hbar v_y}{a} = t_y$ and $\frac{\hbar v_z}{a} = t_z \sin(ba)$. Similarly, for $J = 2$, the Hamiltonian H_2 reduces to Eq. (4.3) with $J = 2$, where $\varepsilon_0 = \frac{1}{2}t_{\parallel}(k_0 a)^2$ with

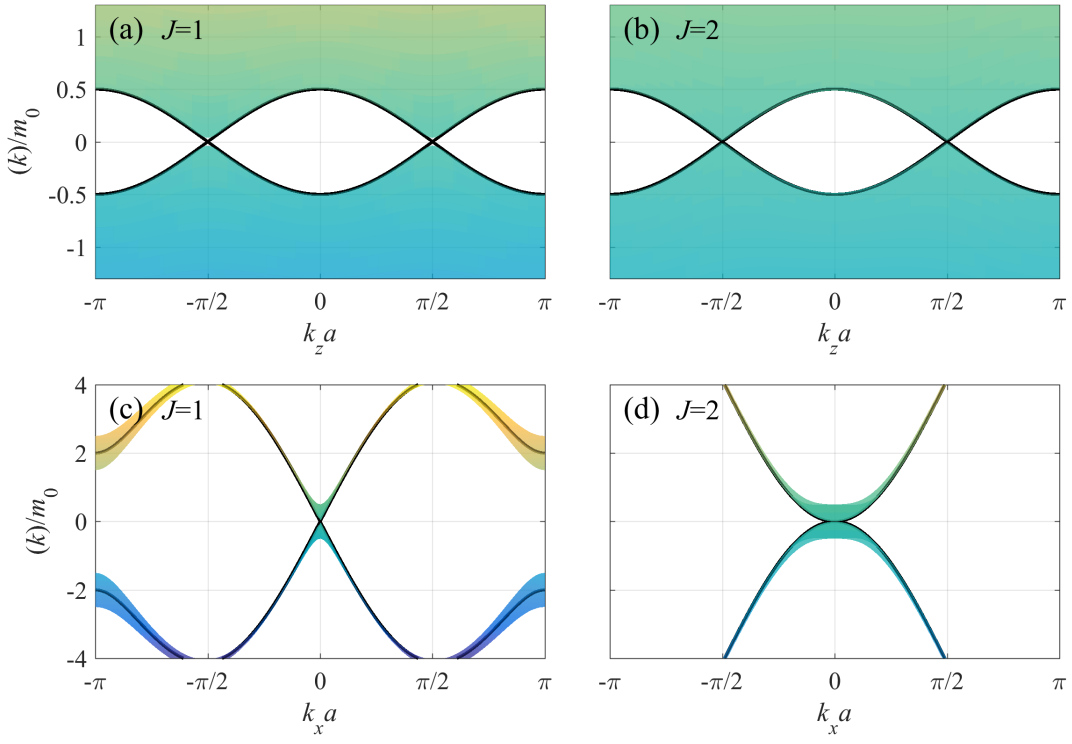

Figure 4.2 Energy dispersions for the $J = 1$ and $J = 2$ lattice models in the WSM phase viewed from the k_z- and k_x-axes. Shaded regions represent the energy dispersions obtained by projecting them to (a), (b) the k_z-axis or to (c), (d) the k_x-axis at $k_y = 0$, in which each point of the dispersion is colored according to the energy scale, with yellow (blue) indicating higher (lower) values. The black solid lines are added to represent the energy dispersions across the Weyl node along (a), (b) the k_z-axis with $k_x = 0$ and (c), (d) the k_x-axis with $k_z = b$. Here, $m_z/m_0 = 0$ and $b = 0.5\pi/a$ are used for calculation.

$t_x = t_y \equiv t_\parallel$ and $\frac{\hbar v_z}{a} = t_z \sin(ba)$. Note that the two Weyl points located at $\boldsymbol{k} = \pm b\hat{\boldsymbol{z}}$ have opposite handedness $\chi = \pm 1$, representing the right-handed/left-handed chirality with Chern number χJ.

Figure 4.2 shows the energy dispersion for the $J = 1$ and $J = 2$ lattice models

in the WSM phase. As shown in Eq. (2.9), the energy dispersion near the Weyl point along the k_z direction with $k_x = k_y = 0$ is linear, while that along the k_x-k_y directions with $k_z = 0$ is proportional to k^J. Note that there always appear multiple Weyl points in the Brillouin zone with the total chirality summing to zero, and in the lattice model we are considering, there are two Weyl nodes with opposite chiralities. Between the two Weyl points, the energy dispersion becomes flat along the k_z direction at $k_x = k_y = 0$, showing a van Hove singularity.

4.3.2 NI phase

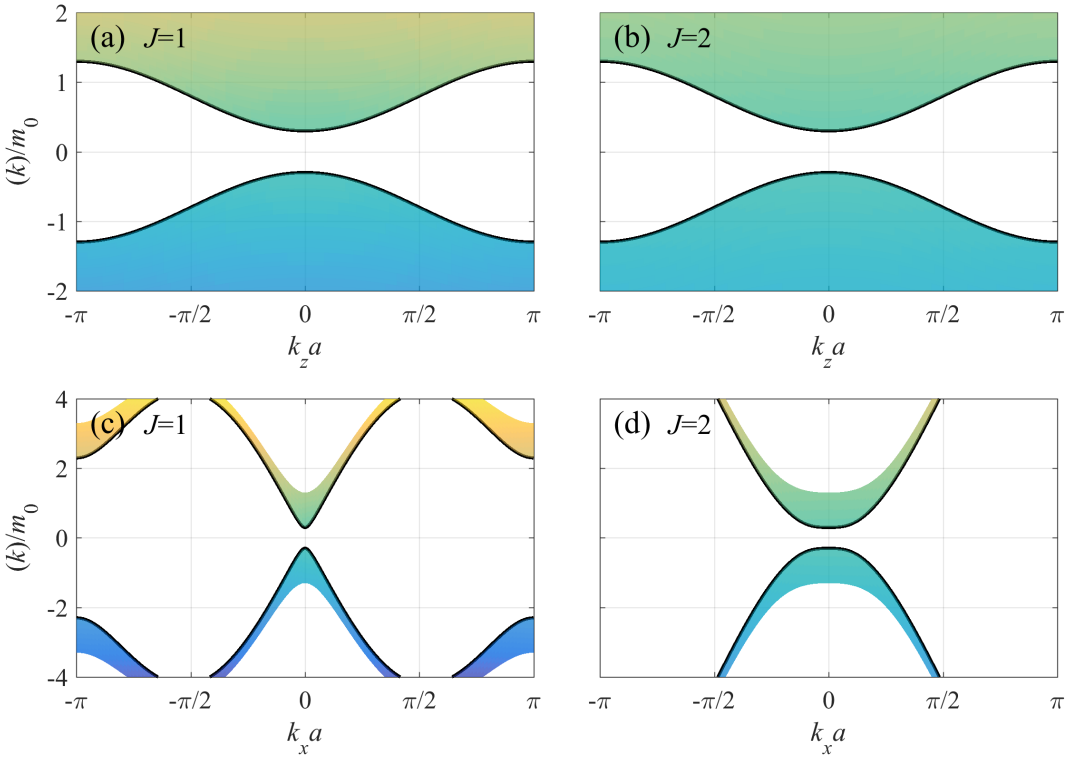

Figure 4.3 Energy dispersions for the (a), (c) $J = 1$ and (b), (d) $J = 2$ lattice models in the NI phase viewed from the (a), (b) k_z- and (c), (d) k_x-axes with $k_y = 0$. Here, $m_z/m_0 = 0.8$ is used for the calculation.

For $m_z > t_z$, the mass term M_z defined in Eq. (4.1) remains positive throughout the Brillouin zone, thus the system is in the trivial insulator phase. Near $\boldsymbol{k} = (0, 0, 0)$, M_z can be approximated as

$$M_z \approx m_z - t_z + \frac{t_z a^2}{2} k_z^2 + \frac{m_0 a^2}{2}(k_x^2 + k_y^2). \tag{4.6}$$

Figure 4.3 shows the energy dispersions for the $J = 1$ and $J = 2$ lattice models with an energy gap of the size of 2α, where $\alpha = m_z - t_z$, which gives rise to a corresponding optical gap.

4.3.3 3D QAH phase

For $m_z < -t_z$, the mass term M_z changes its sign in the Brillouin zone, generating a non-trivial insulating phase in contrast to the case of the NI phase. Near $\boldsymbol{k} = (0, 0, \pm\frac{\pi}{a})$, M_z can be approximated as

$$M_z \approx m_z + t_z - \frac{t_z a^2}{2} q_z^2 + \frac{m_0 a^2}{2}(k_x^2 + k_y^2), \tag{4.7}$$

where $q_z = k_z \mp \frac{\pi}{a}$.

Figure 4.4 shows the energy dispersion for the $J = 1$ and $J = 2$ lattice models in the 3D QAH phase. Because of the negative sign of the constant term $\alpha = m_z + t_z < 0$ in M_z, the 3D QAH phase has a different gap structure compared with the NI phase. Let $\gamma = \frac{m_0 a^2}{2} > 0$. It is easy to show that for $J = 1$, if $\alpha \geq \alpha_c = -\frac{\varepsilon_0^2}{2\gamma k_0^2}$, an energy gap of $2|\alpha|$ appears at $\boldsymbol{k} = (0, 0, \pm\frac{\pi}{a})$, whereas if $\alpha < \alpha_c$, a Mexican hat structure with the gap of $2\sqrt{2\alpha_c\alpha - \alpha_c^2}$ appears away from the $\boldsymbol{k}$ point. Note that in addition to $(k_x, k_y, k_z) = (0, 0, \pm\frac{\pi}{a})$, there appear local minima at $(k_x, k_y, k_z) = (\pm\frac{\pi}{a}, 0, 0)$ and $(0, \pm\frac{\pi}{a}, 0)$ in the $J = 1$ 3D QAH phase. For $J = 2$, there is always a Mexican hat structure for $\alpha < 0$ with a gap of $\frac{2|\alpha|}{\varepsilon_0(\varepsilon_0+\Gamma)}\sqrt{\varepsilon_0^2\Gamma^2 + (\varepsilon_0^2 + \varepsilon_0\Gamma - \Gamma^2)^2}$, where $\Gamma = \gamma k_0^2$.

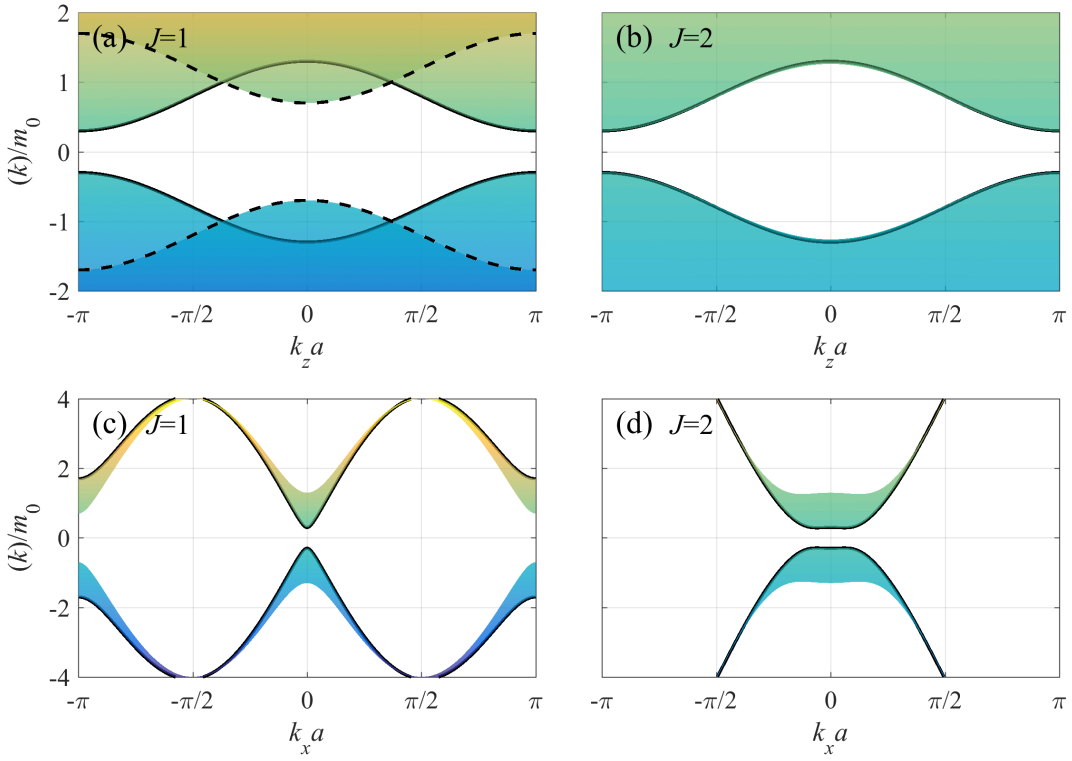

Figure 4.4 Energy dispersions for the (a), (c) $J = 1$ and (b), (d) $J = 2$ lattice models in the 3D QAH phase viewed from the (a), (b) k_z- and (c), (d) k_x-axes with $k_y = 0$. Here, $m_z/m_0 = -0.8$ is used for the calculation. The dashed lines in (a) represent the energy dispersion along the k_z-axis with $k_x = \frac{\pi}{a}$ and $k_y = 0$.

4.3.4 Transition between the WSM and NI phases

At $m_z = t_z$, near $\boldsymbol{k} = (0, 0, 0)$, M_z can be approximated as

$$M_z \approx \frac{t_z a^2}{2} k_z^2 + \frac{m_0 a^2}{2}(k_x^2 + k_y^2). \tag{4.8}$$

Figure 4.5 shows the energy dispersion for the $J = 1$ and $J = 2$ lattice models at the transition between the WSM and NI phases. Note that the low-energy dispersion along the k_z direction with $k_x = k_y = 0$ is *quadratic*, while that along the k_x-k_y directions with $k_z = 0$ is linear for $J = 1$ and quadratic for $J > 1$.

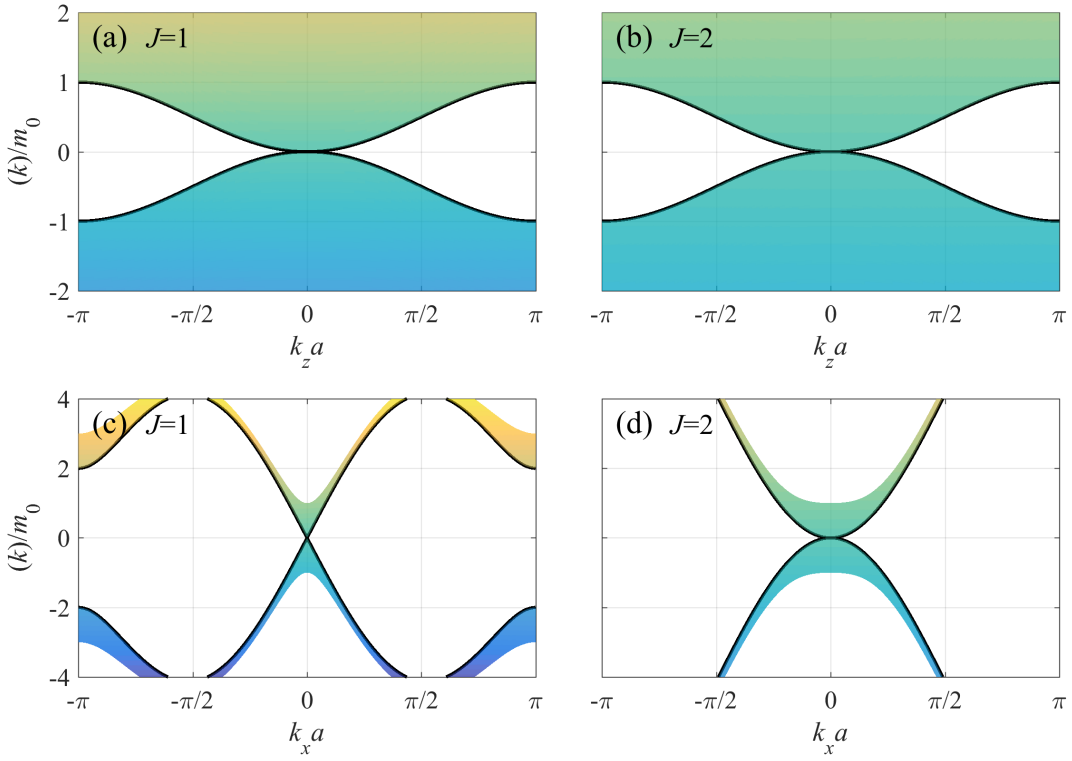

Figure 4.5 Energy dispersions for the (a), (c) $J = 1$ and (b), (d) $J = 2$ lattice models at the transition between the WSM and NI phases viewed from the (a), (b) k_z- and (c), (d) k_x-axes with $k_y = 0$. Here, $m_z/m_0 = 0.5$ is used for the calculation.

4.3.5 Transition between the WSM and 3D QAH phases

At $m_z = -t_z$, near $\boldsymbol{k} = (0, 0, \pm\frac{\pi}{a})$, M_z can be approximated as

$$M_z \approx -\frac{t_z a^2}{2} q_z^2 + \frac{m_0 a^2}{2}(k_x^2 + k_y^2), \tag{4.9}$$

where $q_z = k_z \mp \frac{\pi}{a}$.

Figure 4.6 shows the energy dispersion for the $J = 1$ and $J = 2$ lattice models at the transition between the WSM and 3D QAH phases. Note that similar to the transition between the WSM and NI phases, the low-energy dispersion along the k_z direction with $k_x = k_y = 0$ is *quadratic*, while that along the k_x-k_y directions with

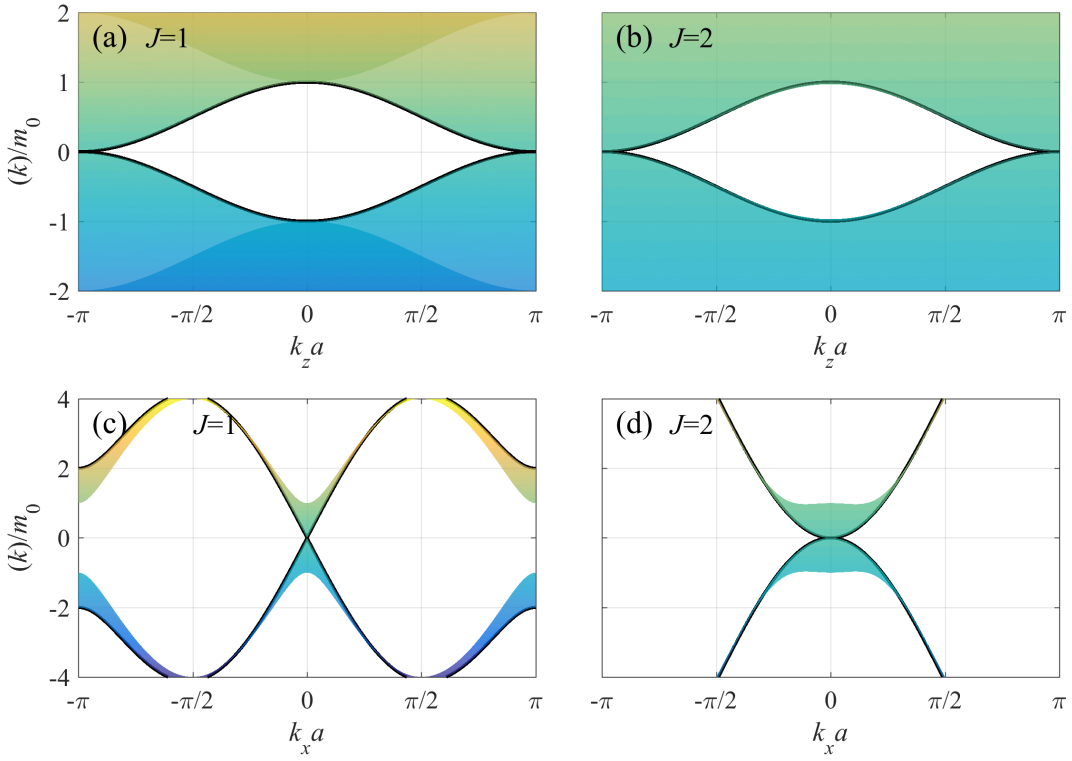

Figure 4.6 Energy dispersions for the (a), (c) $J = 1$ and (b), (d) $J = 2$ lattice models at the transition between the WSM and 3D QAH phases viewed from the (a), (b) k_z- and (c), (d) k_x-axes with $k_y = 0$. Here, $m_z/m_0 = -0.5$ is used for the calculation.

$q_z = 0$ is linear for $J = 1$ and quadratic for $J > 1$.

4.4 Optical conductdivity in WSM phase

In the following, we consider only the undoped case with $\mu = 0$. In the clean limit at zero temperature, the real part of the longitudinal optical conductivity for m-WSMs

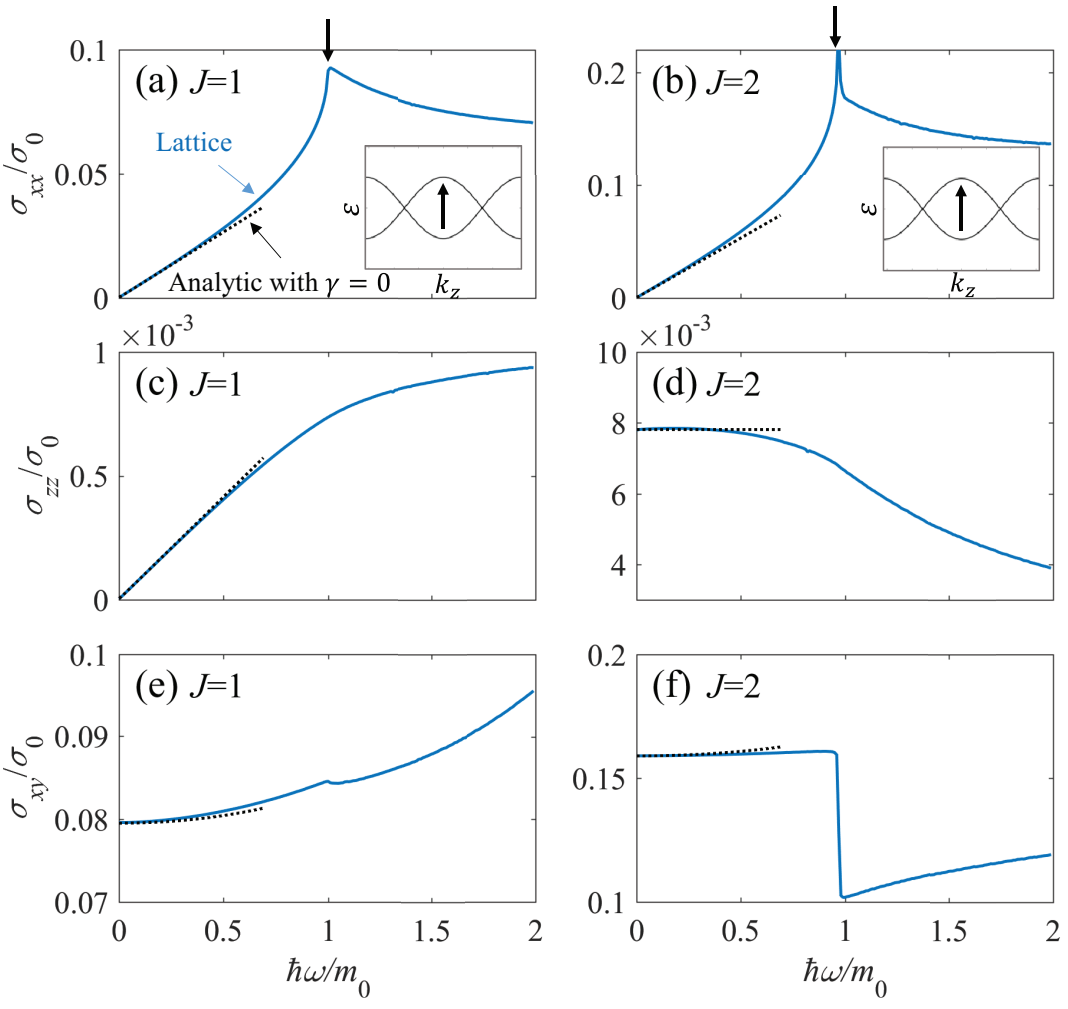

Figure 4.7 Real part of (a)-(d) longitudinal and (e), (f) transverse optical conductivities in units of $\sigma_0 = \frac{e^2}{\hbar a}$ for the lattice (blue solid line) and continuum (black dotted line) models in the WSM phase. The arrows in the insets indicate interband transitions corresponding to kink structures in $\sigma_{xx}(\omega)$ and $\sigma_{xy}(\omega)$. Here, $m_z/m_0 = 0$, $b = 0.5\pi/a$, and $k_c = \pi/a$ are used for calculation.

within the continuum model is given by

$$\sigma_{xx}(\omega) = \frac{g_{\mathrm{N}}}{24\pi}\frac{Je^2}{\hbar v_z}\omega, \tag{4.10a}$$

$$\sigma_{zz}(\omega) = \frac{g_{\mathrm{N}}}{24\pi}\frac{e^2 v_z}{\hbar v_\parallel^2} A_{zz}^{\mathrm{WSM}} \left(\frac{\omega}{\omega_0}\right)^{\frac{2}{J}-1} \omega_0, \tag{4.10b}$$

where $g_{\mathrm{N}} = 2$ is the number of nodes, $\varepsilon_0 = \hbar\omega_0 = \hbar v_\parallel k_0$, $A_{zz}^{\mathrm{WSM}} = \frac{3\sqrt{\pi}\Gamma\left(\frac{1}{J}\right)}{2^{\frac{2}{J}} J^2 \Gamma\left(\frac{1}{J}+\frac{3}{2}\right)}$, and $\Gamma(x)$ is the gamma function [45]. Note that $\sigma_{xx}(\omega) \propto J\omega$ while $\sigma_{zz} \propto \omega^{\frac{2}{J}-1}$, exhibiting the chirality dependent power-law exponents in frequencies. Also note that the effect of a finite μ simply produces a small gap due to Pauli blocking in interband transitions and a conventional Drude peak from intraband transitions, which does not alter the characteristic frequency dependence of the conductivity as long as μ is not high enough that the effective Hamiltonian is still characterized by a m-WSM Hamiltonian (see Appendix B.2).

Next, consider the real part of the Hall or transverse optical conductivity. Note that a sign change of M_z in the Brillouin zone can produce a nontrivial state that supports a Hall effect in the k_x-k_y plane for a fixed k_z. We therefore focus only on the in-plane off-diagonal part $\sigma_{xy}(\omega)$. If two Weyl nodes with opposite chirality are located at $\pm\boldsymbol{b} = \pm b\hat{\boldsymbol{z}}$, the real part of the Hall conductivity up to second order in ω is given by

$$\sigma_{xy}(\omega) = J\chi\frac{e^2}{\hbar}\left(\frac{b}{2\pi^2} + \frac{1}{24\pi^2 v_z^2}\frac{b}{k_{\mathrm{c}}^2 - b^2}\omega^2\right), \tag{4.11}$$

where k_{c} is the cutoff along the k_z direction. Here, χ represents the right-handed/left-handed chirality, which has $\chi = \pm 1$ if the node with positive chirality is at $\pm b\hat{\boldsymbol{z}}$ and the other at $\mp b\hat{\boldsymbol{z}}$. Note that the Hall conductivity for m-WSMs is given by J times that for $J = 1$ Weyl semimetals, thus their surface states could be manifested by J Fermi arcs connecting the two Weyl nodes.

Figure 4.7 shows the calculated optical conductivities for $J = 1$ and $J = 2$ lattice and continuum models, respectively. At low frequencies, the lattice models

are approximated by the corresponding low energy model in Eq. (2.9), thus the optical conductivities obtained from the lattice and continuum models are in good agreement. As the frequency increases, however, optical conductivities deviate from the continuum model and show a kink structure in $\sigma_{xx}(\omega)$ and $\sigma_{xy}(\omega)$ at $\hbar\omega = 2|m_z - t_z|$ due to the interband transitions between states around the van Hove singularity [46], as shown in the insets to (a) and (b).

4.5 Optical conductdivity in insulator phases

For the NI phase ($\alpha > 0$) and 3D QAH phase ($\alpha < 0$), we obtain the leading-order ω dependence of longitudinal optical conductivities analytically assuming $\gamma = 0$ in the vicinity of $\hbar\omega = 2|\alpha|$,

$$\sigma_{xx}(\omega) \sim (\hbar\omega - 2|\alpha|)^{\frac{1}{2}}\,\Theta(\hbar\omega - 2|\alpha|), \tag{4.12a}$$

$$\sigma_{zz}(\omega) \sim (\hbar\omega - 2|\alpha|)^{\frac{1}{J}+\frac{3}{2}}\,\Theta(\hbar\omega - 2|\alpha|). \tag{4.12b}$$

Note that similarly to the WSM phase, $\sigma_{xx}(\omega)$ has the same ω dependence regardless of the chirality index J, while $\sigma_{zz}(\omega)$ has different power-law exponents depending on J. Here the analytic results are obtained assuming $\gamma = 0$ for simplicity, which is valid when the effect of the band distortion associated with nonzero γ is small ($\gamma k_0^2 \ll \varepsilon_0$ or $m_0 \ll t_x, t_y$). As $\gamma k_0^2/\varepsilon_0$ increases, the power-law exponent deviates from the analytic expression in Eq. (4.12) obtained assuming $\gamma = 0$, and the derivation is more significant for $J = 2$ than $J = 1$ because the kinetic term associated with J is comparable to the quadratic γ term at low frequencies (see Appendix B.2).

The transverse optical conductivities in the NI and 3D QAH phases up to second order in ω are given by

$$\sigma_{xy}(\omega) = \xi\sigma_{xy}^{\mathrm{QAH}} + \frac{e^2}{\hbar}B_{xy}\omega^2, \tag{4.13}$$

where $\sigma_{xy}^{\mathrm{QAH}} = \frac{Je^2}{\hbar}\frac{k_c}{2\pi^2}$ and $\xi = 0$ ($\xi = 1$) for the NI (3D QAH) phase. The static part ($\omega = 0$) in Eq. (4.13) can be obtained after properly subtracting the residual

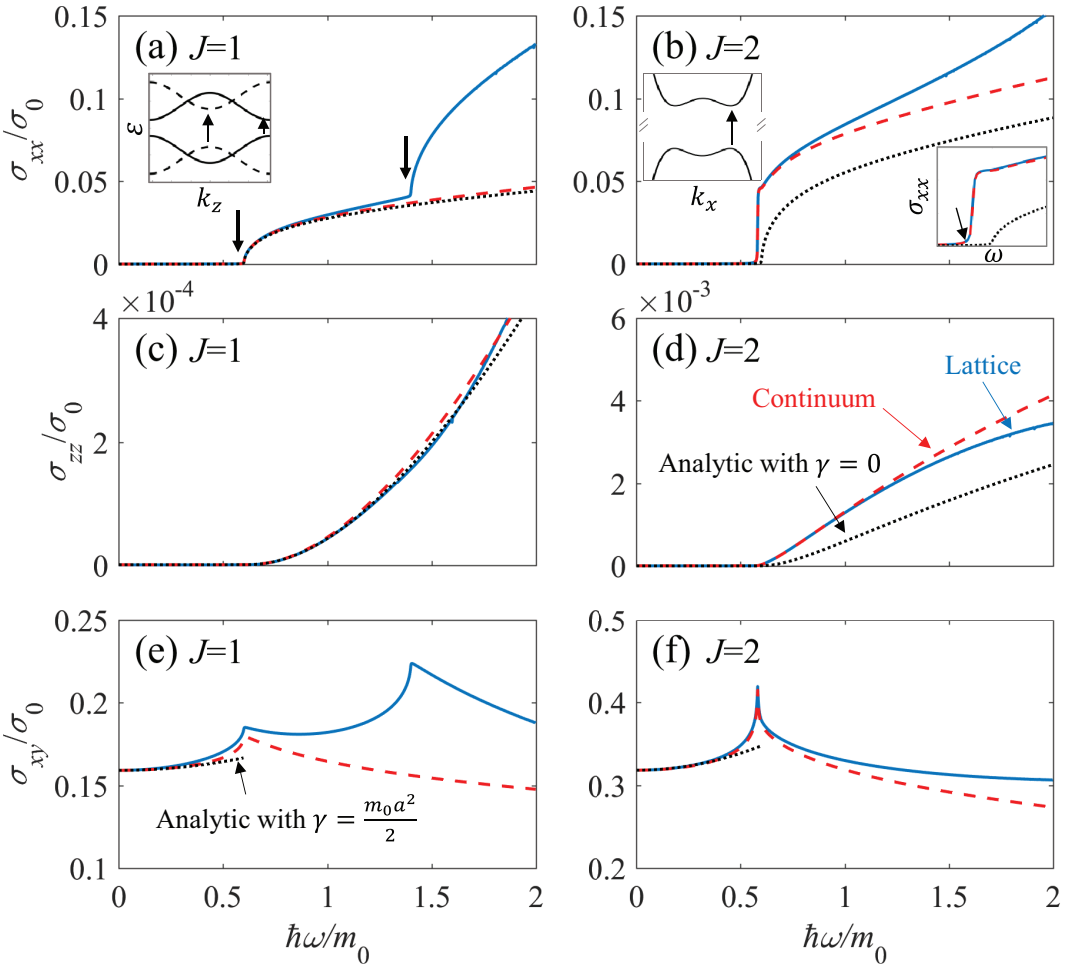

Figure 4.8 Real part of (a)-(d) longitudinal and (e), (f) transverse optical conductivities in the 3D QAH phase for the lattice model (blue solid line), the continuum model (red dashed line), and the analytic results (black dotted line). For the longitudinal (transverse) conductivities, the analytic results are obtained for $\gamma = 0$ ($\gamma = \frac{m_0 a^2}{2}$). Solid (dashed) lines in the inset to (a) represent the energy dispersion for $J = 1$ along the k_z direction with $k_x = 0$ ($k_x = \frac{\pi}{a}$) and $k_y = 0$. The left inset to (b) represents the energy dispersion for $J = 2$ along the k_x direction with $k_z = \frac{\pi}{a}$ and $k_y = 0$, and the right inset to (b) shows an enlarged view in $\sigma_{xx}(\omega)$ near the interband transition. Arrows in the insets indicate interband transitions corresponding to the kink structures appearing in σ_{xx} and σ_{xy}. Here, $m_z/m_0 = -0.8$ and $k_c = \pi/a$ are used for the calculation.

term, because the static Hall conductivity for the continuum model is not properly regularized carrying an arbitrary residual value. Thus only the difference in this quantity between different electronic states is experimentally measurable, giving a quantized value in the 3D QAH phase while zero in the NI phase. In this sense, we choose the momentum cutoff along the k_z direction as $k_c = \pi/a$ so that the properly subtracted static Hall conductivity in the 3D QAH phase has the same quantized value as in the lattice model. A detailed discussion on the regularization process and the expression for B_{xy} can be found in the Appendix B.1. Note that for the transverse optical conductivities, we present analytic results with non-zero γ.

Figure 4.8 shows calculated optical conductivities for the $J = 1$ and $J = 2$ lattice and continuum models in the 3D QAH phase. If $\gamma = 0$, the energy gap with a size of $2|\alpha|$ for both NI and 3D QAH phases leads to zero conductivity for frequencies $\hbar\omega < 2|\alpha|$ due to the optical gap. Because of the non-zero γ, a Mexican hat structure appears in the 3D QAH phase (but not in the NI phase) if $\alpha < \alpha_c = -\frac{\varepsilon_0^2}{2\gamma k_0^2}$ for $J = 1$, and if $\alpha < 0$ for $J = 2$ exhibiting a shifted interband peak with respect to the $\gamma = 0$ result. For the $J = 1$ lattice model in the 3D QAH phase, an additional kink structure appears at $\hbar\omega = 2|m_z - t_z + 2m_0|$ due to the interband transitions at local minima $(k_x, k_y, k_z) = (\pm\frac{\pi}{a}, 0, 0)$, $(0, \pm\frac{\pi}{a}, 0)$, as shown in Fig. 4.8(a).

At the transition point between the WSM and NI phases or between the WSM and 3D QAH phases, the longitudinal (transverse) optical conductivities obtained assuming a zero (non-zero) γ are given by

$$\sigma_{xx}(\omega) = \frac{e^2}{\hbar} A_{xx} (\hbar\omega)^{\frac{1}{2}}, \tag{4.14a}$$

$$\sigma_{zz}(\omega) = \frac{e^2}{\hbar} A_{zz} (\hbar\omega)^{\frac{2}{J} - \frac{1}{2}}, \tag{4.14b}$$

$$\sigma_{xy}(\omega) = \xi \sigma_{xy}^{\mathrm{QAH}} + \frac{e^2}{\hbar} C_{xy} \omega^{\nu}. \tag{4.14c}$$

Note that similarly as in the NI and 3D QAH phases, the static part of $\sigma_{xy}(\omega)$ should be properly subtracted by the residual term. Here, the exponent $\nu \approx 0.5$ is

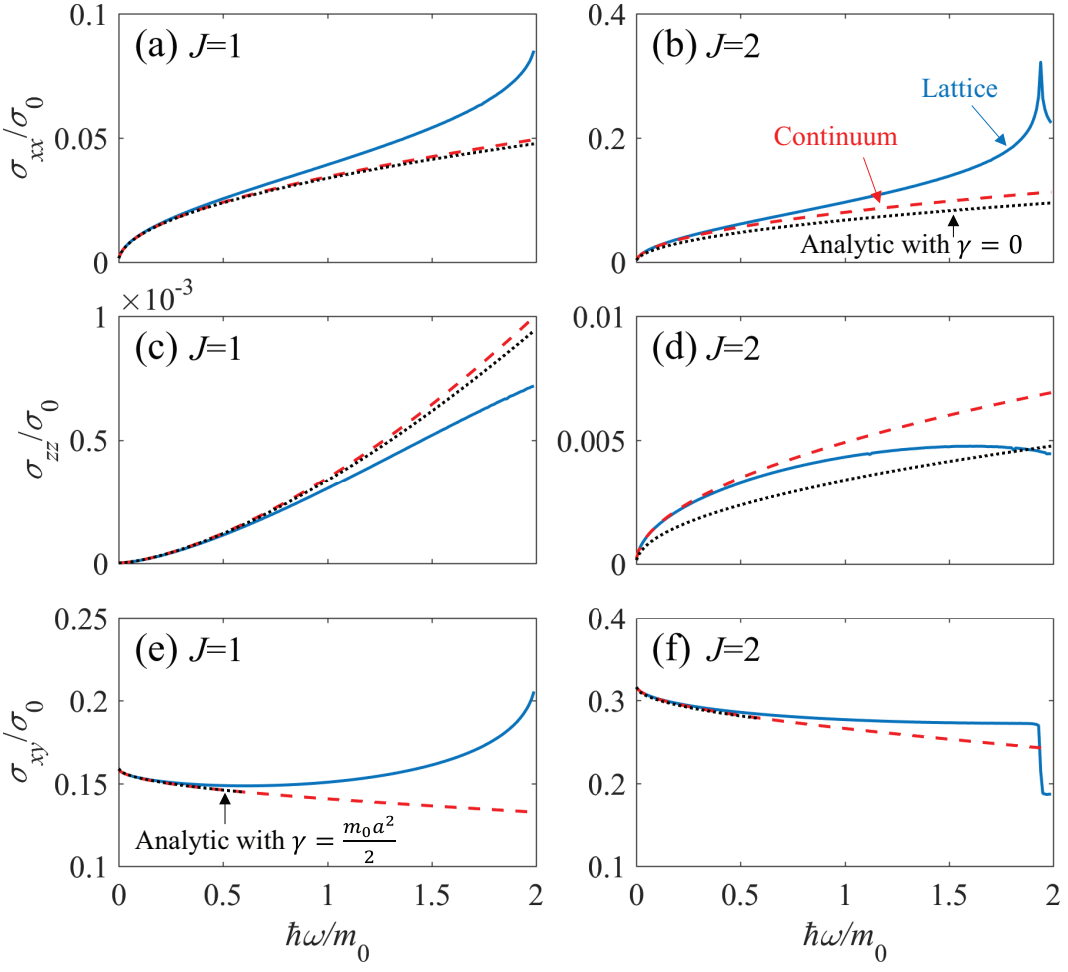

Figure 4.9 Real part of (a)-(d) longitudinal and (e), (f) transverse optical conductivities at the transition between the 3D QAH and WSM phases for the lattice model (blue solid line), the continuum model (red dashed line), and the analytic results (black dotted line). For the longitudinal (transverse) conductivities, the analytic results are obtained for $\gamma = 0$ ($\gamma = \frac{m_0 a^2}{2}$). Here, $m_z/m_0 = -0.5$ and $k_c = \pi/a$ are used for calculation.

found numerically for $J = 1, 2$ with a frequency independent coefficient C_{xy}. Note that the longitudinal conductivities for both transition points are identical (within

a $\gamma = 0$ approximation), whereas the Hall conductivities have different static values, with the difference given by $\sigma_{xy}^{\mathrm{QAH}}$.

4.6 Discussion

Recently, Huang *et al.* [4] demonstrated that strontium silicide ($SrSi_2$) hosts double Weyl nodes with a chirality $J = 2$. The effective Hamiltonian, which describes one of the Weyl nodes with a chirality $J = 2$ in $SrSi_2$, resembles that of bilayer graphene with the interlayer hopping replaced by the spin-orbit coupling Δ connecting the two $J = 1$ Weyl Hamiltonians. If we assume $\mu = 0$, at low frequencies the optical conductivity for the double Weyl nodes in $SrSi_2$ behaves similar to that of the $J = 2$ Weyl semimetals, showing $\sigma_{xx} \sim \omega$ and $\sigma_{zz} \sim \omega^0$ dependence, whereas at high frequencies, the optical conductivity shows two copies of the $J = 1$ Weyl semimetals exhibiting a linear ω dependence in σ_{xx} and σ_{zz}. At intermediate frequencies, kink structures appear at frequencies comparable to the energy scales of interband transitions determined by Δ. Note that the double Weyl nodes in $SrSi_2$ are not actually located at $\mu = 0$, thus the longitudinal conductivity in real $SrSi_2$ will give additional features of the Pauli blocking and the Drude peak. In addition, in a real sample, multiple Weyl nodes coexist, thus the optical conductivity can be obtained by the sum of the contribution from each node.

4.7 Conclusion

In conclusion, we studied the optical properties of m-WSMs in semimetallic and nearby insulating phases, focusing on the frequency dependence of optical conductivity. We demonstrated that the optical conductivities $\sigma_{xx}(\omega)$, $\sigma_{zz}(\omega)$ and $\sigma_{xy}(\omega)$ show a characteristic frequency dependence that strongly varies according to the winding number and phase of the system, and thus can be used as a spectroscopic signature of m-WSMs.

Chapter 5

Collective modes in multi-Weyl semimetals

5.1 Introduction

The goal of this chapter is to investigate electronic collective modes of chiral gapless electron-hole systems and find wave-vector-dependent plasmon dispersions, considering interband transitions along with chirality of the systems. We consider both gapless semimetals with an isotropic band dispersion and multi-Weyl semimetals with an anisotropic band dispersion. We calculate the plasmon modes and the energy loss functions (spectral strength) in gapless semimetals, and present analytical and numerical results for long-wavelength plasma frequencies focusing on the effect of chirality. Throughout the chapter we consider the systems with the finite carrier density, i.e., either electron or hole doped (or gated) systems at zero temperatures.

We find many intriguing and unexpected features of the plasmon modes and their Landau damping in gapless semimetals. For chiral systems with the isotropic linear and quadratic band dispersion ($N = 1, 2$ in $E \propto k^N$) the long-wavelength

plasmons lie outside the Landau damping regions due to the depolarization effects arising from the interband transition and therefore they do not decay by producing electron-hole pairs. For the systems with higher-order dispersions ($N \geq 3$), the long-wavelength plasma frequencies divided by Fermi energy (i.e., $\hbar\omega_{\rm p}/E_{\rm F}$) increase as the density decreases and enter the interband single particle excitation (SPE) region at the critical carrier density, where the dispersion shows a discrete energy jump. For the multi-Weyl systems with an anisotropic dispersion (i.e., with a linear band dispersion along z direction and non-linear in x-y directions), one interesting salient feature in the calculated plasma frequency is the density dependence of the plasmon. We find that the density dependence of the long-wavelength plasma frequency along the direction of non-linear dispersion behaves like that of the isotropic linear band model ($N = 1$), while along the direction of linear dispersion it behaves like that of the isotropic non-linear model ($N \geq 2$). We find that both the plasmons remain undamped over a broad range of density and interaction strength due to the chirality induced red-shift of plasmon modes. We believe that our predictions may be easily observable via inelastic light-scattering spectroscopy[47–49] or inelastic electron-scattering spectroscopy [50–54].

5.2 The Isotropic Model

Before we calculate the collective modes in gapless multi-Weyl semimetals with anisotropic energy band dispersions, we first consider the gapless semimetals with the isotropic band dispersions. For the isotropic model we consider the following Hamiltonian that describes a chiral gapless system with the symmetric energy dispersion,

$$H_N^{\rm ch} = E_0 \left(\frac{|\boldsymbol{k}|}{k_0}\right)^N \hat{\boldsymbol{k}} \cdot \boldsymbol{\sigma}, \tag{5.1}$$

where $\boldsymbol{k}$ is the wave vector, $\hat{\boldsymbol{k}} = \boldsymbol{k}/|\boldsymbol{k}|$, $\boldsymbol{\sigma}$ are Pauli matrices acting in the space of two bands involved at the Weyl point, and E_0 and k_0 are material dependent parameters,

which have units of energy and momentum, respectively. The corresponding energy dispersions are given by $E_{\boldsymbol{k},\pm} = \pm E_0(|\boldsymbol{k}|/k_0)^N$ and the eigenfunctions corresponding to the $\pm$ energies are

$$|+\rangle = (\cos\frac{\theta}{2}, e^{i\phi}\sin\frac{\theta}{2}), \tag{5.2}$$

$$|-\rangle = (-\sin\frac{\theta}{2}, e^{i\phi}\cos\frac{\theta}{2}), \tag{5.3}$$

where $\theta = \tan^{-1}\left(\sqrt{k_x^2+k_y^2}/k_z\right)$ and $\phi = \tan^{-1}(k_y/k_x)$. The $|+\rangle$ state with positive energy represents the conduction band, and the $|-\rangle$ state with negative energy represents the valence band. Note that the Hamiltonian in Eq. (5.1) with $N = 1$ corresponds to the Hamiltonian of Weyl semimetals. To understand the effects of chirality on the plasmon properties beyond the energy dispersion of the system, we also consider the following form of a non-chiral gapless Hamiltonian:

$$H_N^{\rm nch} = E_0\left(\frac{|\boldsymbol{k}|}{k_0}\right)^N \sigma_z. \tag{5.4}$$

The non-chiral Hamiltonian we introduce in Eq. (5.4) has exactly the same energy dispersion as the chiral system in Eq. (5.1). Unlike the chiral model, however, its eigenstates are completely independent of each other so that the chiral nature of wave functions is absent. It will be shown later that the interband transitions associated with chirality are largely responsible for differences between plasmons in the presence and absence of chirality.

Plasmons are defined as longitudinal in-phase oscillation of all the carriers driven by the self-consistent electric field generated by the local variation in charge density. To find the full plasmon dispersion at finite wave vectors we need the quantum mechanical many-body theory for the collective motion of all carriers[42]. Within the random phase approximation (RPA), the plasmon dispersion is obtained by finding zeros of the dynamical dielectric function, which is expressed as [42, 55–58, 61]

$$\varepsilon^{\rm RPA}(q,\omega) = 1 - v_{\rm C}(q)\Pi(q,\omega), \tag{5.5}$$

where $v_{\mathrm{C}}(q) = \frac{4\pi e^2}{\kappa q^2}$ is the Coulomb interaction and κ is a background dielectric constant. The non-interacting polarizability $\Pi(q,\omega)$ is given by

$$\Pi(q,\omega) = g\sum_{s,s'}\int \frac{d^3k}{(2\pi)^3}\frac{f_{\boldsymbol{k},s} - f_{\boldsymbol{k}+\boldsymbol{q},s'}}{\hbar\omega + \Delta^{ss'}_{\boldsymbol{k},\boldsymbol{k}+\boldsymbol{q}} + i0^+}F^{ss'}_{\boldsymbol{k},\boldsymbol{k}+\boldsymbol{q}}, \tag{5.6}$$

where $f_{\boldsymbol{k},s} = \left[1+\exp\left(\frac{E_{\boldsymbol{k},s}-\mu}{k_{\mathrm{B}}T}\right)\right]^{-1}$ is the Fermi distribution function for the band $s = \pm 1$, μ is the chemical potential, $\Delta^{ss'}_{\boldsymbol{k},\boldsymbol{k}+\boldsymbol{q}} = E_{\boldsymbol{k},s} - E_{\boldsymbol{k}+\boldsymbol{q},s'}$, $F^{ss'}_{\boldsymbol{k},\boldsymbol{k}+\boldsymbol{q}} = \frac{1}{2}(1 + ss'\cos\theta_{\boldsymbol{k},\boldsymbol{k}+\boldsymbol{q}})$ is the overlap factor, $\theta_{\boldsymbol{k},\boldsymbol{k}+\boldsymbol{q}}$ is the angle between $\boldsymbol{k}$ and $\boldsymbol{k}+\boldsymbol{q}$, and g denotes the number of degenerate Weyl nodes of the system. Since we focus on the long-wavelength plasmons in this work, we neglect transitions between different nodes located at different momenta. Within this assumption, contributions from other Weyl nodes can be taken into account by multiplying the degeneracy factor g. It is important to notice that in the non-chiral model described by Eq. (5.4) and later by Eq. (5.14), the overlap factor becomes the Kronecker δ, i.e., $F^{ss'}_{\boldsymbol{k},\boldsymbol{k}+\boldsymbol{q}} = \delta_{ss'}$, which excludes the possibility of any interband transitions between the conduction and valence bands. In this sense, the non-chiral model considered here is a two-band model without interband transitions, which is effectively a single-band model with the same energy dispersion.

We first consider the loss function of 3D gapless semimetals, which is calculated from the dielectric function (i.e., $-\mathrm{Im}[1/\varepsilon(q,\omega)]$) and can be directly measured in experiments such as inelastic electron spectroscopy. The loss function is related to the dynamical structure factor $S(q,\omega)$ by $S(q,\omega) \propto -\mathrm{Im}[1/\varepsilon(q,\omega)]$, which gives a direct measure of the spectral strength of the various elementary excitations. Figure 6.1 shows the density plots of calculated energy-loss functions in (q,ω) space for $N = 2$ (parabolic dispersion) and $N = 3$ (cubic dispersion) in the absence (top panels) and presence (bottom panels) of chirality. Plasmon dispersions are given by sharp peaks of the energy-loss function, which correspond to the poles of the dielectric function. When both $\mathrm{Re}[\epsilon]$ and $\mathrm{Im}[\epsilon]$ become zero (i.e., $\epsilon(q,\omega) = 0$, which defines

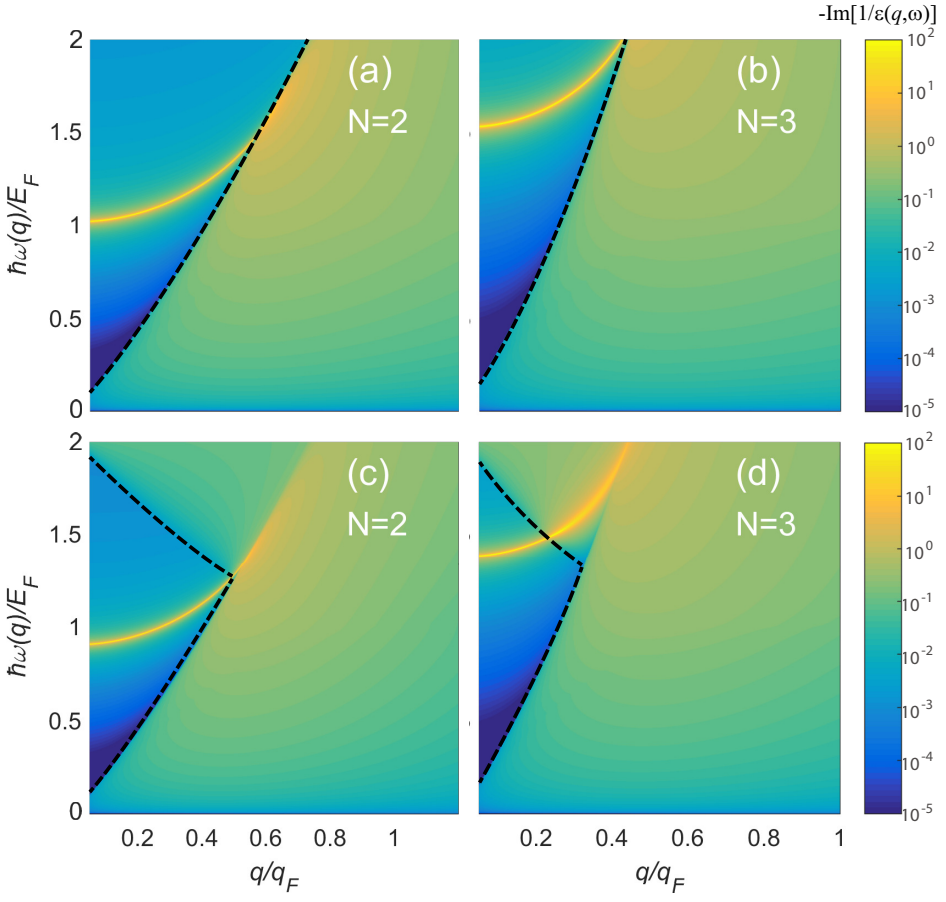

Figure 5.1 The density plots of calculated energy-loss functions in (q,ω) space. (a) and (b) show the loss functions in the absence of chirality for (a) $N = 2$ (parabolic dispersion) and (b) $N = 3$ (cubic dispersion), whereas (c) and (d) show the energy-loss functions in the presence of chirality for (c) $N = 2$ and (d) $N = 3$. The dashed lines represent the boundaries of the intraband and interband electron-hole continua. Note that in the presence of chirality, the plasmon energies are shifted downward for all wave vectors compared with those in the absence of chirality. Here we use the coupling constant $g\alpha = 2.4$, and the Fermi energy $E_{\rm F}/E_0 = 1$ for $N = 2$ and $E_{\rm F}/E_0 = 0.5$ for $N = 3$, respectively.

the plasmon mode), the imaginary part of the inverse dielectric function becomes the Dirac δ-function, i.e., $-\mathrm{Im}[1/\varepsilon(q,\omega)] = W(q)\delta(\omega - \omega_{\mathrm{p}}(q))$ with the strength

$$W(q) = \pi \left\{ \partial \mathrm{Re}[\epsilon(q,\omega)]/\partial\omega|_{\omega=\omega_{\mathrm{p}}(q)} \right\}^{-1}, \tag{5.7}$$

where $\omega_{\mathrm{p}}(q)$ is the plasma frequency at a given wave vector q. Thus, an undamped plasmon shows up as a well-defined δ-function peak in the loss function as indicated by sharp yellow solid lines in Fig. 6.1. The undamped plasmon mode in general carries most of spectral weights and should be observable in experiments (i.e., it is expected that the mode does not decay by electron-hole pairs). The dotted lines in Fig. 6.1 represent the boundaries of the intraband and interband electron-hole single particle excitation (SPE) continua. The electron-hole SPE continua show up as weak broad incoherent structure and carries small spectral weight. When the plasmon mode enters the SPE continuum at the critical wave vector q_{c}, the dielectric function $\epsilon(q > q_{\mathrm{c}}, \omega)$ has a finite imaginary part and the plasmon mode becomes damped via Landau damping. The plasmon mode inside the Landau damping region decays by emitting intraband or interband electron-hole pairs, which is now allowed by energy-momentum conservation. The broadened peaks inside the SPE regions in Fig. 6.1 indicate the damped plasmons. The plasmon energy scaled by the Fermi energy ($\hbar\omega_{\mathrm{p}}/E_{\mathrm{F}}$) is strongly dependent on the band structure. One interesting result is the chirality dependence of the plasmon energy, and it is important to note that in the presence of chirality, plasma frequencies are red-shifted. This is due to the depolarization effect on the plasmon modes, arising from interband transitions.

Figure 6.2 shows the long-wavelength plasma frequencies for $N = 2$ and $N = 3$ as a function of Fermi energy in the presence (red) and absence (blue) of chirality. In this figure the boundary of interband SPE at $q = 0$ is $2E_{\mathrm{F}}$. If the plasma frequency is larger (smaller) than $2E_{\mathrm{F}}$, the plasmon decays (does not decay) by Landau damping. For both $N = 2$ and $N = 3$, $\hbar\omega_{\mathrm{p}}/E_{\mathrm{F}}$ in the absence of chirality increases monotonically with decreasing density and diverges in the low density limit ($E_{\mathrm{F}} \to 0$).

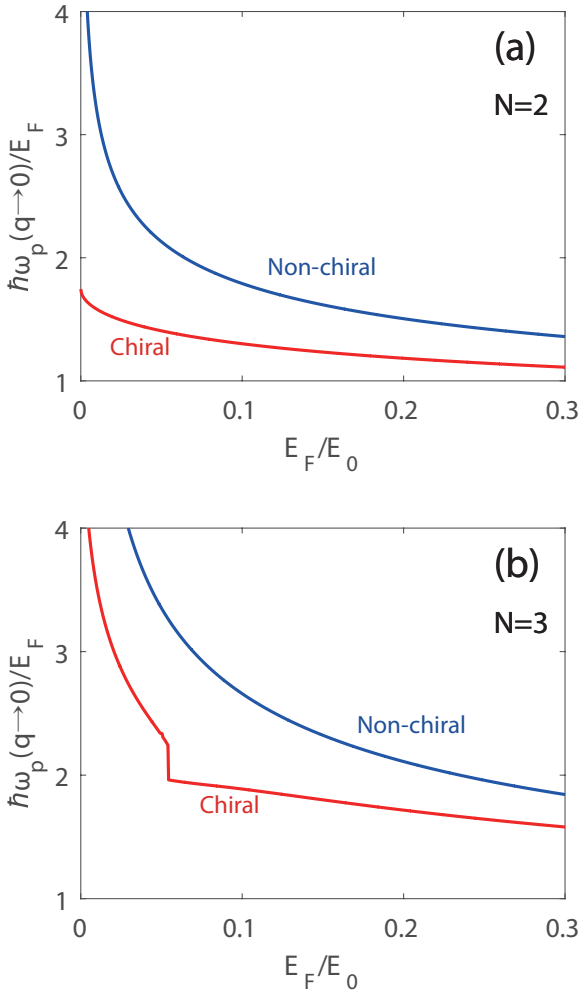

Figure 5.2 Density dependence of the long-wavelength plasma frequencies for (a) $N = 2$ and (b) $N = 3$. Red (Blue) lines correspond to the results in the presence (absence) of chirality. Note that for $N = 2$, $\hbar\omega_{\rm p}/E_{\rm F}$ diverges in the $E_{\rm F} \to 0$ limit in the absence of chirality, whereas it converges to a finite value in the presence of chirality. For $N = 3$, the chiral plasmon dispersion shows a discrete jump at $\hbar\omega_{\rm p} = 2E_{\rm F}$, where plasmons start decaying into electron-hole pair excitations. Here we use the coupling constant $g\alpha = 2.4$.

In the presence of chirality, the plasma frequencies are always smaller than those without chirality, and the energy difference between the two plasmons grows as the carrier density decreases. For $N = 2$, as the density goes to zero, the plasma frequency approaches a finite value less than $2E_{\rm F}$, i.e., $\hbar\omega_{\rm p} \simeq 1.7E_{\rm F}$, indicating that the long-wavelength plasmon does not enter the interband electron-hole continuum for the whole range of densities and thus the plasmon is not damped through the Landau damping. For $N = 3$, the plasma frequency as a function of Fermi energy exhibits a discrete jump at a critical value of $E_{\rm F} = \hbar\omega_{\rm p}/2$, and below the critical value the plasmon energy becomes bigger than $2E_{\rm F}$ and enters into the interband electron-hole continuum decaying via Landau damping. Note that interband transitions are more suppressed at high densities due to Pauli-blocking, which narrows the energy range over which interband transitions can occur. Thus, the effect of interband transition on plasmons becomes weaker at high densities, resulting in small depolarization shift in plasmon energy. For this reason, the signature of chirality in the plasmon dispersions is significant at low densities.

To get further insight into the results shown in Fig. 6.1 , here we present the calculated analytic expressions for the leading-order long-wavelength plasma frequencies (for details, see Appendix C.1),

$$\hbar\omega_{\rm p}^{\rm nch} = E_0\sqrt{\frac{2Ng\alpha}{3\pi}}\left(\frac{E_{\rm F}}{E_0}\right)^{\frac{1+N}{2N}} \tag{5.8}$$

in the absence of chirality and

$$\hbar\omega_{\rm p}^{\rm ch} = \hbar\omega_{\rm p}^{\rm nch}\left[1 + \frac{g\alpha}{3\pi(N-1)}\left(\frac{E_{\rm F}}{E_0}\right)^{\frac{1}{N}-1}\right]^{-\frac{1}{2}} \tag{5.9}$$

in the presence of chirality, where $\alpha = \frac{e^2 k_0}{\kappa E_0}$ is the coupling constant characterizing the interaction strength. The above results are calculated in $E_{\rm F}/E_0 \ll 1$ limit for $N \geq 2$. Note that for $N = 1$ Weyl semimetals a linear band dispersion leads to cut-off dependent long-wavelength plasma frequencies[58, 59]. It is easy to see from

Eq. (5.9) that the plasma frequency with chirality is red-shifted with respect to that without chirality, showing different density dependence at low densities. This difference originates from the interband transition contribution, which appears in the additional term of the polarizability with the opposite sign of the intraband contribution [see Eq. (C.8) in Appendix C.1]. This indicates that interband transitions and associated chiral nature of wavefunctions contribute to the depolarization of the screening and are responsible for the red-shift of the plasma frequencies.

It is interesting that the density dependence of the long wavelength plasma frequencies shown in Eq. (5.8) can be obtained from the classical plasma frequency [60]

$$\omega_{\rm p}^{\rm cl} = \sqrt{\frac{4\pi n e^2}{\kappa m}}, \tag{5.10}$$

where n is the charge carrier density and m is the effective mass of the charge carrier. By using the momentum relation $mv_{\rm F} = \hbar k_{\rm F}$ ($v_{\rm F}$ and $k_{\rm F}$ are the Fermi velocity and the Fermi wave-vector, respectively) and the energy dispersion relation $E_{\boldsymbol{k},\pm} = \pm E_0(|\boldsymbol{k}|/k_0)^N$ for arbitrary band dispersion, the density dependence of the classical plasma frequency can be calculated as

$$\hbar\omega_{\rm p}^{\rm cl} \sim E_{\rm F}^{\frac{1+N}{2N}}, \tag{5.11}$$

which agrees with the full RPA result in Eq. (5.8) for the non-chiral case. Thus, for $N = 1$ we have $\hbar\omega_{\rm p}^{\rm cl} \sim E_{\rm F}$, i.e., the plasma frequency scaled by the Fermi energy is independent of $E_{\rm F}$[61]. For $N \geq 2$, $\hbar\omega_{\rm p}^{\rm cl}/E_{\rm F} \sim E_{\rm F}^{-\alpha}$ with $\alpha = (N-1)/2N$, i.e., the scaled plasma frequency increases as the density (or Fermi energy) decreases and diverge as $E_{\rm F} \to 0$. Note that the interband transition red-shifts the classical plasma frequencies in the presence of chirality.

5.3 The Anisotropic Model

In the previous section we have discussed the plasmon properties of isotropic gapless semimetals. In this section we explore, within the RPA, the plasmon properties of the anisotropic multi-Weyl system whose dispersion is non-linear in the in-plane directions, but linear in the out-of-plane direction.

We consider the following Hamiltonian that describes a multi-Weyl node of order J,

$$H_J^{\rm ch}(\boldsymbol{k}) = E_0 \left[\left(\frac{k_-}{k_0} \right)^J \sigma_+ + \left(\frac{k_+}{k_0} \right)^J \sigma_- + \frac{k_z}{k_0} \sigma_z \right], \tag{5.12}$$

where $\sigma_\pm = \frac{1}{2}(\sigma_x \pm i\sigma_y)$, $k_\pm = k_x \pm i k_y$, and k_0 and E_0 are material dependent parameters. Throughout this section the momentum and the energy are normalized by k_0 and E_0, respectively. With these normalized quantities, we can write the energy dispersion as $E_{\boldsymbol{k},\pm} = \pm E_{\boldsymbol{k}}$, where $E_{\boldsymbol{k}} = \sqrt{k_\parallel^{2J} + k_z^2}$, $k_\parallel = \sqrt{k_x^2 + k_y^2}$ is the in-plane momentum corresponding to non-linear dispersion ($E \sim k_\parallel^J$) in the $x-y$ plane and k_z is the out-of-plane momentum along the z direction where the dispersion is linear ($E \sim k_z$). The overlap factor $F^{ss'}_{\boldsymbol{k},\boldsymbol{k}'}$ is given by

$$F^{ss'}_{\boldsymbol{k},\boldsymbol{k}'} = \frac{1}{2}\left[1 + ss'(\cos\theta\cos\theta' + \sin\theta\sin\theta'\cos J(\phi - \phi'))\right] \tag{5.13}$$

where $\boldsymbol{k} = (k_x, k_y, k_z)$ and $\boldsymbol{k}' = (k'_x, k'_y, k'_z)$ are related to (r, θ, ϕ) and (r', θ', ϕ') through the coordinate transformation, respectively [see Eq. (C.9) in Appendix C.2]. For comparison, we also introduce an anisotropic non-chiral model with the same energy dispersion:

$$H_J^{\rm nch}(\boldsymbol{k}) = E_{\boldsymbol{k}} \sigma_z. \tag{5.14}$$

To investigate the plasmon dispersions and their damping we calculate the energy loss function of the system. Figure 6.3 shows the density plots of the calculated energy loss functions for $J = 2$ in the absence (top panels) and presence (bottom panels) of chirality. Figure 6.3 (a) and (c) show the density plots of the energy loss

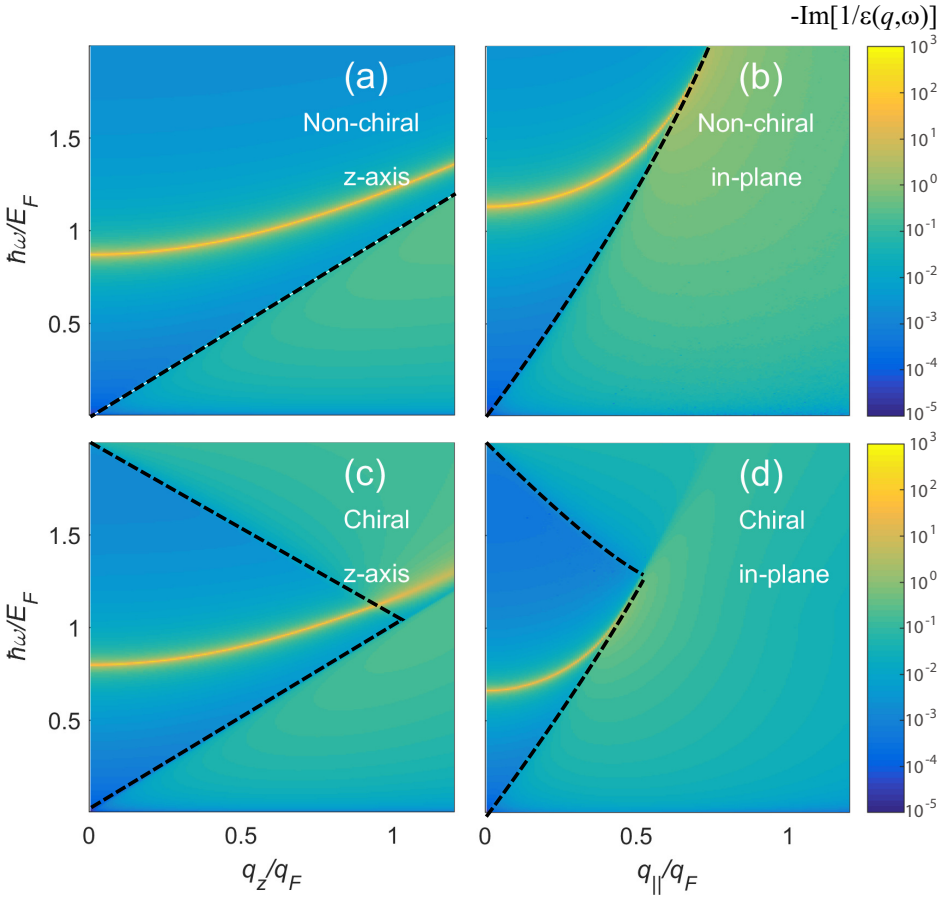

Figure 5.3 Calculated plasmon dispersions (solid yellow lines) for the anisotropic model with $J = 2$ in the absence [top panels, (a) and (b)] and presence [bottom panels, (c) and (d)] of chirality along the z-direction [left panels, (a) and (c)] and the in-plane direction [right panels, (b) and (d)]. Note that plasmon dispersions along the z-direction behave similarly as those for the $N = 1$ isotropic model and plasmon dispersions along the in-plane direction behave as those for the $N = 2$ isotropic model. Plasmon frequencies along both directions are red-shifted in the presence of chirality, as in the isotropic model. Here we use the Fermi energy $E_{\mathrm{F}}/E_0 = 1$ and the coupling constant $g\alpha = 2.4$.

function in (q_z, ω) space for a fixed in-plane wave vector ($q_\parallel = 0$), and Fig. 6.3 (b) and (d) show the density plots of the energy loss function in $(q_\parallel, \omega)$ space for a fixed out of plane wave vector ($q_z = 0$). The yellow lines with the largest spectral weight in the energy loss correspond to the plasmon dispersions of the system. The two most important salient features of the results shown in Fig. 6.3 are following. First, the plasmon dispersions for both in-plane and out-of-plane directions are red-shifted in the presence of chirality, which is consistent with the isotropic results. Second, the plasmon dispersion along the out-of-plane direction (where the band dispersion is linear) shows a similar behavior as that in the $N = 1$ isotropic system. This is because the longitudinal plasmon oscillations propagating along the out-of-plane direction arise from the collective carriers with linear band dispersion and thus their effective motion is essentially identical to those in gapless semimetals with linear dispersion ($N = 1$). The same argument is also applied to the in-plane plasmon modes which propagate along the in-plane direction, where the carriers have the parabolic dispersion and therefore the plasmon dispersion behaves as that in the $N = 2$ isotropic system.

In contrast to the plasmon dispersions, however, the density dependence of the long-wavelength plasmons shows a non-trivial relation between the isotropic and anisotropic models. Figure 6.4 presents calculated long-wavelength plasma frequencies as a function of Fermi energy for $J = 2$ and $J = 3$ in the presence (red) and absence (blue) of chirality. The in-plane plasma frequencies $\hbar\omega_{\rm p}/E_{\rm F}$ [(a) for $J = 2$ and (b) for $J = 3$], show the same behavior as the $N = 1$ isotropic system, i.e., the normalized frequencies are weakly dependent on the carrier density over a wide range both with and without chirality. Note that this behavior is similar to that in gapless semimetals with linear dispersion. For the z-direction [(c) for $J = 2$ and (d) for $J = 3$], $\hbar\omega_{\rm p}/E_{\rm F}$ increases with decreasing Fermi energy in the absence of chirality, and diverges in the $E_{\rm F} \to 0$ limit for both $J = 2$ and $J = 3$. In the presence of

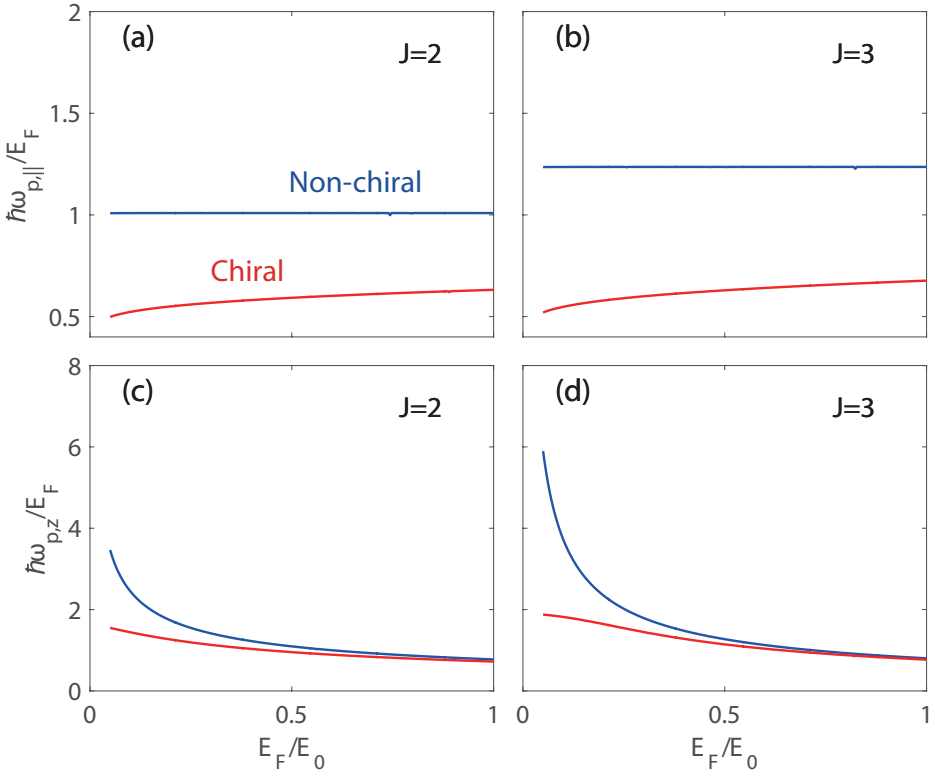

Figure 5.4 Density dependence of the long-wavelength plasma frequencies in the presence (red lines) and absence (blue lines) of chirality for $J = 2$ [left panels, (a) and (c)] and $J = 3$ [right panels, (b) and (d)]. Along the in-plane momentum direction [top panels, (a) and (b)], $\hbar\omega_{\rm p}/E_{\rm F}$ for both $J = 2$ and $J = 3$ behaves as that in Weyl semimetals. Along the z direction [bottom panels, (c) and (d)], for both $J = 2$ and $J = 3$ $\hbar\omega_{\rm p}/E_{\rm F}$ converges to a finite value in the $E_{\rm F} \to 0$ limit. Here we use the coupling constant $g\alpha = 2.4$.

chirality, for $J = 2$ and $J = 3$ it converges to a finite value in the $E_{\rm F} \to 0$ limit. Note that these results are qualitatively similar to the chiral signature of $N = 2$ and $N = 3$ isotropic systems, respectively, as discussed in Sec. II, though here the energy dispersion along the z-direction is linear. It is important to notice that this

result is against our expectations because the density dependence of the anisotropic plasmons along a direction with a specific energy dispersion does not match with the corresponding plasmons in the isotropic model with the same energy dispersion. It should also be noted that for the chiral case anisotropic plasmons along both the in-plane and out-of-plane directions are significantly red-shifted so that they are outside the electron-hole continua for a broad range of density and coupling strength. For $J = 3$ plasmons, this is in sharp contrast to the counterpart of the isotropic case ($N = 3$), where plasmons exhibit a discrete jump merging into the electron-hole continua at a critical Fermi energy.

Here we analyze the previous numerical results in Fig. 6.4 with analytical expressions. Similarly as the isotropic case, we can also derive long-wavelength plasma frequencies from the linear response theory in the many-body approach. In the absence of chirality, we obtain plasma frequencies for the anisotropic model to be

$$\omega_{\mathrm{p},\parallel} = \sqrt{\frac{2g\alpha J}{3\pi}} E_{\mathrm{F}} \tag{5.15}$$

along the $k_{\parallel}$ momentum direction and

$$\omega_{\mathrm{p}} = \sqrt{\frac{g\alpha\Gamma\left(1+\frac{1}{J}\right)}{2\sqrt{\pi}\Gamma\left(\frac{3}{2}+\frac{1}{J}\right)}} E_{\mathrm{F}}^{1/J} \tag{5.16}$$

along the k_z momentum direction. The difference in density dependence between the two plasma frequencies can also be understood by the classical derivation of plasma frequency, as in the isotropic case. Since the density of states of the anisotropic model in Eq. (B.20) is calculated to be $D(E) \sim E^{2/J}$, the total carrier density n becomes $n \sim E_{\mathrm{F}}^{\frac{2+J}{J}}$. Since the energy dispersion is anisotropic, it is expected that the effective mass is also anisotropic. Thus, electrons would effectively behave as if they have the energy dispersion $E \sim k_{\parallel}^{J}$ with $m \sim E_{\mathrm{F}}^{\frac{2-J}{J}}$ along the in-plane $k_{\parallel}$ momentum direction, and $E \sim k_z$ with $m \sim E_{\mathrm{F}}$ for the out-of-plane k_z momentum direction. Putting n and m into Eq. (5.10), we can obtain the Fermi energy dependence of the

plasma frequency in classical limit:

$$\hbar\omega_{\mathrm{p},\|} \sim E_{\mathrm{F}} \tag{5.17}$$

along the $k_{\|}$ momentum direction and

$$\hbar\omega_{\mathrm{p},z} \sim E_{\mathrm{F}}^{1/J} \tag{5.18}$$

along the k_z momentum direction. The density dependence of plasmons obtained from both classical and quantum mechanical approaches are consistent with the numerical results in Fig. 6.4. Note that as in the case of the isotropic system, the density dependence of classical plasma frequencies is in good agreement with that of the non-chiral plasmon.

5.4 Summary and Conclusion

In this chapter, we investigate theoretically electronic collective modes of 3D chiral gapless electron-hole systems and find the wave vector dependent plasmon dispersion. We have calculated long-wavelength plasma frequencies and their density dependence both in semimetals with an isotropic band dispersion and in multi-Weyl semimetals with an anisotropic band dispersion. We find that the interband transition associated with chirality leads to the depolarization shift of plasma frequencies irrespective of band dispersion.

For the isotropic parabolic dispersion ($N = 2$), the depolarization shift of the long-wavelength plasmons arises from the interband electron-hole transition and the plasmons lie outside the interband electron-hole continuum (i.e., $\hbar\omega_{\mathrm{p}} < 2E_{\mathrm{F}}$). Thus, the plasmons do not decay via Landau damping. For the cubic dispersion ($N = 3$), we find that the plasma frequency ($\hbar\omega_{\mathrm{p}}/E_{\mathrm{F}}$) increases as the density decreases and enters the interband single particle excitation region at a critical carrier density showing a discrete energy jump.

For the anisotropic dispersion, we have calculated the plasma frequencies in a system with a linear band dispersion along one specific direction and non-linear dispersion in the other remaining directions. We find that the density dependence of the long-wavelength plasma frequency along the direction of non-linear dispersion shows a similar behavior as that of the linear band isotropic model ($N = 1$), in which $\hbar\omega_{\rm p}/E_{\rm F}$ depends weakly on the density over a wide range of Fermi energies. On the other hand, the density dependence of the long-wavelength plasma frequency along the direction of linear dispersion shows a similar behavior as that of the isotropic model with the non-linear dispersion. The long-wavelength plasmons along all the directions are undamped due to the chirality induced red-shift of plasma frequencies.

Our predicted plasmon properties clearly distinguish gapless semimetals from the extensively studied usual parabolic 3D electron systems. We believe that our predictions can be tested in doped gapless semimetals using inelastic light scattering [47–49] and electron scattering [50–54] spectroscopies.

Chapter 6

Inelastic carrier lifetime in a coupled graphene

6.1 Introduction

Two-dimensional (2D) graphene has been extensively studied during recent years because of its fundamental and technological interest. [62, 63] Although it is possible to grow graphene on non-polar substrates,[64] in most currently available graphene samples (e.g., graphene field-effect transistors) graphene lies on top of a polar substrate such as SiO_2,[65–67] SiC,[68–71] hBN[72–75] or HfO_2.[76] In such graphene samples the polar optical phonons of the substrate are localized near the graphene-substrate interface, and free carriers in graphene couple to the surface polar (SO) phonons of the underlying substrate through the long-range polar Fröhlich coupling. In polar materials the longitudinal optical (LO) phonons generate a long-range electric field which scatters electrons, and typically their contribution to resistivity is dominant at room temperatures. [55] In non-polar materials such as graphene, however, the non-polar optical phonons have little effect on carrier transport because the

long-range interaction between electrons and phonons is absent and the energy of the (non-polar) optical phonon is very high, ∼200 meV. In addition, contributions from acoustic phonons[77–80] are relatively small because the electron-acoustic-phonon coupling is rather weak in graphene due to the small deformation potential.[81–84] For this reason, the SO phonons rather than non-polar LO or acoustic phonons can be the dominant scattering source at room temperature in graphene on a polar substrate. [65, 76, 85]

In addition to being the main scattering source in transport, it is well known that in polar materials the electron-polar-optical-phonon interaction leads to polaronic many-body renormalization of the single particle properties, e.g., polaronic Fermi velocity (effective mass) renormalization and broadening of the quasiparticle spectral function.[42, 86–89] Even though these effects are expected to be small in graphene due to the weak Fröhlich coupling arising from the spatial separation between electrons in graphene and the surface of a substrate and due to the large dielectric constant of the substrate, there is a much stronger quantitative manifestation of electron-SO-phonon coupling in graphene on a polar substrate, which is the macroscopic coupling of the electronic collective modes (i.e., plasmons) to the SO phonons of the system via the long-range Fröhlich coupling. This mode coupling phenomenon, which hybridizes the collective plasmon modes of the electron gas with the SO-phonon modes of the substrate, gives rise to coupled plasmon-phonon modes, which have been extensively studied both experimentally[67, 70, 71, 90, 91] and theoretically[92–94] in graphene. The plasmon-phonon coupling is important in many single-particle properties including the inelastic carrier life time, hot-electron energy-loss processes, and transport properties.

In this section, we provide the inelastic carrier lifetime and the inelastic mean free path of monolayer and bilayer graphene in the presence of the long-range polar Fröhlich coupling between electrons in graphene and SO phonons in the underlying

polar substrate within the leading-order perturbation theory, i.e., G_0W approximation. We consider the effective total interaction (i.e., the coupled electron-electron and electron-SO-phonon interaction) within the framework of the random phase approximation (RPA). Even though the problem is treated within the G_0W framework of the leading-order effective interaction approximation, our results should be quite valid in graphene because graphene has a very weak Fröhlich coupling, which justifies the neglect of the electron-phonon vertex corrections. We include, however, important physical effects of the dynamical screening, phonon self-energy correction, plasmon-phonon mode coupling, and Landau damping. In the presence of electron-SO-phonon coupling we find added features in the inelastic carrier lifetime, which are obviously absent without the coupling.

There have been several studies upon the effects of electron-SO-phonon interaction in graphene.[95–98] Various many-body quantities such as- the self-energy, scattering rate, and spectral function have been calculated for the statically screened electron-SO- phonon interaction. Such calculations based on the static screening approximation are justified when the charge carrier density is high enough that the corresponding Fermi energy exceeds the SO phonon energy. However, the SO phonon energies of the common polar substrates for graphene such as SiC or SiO_2 range from 50 to 200 meV, and they are comparable to the typical Fermi energies of graphene, 100 – 300 meV. Thus the dynamic screening of the electron-SO- phonon interaction is more desirable. [94] In addition, because the SO phonon energy and the energy of electrons are comparable, we cannot treat the electron-electron interaction and the electron-SO phonon interaction separately. Therefore, we need to treat both interactions equivalently within the same dynamic screening approximation. Quasiparticle properties of various systems have been calculated considering both electron-electron and electron-phonon interactions.[99, 100] However, there appears to be a lack of calculation of quasiparticle properties of graphene on a polar substrate with both

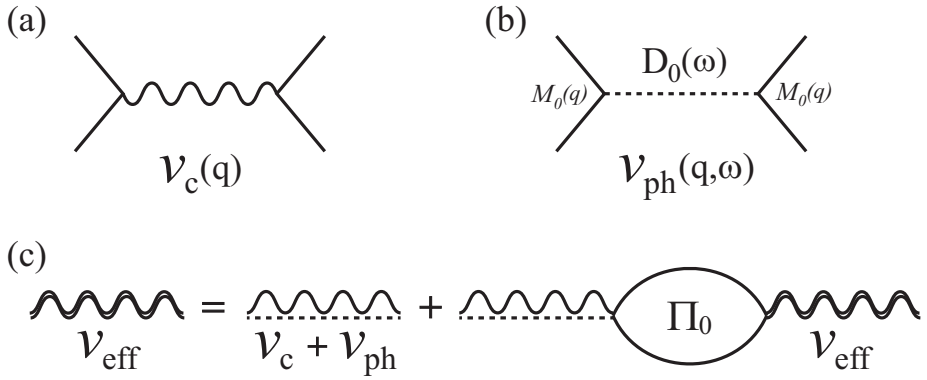

Figure 6.1 (a) Electron-electron Coulomb interaction. (b) Phonon mediated electron-electron interaction. (c) Series of diagrams corresponding to the RPA for the effective interaction in the presence of both electron-electron and electron-phonon interactions. The wiggly (dashed) line represents the electron-electron Coulomb (SO phonon mediated) interaction and Π_0 the bare polarizability.

electron-electron and electron-SO-phonon interactions equally treated.

In this chapter, we calculate the scattering rate (τ^{-1}) and the corresponding inelastic mean free path (l) of quasiparticles in both monolayer and bilayer graphene by taking into account both electron-electron and electron-SO-phonon interactions. We also investigate the effect of the dynamic screening of the electron-SO-phonon interaction and plasmon-phonon coupling. In addition, we propose a possible technological application to a lateral hot-electron transistor by making use of the electron-SO-phonon interaction effect. Throughout the chapter, we refer to the graphene system with both electron-electron and electron-SO-phonon interactions as the coupled system, whereas the graphene system with only the electron-electron interaction as the uncoupled system.

6.2 Theory

We consider the two component effective Hamiltonian for both monolayer and bilayer graphene, which is given by[101, 102]

$$H_J(\boldsymbol{k}) = t_\perp \left(\frac{\hbar v|\boldsymbol{k}|}{t_\perp}\right)^J \tag{6.1}$$

where $J=1(J=2)$ corresponds to monolayer (bilayer) graphene, $t_\perp$ is the nearest interlayer hopping, v is the in-plane velocity of monolayer graphene, $|\boldsymbol{k}| = \sqrt{k_x^2+k_y^2}$ and $\phi_{\boldsymbol{k}} = \tan^{-1}(k_y/k_x)$. The corresponding energy eigenvalues and eigenfunctions are given by $\varepsilon_{\boldsymbol{k},s} = st_\perp(\hbar v|\boldsymbol{k}|/t_\perp)^J$ and $|s,\boldsymbol{k}\rangle = \frac{1}{\sqrt{2}}\left(s, e^{iJ\phi_{\boldsymbol{k}}}\right)$ where $s=\pm 1$ are band indices.

For monolayer graphene, this model holds over the Fermi energy range limited by intralayer coupling (γ_0 $\sim$3 eV) while for bilayer graphene it is valid for the Fermi energy range limited by the interlayer coupling (γ_1 $\sim$0.4 eV), which is still within the range we are considering in this work. Note that if the Fermi energy or the corresponding carrier density is high enough, the interlayer hopping $t_\perp$ can be negligible and the bilayer graphene is simply described by a collection of two monolayer graphene sheets. We will discuss the high carrier density limit in bilayer graphene later.

In the coupled system, electrons interact with each other through the direct Coulomb interaction $v_c(q) = 2\pi e^2/\epsilon_\infty q$ [Fig. 6.1(a)] and the SO-phonon-mediated interaction $v_{\rm ph}(q,\omega) = M_0^2(q)D_0(\omega)$ [Fig. 6.1(b)]. Here the electron-SO phonon coupling $M_0(q)$ is given by[42]

$$M_0^2(q) = v_c(q)\alpha e^{-2qd}\frac{\omega_{\rm SO}}{2}, \tag{6.2}$$

where d is the distance between the graphene and the polar substrate,

$$\alpha = \epsilon_\infty\left[\frac{1}{\epsilon_\infty+1} - \frac{1}{\epsilon_0+1}\right], \tag{6.3}$$

ϵ_0 (ϵ_∞) is the zero- (high) frequency dielectric constant, and $D_0(\omega)$ is the bare SO-phonon propagator given by

$$D_0(\omega) = \frac{2\omega_{\rm SO}}{\omega^2 - \omega_{\rm SO}^2}. \tag{6.4}$$

Within the RPA the effective electron-electron interaction is obtained from the sum of all bare bubble diagrams [Fig. 6.1(c)] and is given by

$$v_{\rm eff}(q,\omega) = \frac{v_c(q) + v_{\rm ph}(q,\omega)}{1 - [v_c(q) + v_{\rm ph}(q,\omega)]\,\Pi_0(q,\omega)} = \frac{v_c(q)}{\epsilon_{\rm t}(q,\omega)}, \tag{6.5}$$

where $\Pi_0(q,\omega)$ is the bare polarizability of graphene. Thus the total dielectric function from electrons and SO phonons is given by[92]

$$\begin{aligned}\epsilon_{\rm t}(q,\omega) &= 1 - v_c(q)\Pi_0(q,\omega) + \frac{M_0^2(q)D_0(\omega)}{v_c(q) + M_0^2(q)D_0(\omega)} \\ &= 1 - \frac{2\pi e^2}{\epsilon_\infty q}\Pi_0(q,\omega)\frac{\alpha e^{-2qd}}{1 - \alpha e^{-2qd} - \omega^2/\omega_{\rm SO}^2}.\end{aligned} \tag{6.6}$$

Here for simplicity we use the zero-temperature polarizability as an approximation, which is valid in monolayer graphene at typical doping densities $n = 10^{11}$–10^{13} cm^{-2} because the corresponding Fermi temperature $T_{\rm F} = 400$–4000 K is much larger than room temperature. On the other hand, in bilayer graphene the Fermi temperature at low densities $n \sim 10^{11}$ cm^{-2} ($T_{\rm F} \sim 40$ K) is smaller than room temperature, and thus the zero temperature approximation is valid only at relatively high densities $n > 10^{12}$ cm^{-2}($T_{\rm F} \sim 400$ K) in bilayer graphene.

Alternatively, the effective interaction $v_{\rm eff}(q,\omega)$ can be written as the sum of the screened electron-electron Coulomb interaction and the screened electron-SO phonon interaction, [42, 99]

$$v_{\rm eff}(q,\omega) = \frac{v_c(q)}{\epsilon(q,\omega)} + v_{\rm ph}^{\rm sc}(q,\omega), \tag{6.7}$$

where $\epsilon(q,\omega)$=$1-v_c(q)\Pi_0(q,\omega)$ is the electronic dielectric function within the RPA.[**diel**] The screened electron-SO phonon interaction is given by $v_{\rm ph}^{\rm sc}(q,\omega) = [M(q,\omega)]^2 D(q,\omega)$

where $M(q,\omega) = M_0(q)/\epsilon(q,\omega)$ is the screened interaction matrix element and $D(q,\omega)$ is the renormalized phonon propagator given by

$$D(q,\omega) = \frac{D_0(\omega)}{1 - [M_0(q)]^2 D_0(\omega)\Pi_0(q,\omega)/\epsilon(q,\omega)}. \tag{6.8}$$

Note that the interaction between electrons and SO-phonons is dynamically screened. The effect of dynamic screening in contrast to that of the static screening will be discussed later.

The self-energy of the coupled system within the G_0W approximation is given by [103]

$$\begin{aligned}\mathrm{Im}[\Sigma_s^{\mathrm{t}}(\boldsymbol{k},\omega)] = & \sum_{s'} \int \frac{d^2q}{(2\pi)^2} \left[\Theta(\omega - \xi_{\boldsymbol{k}+\boldsymbol{q},s'}) - \Theta(-\xi_{\boldsymbol{k}+\boldsymbol{q},s'})\right] \\ & \times \ \mathrm{Im}[v_{\mathrm{eff}}(q,\omega)]\, F_{ss'}(\boldsymbol{k},\boldsymbol{k}+\boldsymbol{q}),\end{aligned} \tag{6.9}$$

where $F_{ss'}(\boldsymbol{k},\boldsymbol{k}+\boldsymbol{q}) = \frac{1}{2}(1 + ss'\cos J\theta_{\boldsymbol{k},\boldsymbol{k}+\boldsymbol{q}})$ is the wavefunction overlap factor and $\theta_{\boldsymbol{k},\boldsymbol{k}+\boldsymbol{q}}$ is the angle between $\boldsymbol{k}$ and $\boldsymbol{k}+\boldsymbol{q}$. Within the on-shell approximation, ω is substituted by the on-shell energy $\xi_{\boldsymbol{k},s} = \varepsilon_{\boldsymbol{k},s} - \mu$ where μ is the chemical potential. The scattering rate is given by the imaginary part of the self-energy via the relation $\hbar/\tau = -2\mathrm{Im}[\Sigma_s^{\mathrm{t}}]$.

6.3 Results

6.3.1 Scattering rate

For numerical calculations, the parameters[104] corresponding to SiC are used throughout this chapter: $\hbar\omega_{\mathrm{SO}} = 116.7$ meV, $\epsilon_\infty = 6.4$, $\epsilon_0 = 10.0$, and $d = 5$ Å. Figures 6.2(a) and (b) show the scattering rates for uncoupled and coupled monolayer graphene as a function of the on-shell energy $\xi_{\boldsymbol{k}}$. As in the case of the 2D electron gas with the parabolic energy dispersion, the scattering rate vanishes at the Fermi energy (i.e., $\xi_{\boldsymbol{k}} = 0$) and shows the well-known quadratic behavior of $\sim |\xi_{\boldsymbol{k}}|^2 \ln|\xi_{\boldsymbol{k}}|$ near

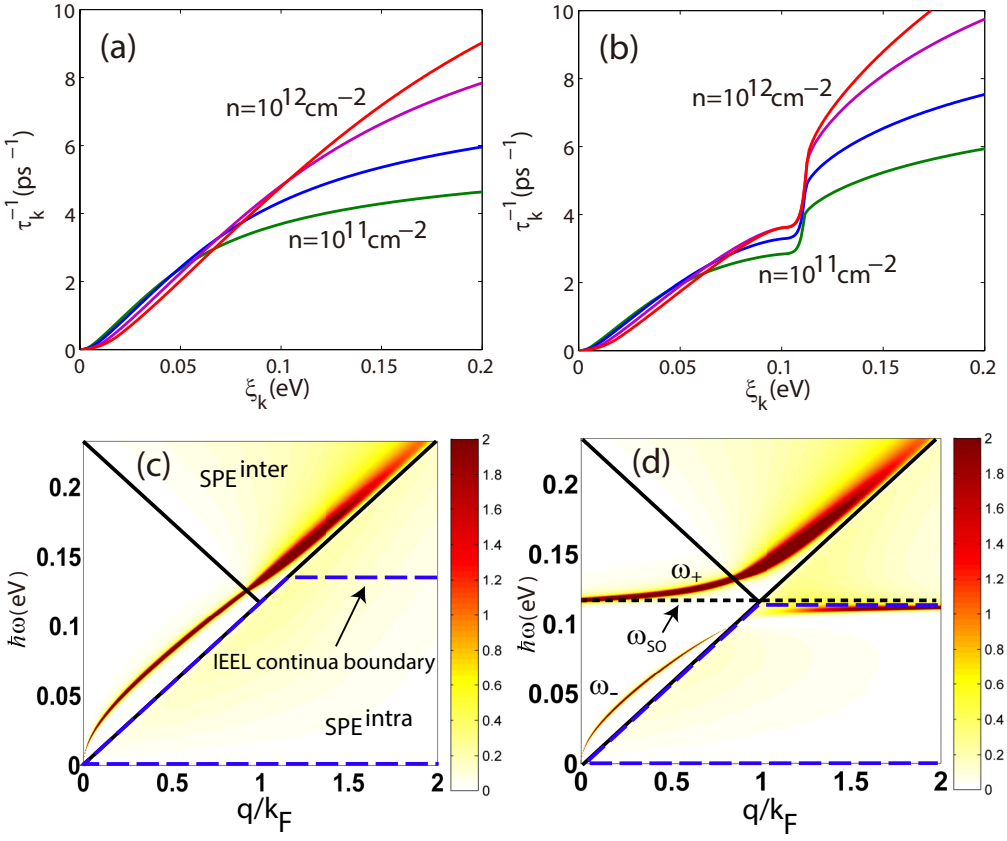

Figure 6.2 (Color online) (a) Calculated scattering rate as a function of the on-shell energy $\xi_{\boldsymbol{k}}$ for different carrier densities $n = (1, 2, 5, 10) \times 10^{11}$ cm^{-2} for (a) uncoupled and (b) coupled monolayer graphene ($J = 1$), and calculated energy-loss function for (c) uncoupled and (d) coupled monolayer graphene at $n = 10^{12}$ cm^{-2}. The dotted horizontal line in (d) represents the SO phonon frequency, and the dashed line represents the boundary of the IEEL continua for an electron injected with the energy 140 meV (c) and 106 meV (d). SPE$^{\text{intra}}$ (SPE$^{\text{inter}}$) represents the single-particle excitation region for the intraband (interband) electron-hole excitations. Note that for the coupled system the plasmon dispersion is partly covered by the IEEL continua and thus a decay process via plasmon emission is available.

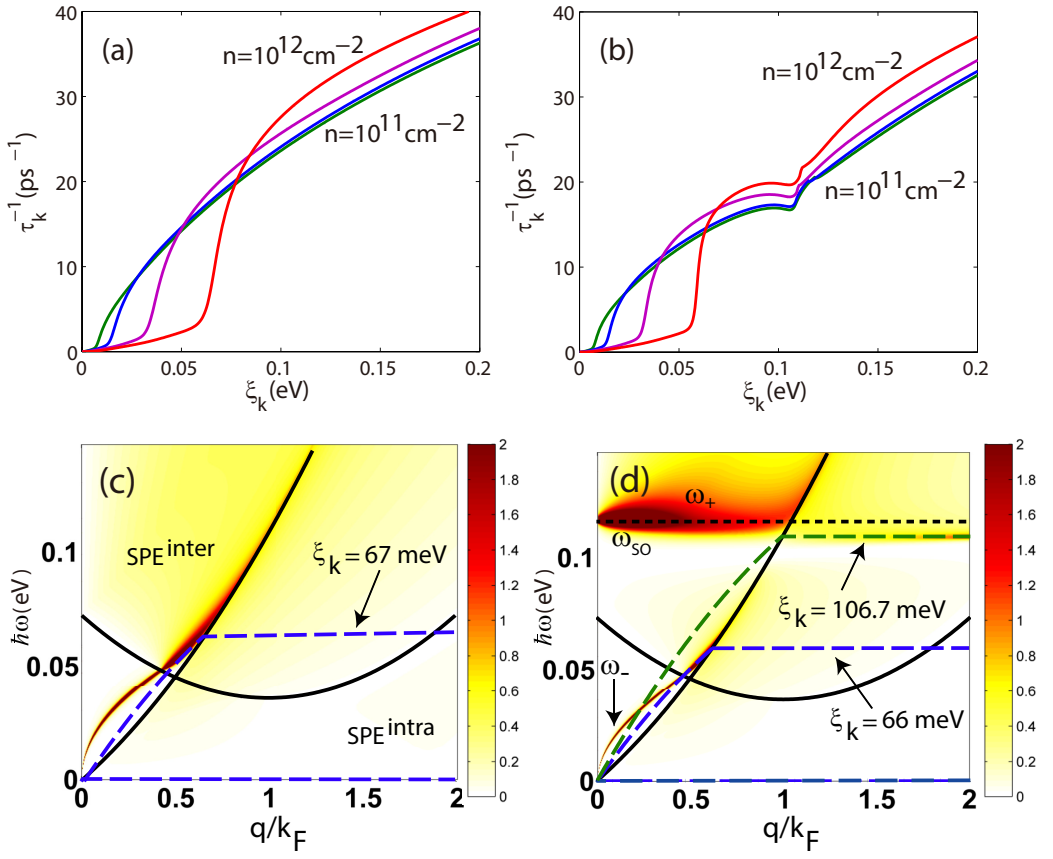

Figure 6.3 (Color online) Calculated scattering rate as a function of $\xi_{\boldsymbol{k}}$ for different carrier densities $n = (1, 2, 5, 10) \times 10^{11}$ cm^{-2} for (a) uncoupled and (b) coupled bilayer graphene ($J = 2$), and calculated energy loss function for (c) uncoupled and (d) coupled bilayer graphene at $n = 10^{12}$ cm^{-2}. In (d), the IEEL continua are drawn for two different energies of an injected electron: $\xi_{\boldsymbol{k}} = 66$ meV (blue dashed line) and $\xi_{\boldsymbol{k}} = 106.7$ meV (green dashed line). At these energies, the scattering rate increases sharply because of the decay via the emission of the plasmonlike mode and phononlike mode, respectively, as shown in (b).

the Fermi energy. Away from the Fermi energy, an upward kink structure appears in the scattering rate for the coupled system, whereas the uncoupled system shows no such structure at any energy. Figures 6.2(c) and 2(d) show the calculated loss functions –Im$[1/\epsilon_{\rm t}(q,\omega)]$ of the uncoupled and coupled monolayer graphene for carrier density $n = 10^{12}$ cm^{-2} along with the single-particle excitation (SPE) and the injected-electron energy loss (IEEL) continua. The loss function describes electronic energy dissipation and its poles represent the dissipation via plasmon excitations. The intersections of the IEEL continua with the SPE continua indicate the allowed quasiparticle decay via electron-hole pair excitations while the intersections of the IEEL continua with the plasmon lines indicate the allowed quasiparticle decay via the emission of plasmons. Note that the volume of the IEEL continua depends on the energy with which an electron is injected. Hence, an injected electron with a higher energy can have more routes to decay than that injected with a low energy.

For the uncoupled monolayer graphene, the quasiparticle cannot decay via plasmon emission because the plasmon dispersion does not enter the IEEL continua over the whole energy range, as shown in Fig. 6.2(c). Thus the scattering rate in doped graphene does not show an abrupt increase at any energy.[103] On the other hand, as shown in Fig. 6.2(d), for the coupled system there are two modes: the phononlike mode ω_+ and the plasmonlike mode ω_-. The plasmonlike mode w_- enters the IEEL continua at a finite critical wave vector $q_c \approx \omega_{\rm SO}(1-\alpha)/v$.[92] Thus an additional decay channel via ω_- emission is turned on around the SO phonon energy $E_{\rm SO} = \hbar\omega_{\rm SO}$, leading to an upward step in the scattering rate. Note that decay via the emission of the phononlike mode ω_+ is impossible for monolayer graphene because the ω_+ mode increases linearly at large q with energy slightly higher than that of the uncoupled plasmon mode and thus it does not enter the IEEL continua.

Figure 6.3 shows the scattering rate and the loss function in uncoupled and coupled bilayer graphene. Unlike the situation with monolayer graphene, the plas-

mon dispersions for both uncoupled and coupled bilayer graphene enter the IEEL continua. Therefore, even in the uncoupled system the scattering rate exhibits an abrupt increase, which is absent in the uncoupled monolayer system. In addition, while the coupled monolayer graphene system has only a single jump in the scattering rate, the coupled bilayer graphene shows two abrupt jumps. One of them occurs near $\xi_{\boldsymbol{k}} \approx E_{\mathrm{SO}}$, for which the emission of the phononlike mode ω_+ damped in the interband SPE is responsible. The other jump occurs due to the emission of the plasmonlike mode ω_- and its threshold energy strongly depends upon the carrier density, hence the emission of the plasmonlike mode ω_- is tunable with a carrier density. At higher carrier densities ($E_{\mathrm{F}} > E_{\mathrm{SO}}$) the plasmon is strongly coupled to the SO phonon and the threshold energy for the phononlike mode ω_+ becomes a tunable quantity while the threshold energy for the plasmonlike ω_- is fixed around the SO phonon energy E_{SO}.[92] Note that in bilayer graphene the step of the scattering rate at the phononlike mode shows a weaker density dependence on the carrier density than that in monolayer graphene because of the constant density of states. Also note that our calculation for bilayer graphene is based on the two band model which is valid only at low carrier densities. At high enough carrier densities, the interlayer coupling becomes negligible and the energy band structure of bilayer graphene behaves as a collection of monolayer graphene sheets, thus we expect that the results for bilayer graphene are similar to those of monolayer graphene. At such high densities, the density-dependent jump would disappear and only one single jump around E_{SO} would be found in the scattering rate, as in the monolayer case. We also note that high-energy plasmon modes are known to exist in bilayer graphene.[105–107] When an electron is injected with sufficiently high energies, a decay through the emission of the high-energy plasmon modes could be possible, leading to additional jumps in the scattering rate. Such jumps are not captured by the two-band effective model and thus beyond the scope of this work.

6.3.2 Mean free path

The inelastic mean free paths $l_k = v_k \tau_k$ of the uncoupled and coupled monolayer graphene systems are given in Fig. 6.4(a). Unlike the uncoupled system, the coupled system shows a sharp decrease in the inelastic mean free path at the SO phonon energy E_{SO} at which the emission of plasmonlike mode is turned on and an electron loses its energy significantly. Thus, by injecting an electron below or above E_{SO}, we can change the mean free path of the system significantly, which can be used for designing a lateral hot electron transistor device in the coupled monolayer graphene system.[108–110] Figure 6.4(b) shows the inelastic mean free path for bilayer graphene systems. The mean free path in bilayer graphene is much shorter than that in monolayer graphene and the step of the mean free path is very small around E_{SO}. Thus the bilayer graphene may not be a good candidate for the application to a lateral hot electron transistor utilizing the electron-phonon interaction. At low energies, however, the inelastic mean free path strongly depends on the carrier density because the threshold energy of the plasmonlike mode w_- is approximately proportional to the Fermi energy. Thus, by changing the carrier density, we can activate or deactivate the decay process via emission of the plasmonlike mode w_-, which is possible even in the uncoupled system without SO phonons. With the help of density tunability through gating, we can achieve a significant change in the mean free path. We find that the mean free path of an electron with an energy $\xi_{\boldsymbol{k}} \approx 0.1$ eV at the carrier density $n \sim 10^{12}$ cm^{-2} is $l \sim 10^2$ nm but $l \sim$1–10 nm at $n \sim 10^{11}$ cm^{-2}. This promises a possible use of bilayer graphene as a lateral-hot electron transistor in the absence of electron-SO-phonon coupling.

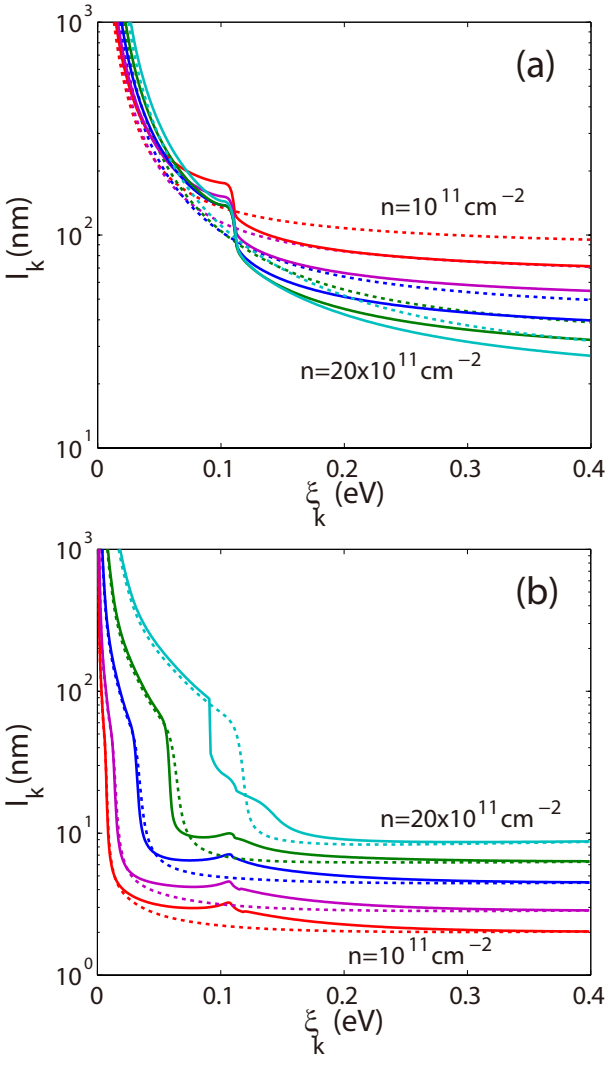

Figure 6.4 (Color online) Calculated mean free path as a function of $\xi_{\boldsymbol{k}}$ for different carrier densities $n = (1, 2, 5, 10, 20) \times 10^{11}$ cm^{-2} for (a) monolayer graphene and (b) bilayer graphene. The solid (dotted) lines represent the mean free paths in the presence (absence) of the electron-SO-phonon coupling.

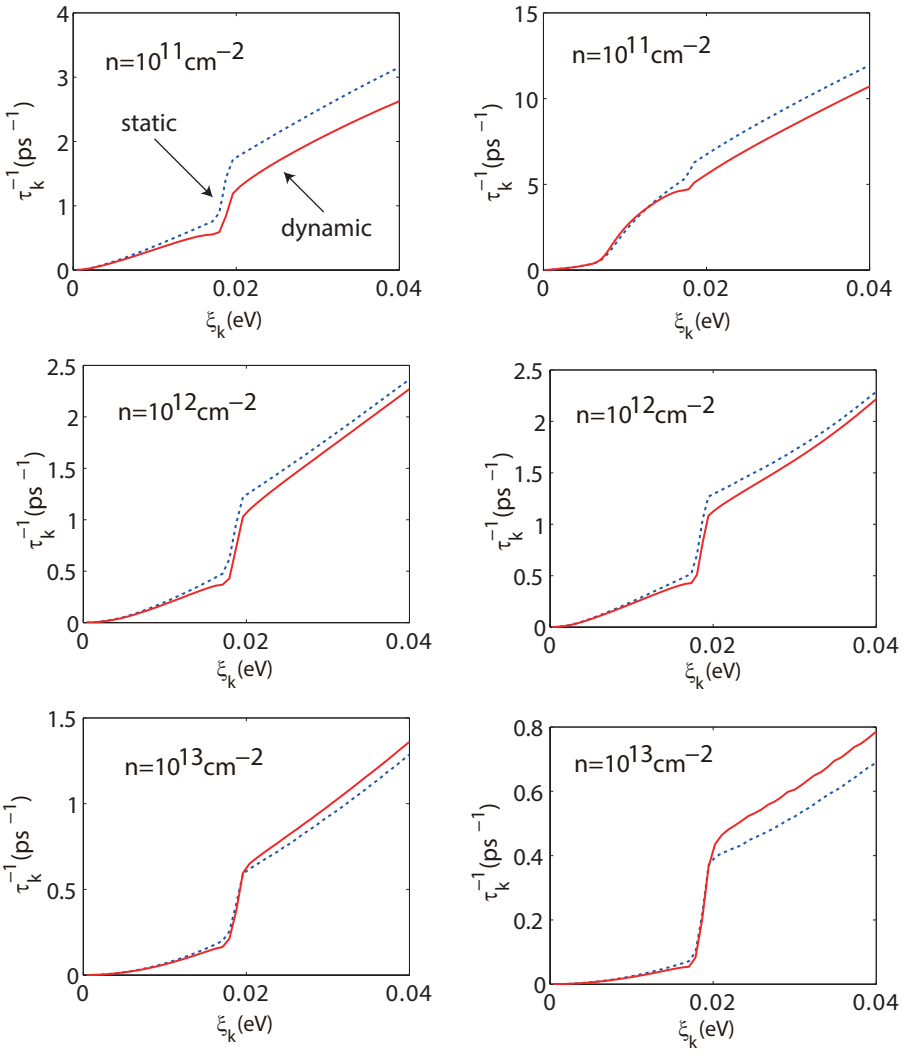

Figure 6.5 Calculated scattering rate as a function of $\xi_{\boldsymbol{k}}$ for different carrier densities $n = 10^{11}, 10^{12}, 10^{13}$ cm^{-2} for monolayer graphene (left column) and for bilayer graphene (right column). The solid (dotted) lines represent the scattering rates with dynamically (statically) screened electron-SO-phonon interaction. Here $\hbar\omega_{\rm SO} = 20$ meV is used for this calculation.

6.4 Discussion and Summary

In the previous section we showed the self-energy calculated with dynamical RPA screening. In this section we discuss the effect of dynamical screening of the electron-SO-phonon interaction compared with the results calculated with static screening. We also discuss the effects of finite SO-phonon lifetime and multiple SO-phonon modes of the polar substrate.

The static screening is equivalent to putting $\omega = 0$ in $\Pi_0(q, \omega)$ in Eq. (6.8), which means that the electrons screen the SO phonons statically, while electron-electron interactions are treated dynamically to take into account the plasmon effects. Figure 6.5 shows the scattering rates for different carrier densities in monolayer and bilayer graphene with the static or dynamic screening approximations. We find that at low densities the scattering rates with static screening are larger than those with dynamic screening for both monolayer and bilayer graphene, while at high densities the results with dynamic screening are larger than those with static screening. These effects may arise from the attractive nature of the phonon-mediated effective interaction, which originates from the retardation effect coming from the mass difference between ions and electrons. At low densities, the negative contribution to the scattering rate from the attractive effective interaction is significant, and the static screening suppresses the negative contribution more strongly than the dynamic screening, giving a larger scattering rate. As the carrier density increases, the negative contribution to the scattering rate becomes negligible, and the scattering rate with the static screening approximation becomes smaller than that with the dynamic screening, as shown in the bottom panel of 6.5.

In our calculations, we assume an infinite lifetime for SO phonons because the inclusion of the finite lifetime just suppresses the jumps in the scattering rate without making any qualitative change. Furthermore, the typical decay rates of SO phonons are so small ($\sim$1 meV) compared to SO phonon energies that the effect of the finite

phonon lifetime is quantitatively negligible.

We also assume in our calculations that only one single SO phonon mode is present in substrates. If multiple SO phonon modes exist, as in SiO_2, each mode couples to the electron motion independently, giving a jump in the scattering rate near the phonon mode energy. Our results based on one single phonon mode correspond to each of these jumps, and thus extension to multiple phonon modes from our results is trivial.

In conclusion, we theoretically calculated the inelastic scattering rates τ^{-1} and the hot-electron inelastic mean free paths l for both monolayer and bilayer graphene on a substrate made of polar materials, treating the electron-electron interaction and the electron-SO-phonon interaction on an equal footing. In our theoretical calculation, we include the interaction between electrons, SO phonons, and plasmons within the RPA (for dynamical screening and phonon self-energy correction) and within the leading-order self-energy in the effective total interaction. We find that the strong coupling between the SO phonon and the plasmon leads to an additional decay channel for the quasiparticles through the emission of the coupled mode and gives rise to an abrupt increase in the scattering rate, which is absent in the uncoupled system. In monolayer graphene a single jump in the scattering rate occurs around E_{SO}, arising from the emission of the low energy branch of the coupled modes. By varying the energy of an injected electron, we can change the mean free path significantly. In bilayer graphene the emission of both low and high energy branches of the coupled modes contributes to the scattering rate, and gives rise to two abrupt changes in the scattering rate. In particular, in bilayer graphene, the emission of the plasmonlike mode depends strongly on the carrier density while the threshold energy for the emission of the phononlike mode is weakly dependent on the carrier density and fixed at E_{SO}. Utilizing the density dependence of the plasmonlike mode, we can achieve a significant difference in the mean free path by varying the carrier

density.

With the help of the abrupt changes in τ^{-1} and l near E_{SO}, our results for both monolayer and bilayer graphene are applicable to making an electronic device by varying the energy of an injected electron near E_{SO} or tuning the carrier density.

It may be possible to fabricate a hot-electron transistor device with a sudden onset of negative differential resistance associated with sharp changes in the inelastic mean free path due to electron-coupled-mode scattering of the injected electrons.

Chapter 7

Conclusion

The main focus of my doctoral research has been on optical properties and interaction-induced collective phenomena in materials that exhibit Dirac like physics in their low energy excitations. We specifically investigated two emerging Dirac materials: multi-Weyl and nodal line semimetals. Our first aim was to reveal their optical properties, and show that the revealed properties can serve as useful information for identifying them in optical experiments. We evaluated optical conductivity using the Kubo formula in the non-interacting limit, and obtained several interesting features, as summarized below.

For nodal line semimetals, we suggested a geometrical understanding of the optical conductivity using graphene analogy. We found that a geometrical change in the phase space for interband transitions can cause qualitatively different optical behaviors. We expect our results to be generally applicable to arbitrary nodal line systems.

We also studied the optical properties of multi-Weyl semimetals in semimetallic and nearby insulating phases, focusing on the frequency dependence of optical

conductivity. We demonstrated that the optical conductivities $\sigma_{xx}(\omega)$, $\sigma_{zz}(\omega)$, and $\sigma_{xy}(\omega)$ exhibit a characteristic frequency dependence that strongly varies according to the winding number and phase of the system.

Our second aim was to understand interacting phenomena in Dirac materials. In particular, we investigated collective modes and their couplings with phonons. We begin our study by investigating plasmon modes of multi-Weyl semimetals. We calculated long-wavelength plasma frequencies incorporating interband transitions and chiral properties of carriers. We find that interband transitions and chirality lead to the depolarization shift of plasma frequencies. Interestingly, plasmons along both directions remain undamped over a broad range of densities due to the chirality induced depolarization shift.

Then we investigated quasiparticle scattering mechanisms in graphene systems in the presence of the coupling between electrons and surface optical phonons of the polar substrate. We calculate the self-energy within the GW approximation treating both electrons and phonons on an equal footing. We found a new decay channel through the emission of the plasmon-phonon coupled mode. It results in a sudden rise in the scattering rate, which is absent in non-coupled systems.

Bibliography

[1] C. L. Kane and E. J. Mele, "Quantum spin hall effect in graphene", Phys. Rev. Lett. **95**, 226801 (2005).

[2] G. Xu, H. Weng, Z. Wang, X. Dai, and Z. Fang, "Chern semimetal and the quantized anomalous hall effect in $HgCr_2Se_4$", Phys. Rev. Lett. **107** (2011).

[3] C. Fang, M. J. Gilbert, X. Dai, and B. A. Bernevig, "Multi-Weyl topological semimetals stabilized by point group symmetry", Phys. Rev. Lett. **108** (2012).

[4] S.-M. Huang, S.-Y. Xu, I. Belopolski, C.-C. Lee, G. Chang, T.-R. Chang, B. Wang, N. Alidoust, G. Bian, M. Neupane, D. Sanchez, H. Zheng, H.-T. Jeng, A. Bansil, T. Neupert, H. Lin, and M. Z. Hasan, "New type of Weyl semimetal with quadratic double Weyl fermions", Proc. Natl. Acad. Sci. USA **113**, 1180 (2016).

[5] A. A. Burkov, M. D. Hook, and L. Balents, "Topological nodal semimetals", Phys. Rev. B **84** (2011).

[6] C.-K. Chiu and A. P. Schnyder, "Classification of reflection-symmetry-protected topological semimetals and nodal superconductors", Phys. Rev. B **90** (2014).

[7] C. Fang, H. Weng, X. Dai, and Z. Fang, "Topological nodal line semimetals", Chin. Phys. B **25** (2016).

[8] R. Yu, Z. Fang, X. Dai, and H. Weng, "Topological nodal line semimetals predicted from first-principles calculations", Front. Phys. **12** (2017).

[9] M. Neupane, S.-Y. Xu, R. Sankar, N. Alidoust, G. Bian, C. Liu, I. Belopolski, T.-R. Chang, H.-T. Jeng, H. Lin, A. Bansil, F. Chou, and M. Z. Hasan, "Observation of a three-dimensional topological Dirac semimetal phase in high-mobility Cd_3As_2", Nat. Commun. **5** (2014).

[10] S. Jeon, B. B. Zhou, A. Gyenis, B. E. Feldman, I. Kimchi, A. C. Potter, Q. D. Gibson, R. J. Cava, A. Vishwanath, and A. Yazdani, "Landau quantization and quasiparticle interference in the three-dimensional Dirac semimetal Cd_3As_2", Nat. Mater. **13**, 851 (2014).

[11] Z. K. Liu, J. Jiang, B. Zhou, Z. J. Wang, Y. Zhang, H. M. Weng, D. Prabhakaran, S. K. Mo, H. Peng, P. Dudin, T. Kim, M. Hoesch, Z. Fang, X. Dai, Z. X. Shen, D. L. Feng, Z. Hussain, and Y. L. Chen, "A stable three-dimensional topological dirac semimetal Cd_3As_2", Nat. Mater. **13**, 677 (2014).

[12] Z. K. Liu, B. Zhou, Y. Zhang, Z. J. Wang, H. M. Weng, D. Prabhakaran, S. K. Mo, Z. X. Shen, Z. Fang, X. Dai, Z. Hussain, and Y. L. Chen, "Discovery of a three-dimensional topological Dirac semimetal, Na_3Bi", Science **343**, 864 (2014).

[13] S. Borisenko, Q. Gibson, D. Evtushinsky, V. Zabolotnyy, B. Buechner, and R. J. Cava, "Experimental realization of a three-dimensional Dirac semimetal", Phys. Rev. Lett. **113** (2014).

[14] L. P. He, X. C. Hong, J. K. Dong, J. Pan, Z. Zhang, J. Zhang, and S. Y. Li, "Quantum transport evidence for the three-dimensional dirac semimetal phase in Cd_3As_2", Phys. Rev. Lett. **113** (2014).

[15] C.-Z. Li, L.-X. Wang, H. Liu, J. Wang, Z.-M. Liao, and D.-P. Yu, "Giant negative magnetoresistance induced by the chiral anomaly in individual Cd_3As_2 nanowires", Nat. Commun. **6** (2015).

[16] C.-Z. Chen, J. Song, H. Jiang, Q.-f. Sun, Z. Wang, and X. C. Xie, "Disorder and metal-insulator transitions in Weyl semimetals", Phys. Rev. Lett. **115** (2015).

[17] Q. Li, D. E. Kharzeev, C. Zhang, Y. Huang, I. Pletikosic, A. V. Fedorov, R. D. Zhong, J. A. Schneeloch, G. D. Gu, and T. Valla, "Chiral magnetic effect in $ZrTe_5$", Nat. Phys. **12**, 550 (2016).

[18] S.-Y. Xu, N. Alidoust, I. Belopolski, Z. Yuan, G. Bian, T.-R. Chang, H. Zheng, V. N. Strocov, D. S. Sanchez, G. Chang, C. Zhang, D. Mou, Y. Wu, L. Huang, C.-C. Lee, S.-M. Huang, B. Wang, A. Bansil, H.-T. Jeng, T. Neupert, A. Kaminski, H. Lin, S. Jia, and M. Z. Hasan, "Discovery of a weyl fermion state with fermi arcs in niobium arsenide", Nat. Phys. **11**, 748 (2015).

[19] B. Q. Lv, S. Muff, T. Qian, Z. D. Song, S. M. Nie, N. Xu, P. Richard, C. E. Matt, N. C. Plumb, L. X. Zhao, G. F. Chen, Z. Fang, X. Dai, J. H. Dil, J. Mesot, M. Shi, H. M. Weng, and H. Ding, "Observation of fermi-arc spin texture in taas", Phys. Rev. Lett. **115** (2015).

[20] B. Q. Lv, H. M. Weng, B. B. Fu, X. P. Wang, H. Miao, J. Ma, P. Richard, X. C. Huang, L. X. Zhao, G. F. Chen, Z. Fang, X. Dai, T. Qian, and H. Ding, "Experimental discovery of weyl semimetal TaAs", Phys. Rev. X **5** (2015).

[21] B. Q. Lv, N. Xu, H. M. Weng, J. Z. Ma, P. Richard, X. C. Huang, L. X. Zhao, G. F. Chen, C. E. Matt, F. Bisti, V. N. Strocov, J. Mesot, Z. Fang, X. Dai, T. Qian, M. Shi, and H. Ding, "Observation of Weyl nodes in TaAs", Nat. Phys. **11**, 724 (2015).

[22] S.-M. Huang, S.-Y. Xu, I. Belopolski, C.-C. Lee, G. Chang, B. Wang, N. Alidoust, G. Bian, M. Neupane, C. Zhang, S. Jia, A. Bansil, H. Lin, and M. Z. Hasan, "A weyl fermion semimetal with surface fermi arcs in the transition metal monopnictide taas class", Nat. Commun. **6** (2015).

[23] S.-Y. Xu, I. Belopolski, D. S. Sanchez, C. Zhang, G. Chang, C. Guo, G. Bian, Z. Yuan, H. Lu, T.-R. Chang, P. P. Shibayev, M. L. Prokopovych, N. Alidoust, H. Zheng, C.-C. Lee, S.-M. Huang, R. Sankar, F. Chou, C.-H. Hsu, H.-T. Jeng, A. Bansil, T. Neupert, V. N. Strocov, H. Lin, S. Jia, and M. Z. Hasan, "Experimental discovery of a topological weyl semimetal state in TaP", Sci. Adv. **1** (2015).

[24] L. X. Yang, Z. K. Liu, Y. Sun, H. Peng, H. F. Yang, T. Zhang, B. Zhou, Y. Zhang, Y. F. Guo, M. Rahn, D. Prabhakaran, Z. Hussain, S. K. Mo, C. Felser, B. Yan, and Y. L. Chen, "Weyl semimetal phase in the non-centrosymmetric compound TaAs", Nat. Phys. **11**, 728 (2015).

[25] H. Inoue, A. Gyenis, Z. Wang, J. Li, S. W. Oh, S. Jiang, N. Ni, B. A. Bernevig, and A. Yazdani, "Quasiparticle interference of the fermi arcs and surface-bulk connectivity of a Weyl semimetal", Science **351**, 1184 (2016).

[26] B. Xu, Y. M. Dai, L. X. Zhao, K. Wang, R. Yang, W. Zhang, J. Y. Liu, H. Xiao, G. F. Chen, A. J. Taylor, D. A. Yarotski, R. P. Prasankumar, and X. G. Qiu, "Optical spectroscopy of the Weyl semimetal TaAs", Phys. Rev. B **93** (2016).

[27] P. J. W. Moll, N. L. Nair, T. Helm, A. C. Potter, I. Kimchi, A. Vishwanath, and J. G. Analytis, "Transport evidence for fermi-arc-mediated chirality transfer in the Dirac semimetal Cd_3As_2", Nature (London) **535**, 266 (2016).

[28] S. Banerjee and W. E. Pickett, "Phenomenology of a semi-Dirac semi-Weyl semimetal", Phys. Rev. B **86** (2012).

[29] H.-H. Lai, "Correlation effects in double-Weyl semimetals", Phys. Rev. B **91** (2015).

[30] S.-K. Jian and H. Yao, "Correlated double-weyl semimetals with coulomb interactions: possible applications to $HgCr_2Se_4$ and $SrSi_2$", Phys. Rev. B **92** (2015).

[31] T. Guan, C. Lin, C. Yang, Y. Shi, C. Ren, Y. Li, H. Weng, X. Dai, and Z. Fang, "Evidence for half-metallicity in n-type $HgCr_2Se_4$", Phys. Rev. Lett. **115** (2015).

[32] H. Huang, Z. Liu, H. Zhang, W. Duan, and D. Vanderbilt, "Emergence of a chern-insulating state from a semi-Dirac dispersion", Phys. Rev. B **92** (2015).

[33] P. K. Pyatkovskiy and T. Chakraborty, "Dynamical polarization and plasmons in a two-dimensional system with merging dirac points", Phys. Rev. B **93** (2016).

[34] R. Y. Chen, S. J. Zhang, J. A. Schneeloch, C. Zhang, Q. Li, G. D. Gu, and N. L. Wang, "Optical spectroscopy study of the three-dimensional Dirac semimetal $ZrTe_5$", Phys. Rev. B **92** (2015).

[35] S. Das Sarma and E. H. Hwang, "Charge transport in gapless electron-hole systems with arbitrary band dispersion", Phys. Rev. B **91** (2015).

[36] S. Das Sarma, E. H. Hwang, and H. Min, "Carrier screening, transport, and relaxation in three-dimensional Dirac semimetals", Phys. Rev. B **91** (2015).

[37] L. P. Eisenhart, *A treatise on the differential geometry of curves and surfaces* (Ginn, 1909).

[38] J. P. Carbotte, "Optical response of a line node semimetal", J. Phys. Condens. Matter **29** (2017).

[39] K. Mullen, B. Uchoa, and D. T. Glatzhofer, "Line of Dirac nodes in hyper-honeycomb lattices", Phys. Rev. Lett. **115** (2015).

[40] C. Fang, Y. Chen, H.-Y. Kee, and L. Fu, "Topological nodal line semimetals with and without spin-orbital coupling", Phys. Rev. B **92** (2015).

[41] T. Ando, Y. S. Zheng, and H. Suzuura, "Dynamical conductivity and zero-mode anomaly in honeycomb lattices", J. Phys. Soc. Jpn. **71**, 1318 (2002).

[42] G. D. Mahan, *Many-particle physics* (Springer Science & Business Media, 2013).

[43] P. Delplace, J. Li, and D. Carpentier, "Topological weyl semi-metal from a lattice model", Europhys. Lett. **97** (2012).

[44] A. M. Turner and A. Vishwanath, *Topological insulators: chapter 11. beyond band insulators: topology of semimetals and interacting phases*, Vol. 6 (Elsevier Inc. Chapters, 2013).

[45] G. B. Arfken and H. J. Weber, *Mathematical methods for physicists* (Academic press, 2005).

[46] C. J. Tabert, J. P. Carbotte, and E. J. Nicol, "Optical and transport properties in three-dimensional Dirac and Weyl semimetals", Phys. Rev. B **93** (2016).

[47] D. Olego, A. Pinczuk, A. C. Gossard, and W. Wiegmann, "Plasma dispersion in a layered electron-gas - a determination in gaas (alga) as heterostructures", Phys. Rev. B **25**, 7867 (1982).

[48] A. Pinczuk, M. G. Lamont, and A. C. Gossard, "Discrete plasmons in finite semiconductor multilayers", Phys. Rev. Lett. **56**, 2092 (1986).

[49] M. A. Eriksson, A. Pinczuk, B. S. Dennis, S. H. Simon, L. N. Pfeiffer, and K. W. West, "Collective excitations in the dilute 2d electron system", Phys. Rev. Lett. **82**, 2163 (1999).

[50] T. Langer, J. Baringhaus, H. Pfnuer, H. W. Schumacher, and C. Tegenkamp, "Plasmon damping below the landau regime: the role of defects in epitaxial graphene", New J. Phys. **12** (2010).

[51] Y. Liu, R. F. Willis, K. V. Emtsev, and T. Seyller, "Plasmon dispersion and damping in electrically isolated two-dimensional charge sheets", Phys. Rev. B **78** (2008).

[52] S. Y. Shin, N. D. Kim, J. G. Kim, K. S. Kim, D. Y. Noh, K. S. Kim, and J. W. Chung, "Control of the pi plasmon in a single layer graphene by charge doping", Appl. Phys. Lett. **99** (2011).

[53] T. Eberlein, U. Bangert, R. R. Nair, R. Jones, M. Gass, A. L. Bleloch, K. S. Novoselov, A. Geim, and P. R. Briddon, "Plasmon spectroscopy of free-standing graphene films", Phys. Rev. B **77** (2008).

[54] A. Nagashima, K. Nuka, H. Itoh, T. Ichinokawa, C. Oshima, S. Otani, and Y. Ishizawa, "2-dimensional plasmons in monolayer graphite", Solid State Commun. **83**, 581 (1992).

[55] T. Ando, A. B. Fowler, and F. Stern, "Electronic-properties of two-dimensional systems", Rev. Mod. Phys. **54**, 437 (1982).

[56] E. H. Hwang and S. Das Sarma, "Dielectric function, screening, and plasmons in two-dimensional graphene", Phys. Rev. B **75** (2007).

[57] J. Zhou, H.-R. Chang, and D. Xiao, "Plasmon mode as a detection of the chiral anomaly in Weyl semimetals", Phys. Rev. B **91** (2015).

[58] J. Hofmann and S. Das Sarma, "Plasmon signature in Dirac-Weyl liquids", Phys. Rev. B **91** (2015).

[59] R. E. Throckmorton, J. Hofmann, E. Barnes, and S. Das Sarma, "Many-body effects and ultraviolet renormalization in three-dimensional Dirac materials", Phys. Rev. B **92** (2015).

[60] J. D. Jackson, *Electrodynamics* (Wiley Online Library, 1975).

[61] S. Das Sarma and E. H. Hwang, "Collective modes of the massless dirac plasma", Phys. Rev. Lett. **102**, 206412 (2009).

[62] S. Das Sarma, S. Adam, E. H. Hwang, and E. Rossi, "Electronic transport in two-dimensional graphene", Rev. Mod. Phys. **83**, 407 (2011).

[63] A. H. Castro Neto, F. Guinea, N. M. R. Peres, K. S. Novoselov, and A. K. Geim, "The electronic properties of graphene", Rev. Mod. Phys. **81**, 109 (2009).

[64] Y. Wu, Y.-m. Lin, A. A. Bol, K. A. Jenkins, F. Xia, D. B. Farmer, Y. Zhu, and P. Avouris, "High-frequency, scaled graphene transistors on diamond-like carbon", Nature (London) **472**, 74 (2011).

[65] J.-H. Chen, C. Jang, S. Xiao, M. Ishigami, and M. S. Fuhrer, "Intrinsic and extrinsic performance limits of graphene devices on SiO_2", Nat. Nanotech. **3**, 206 (2008).

[66] V. E. Dorgan, M.-H. Bae, and E. Pop, "Mobility and saturation velocity in graphene on SiO_2", Appl. Phys. Lett. **97** (2010).

[67] Z. Fei, G. O. Andreev, W. Bao, L. M. Zhang, A. S. McLeod, C. Wang, M. K. Stewart, Z. Zhao, G. Dominguez, M. Thiemens, M. M. Fogler, M. J. Tauber, A. H. Castro-Neto, C. N. Lau, F. Keilmann, and D. N. Basov, "Infrared nanoscopy of Dirac plasmons at the graphene-SiO_2 interface", Nano Lett. **11**, 4701 (2011).

[68] J. A. Robinson, M. Wetherington, J. L. Tedesco, P. M. Campbell, X. Weng, J. Stitt, M. A. Fanton, E. Frantz, D. Snyder, B. L. VanMil, G. G. Jernigan, R. L. Myers-Ward, J. Eddy Charles R., and D. K. Gaskill, "Correlating raman spectral signatures with carrier mobility in epitaxial graphene: a guide to achieving high mobility on the wafer scale", Nano Lett. **9**, 2873 (2009).

[69] P. Sutter, "Epitaxial graphene how silicon leaves the scene", Nat. Mater. **8**, 171 (2009).

[70] Y. Liu and R. F. Willis, "Plasmon-phonon strongly coupled mode in epitaxial graphene", Phys. Rev. B **81** (2010).

[71] R. J. Koch, T. Seyller, and J. A. Schaefer, "Strong phonon-plasmon coupled modes in the graphene/silicon carbide heterosystem", Phys. Rev. B **82** (2010).

[72] C. R. Dean, A. F. Young, I. Meric, C. Lee, L. Wang, S. Sorgenfrei, K. Watanabe, T. Taniguchi, P. Kim, K. L. Shepard, and J. Hone, "Boron nitride substrates for high-quality graphene electronics", Nat. Nanotech. **5**, 722 (2010).

[73] L. Wang, I. Meric, P. Y. Huang, Q. Gao, Y. Gao, H. Tran, T. Taniguchi, K. Watanabe, L. M. Campos, D. A. Muller, J. Guo, P. Kim, J. Hone, K. L. Shepard, and C. R. Dean, "One-dimensional electrical contact to a two-dimensional material", Science **342**, 614 (2013).

[74] S. Ulstrup, M. Bianchi, R. Hatch, D. Guan, A. Baraldi, D. Alfe, L. Hornekaer, and P. Hofmann, "High-temperature behavior of supported graphene: electron-phonon coupling and substrate-induced doping", Phys. Rev. B **86** (2012).

[75] A. Principi, M. Carrega, M. B. Lundeberg, A. Woessner, F. H. L. Koppens, G. Vignale, and M. Polini, "Plasmon losses due to electron-phonon scattering: the case of graphene encapsulated in hexagonal boron nitride", Phys. Rev. B **90** (2014).

[76] K. Zou, X. Hong, D. Keefer, and J. Zhu, "Deposition of high-quality HfO_2 on graphene and the effect of remote oxide phonon scattering", Phys. Rev. Lett. **105** (2010).

[77] E. H. Hwang and S. Das Sarma, "Acoustic phonon scattering limited carrier mobility in two-dimensional extrinsic graphene", Phys. Rev. B **77** (2008).

[78] C.-H. Park, N. Bonini, T. Sohier, G. Samsonidze, B. Kozinsky, M. Calandra, F. Mauri, and N. Marzari, "Electron-phonon interactions and the intrinsic electrical resistivity of graphene", Nano Lett. **14**, 1113 (2014).

[79] T. Sohier, M. Calandra, C.-H. Park, N. Bonini, N. Marzari, and F. Mauri, "Phonon-limited resistivity of graphene by first-principles calculations: Electron-phonon interactions, strain-induced gauge field, and Boltzmann equation", Phys. Rev. B **90** (2014).

[80] S. H. Zhang, W. Xu, F. M. Peeters, and S. M. Badalyan, "Electron energy and temperature relaxation in graphene on a piezoelectric substrate", Phys. Rev. B **89** (2014).

[81] H. Min, E. H. Hwang, and S. Das Sarma, "Chirality-dependent phonon-limited resistivity in multiple layers of graphene", Phys. Rev. B **83** (2011).

[82] D. K. Efetov and P. Kim, "Controlling electron-phonon interactions in graphene at ultrahigh carrier densities", Phys. Rev. Lett. **105** (2010).

[83] A. Pachoud, M. Jaiswal, P. K. Ang, K. P. Loh, and B. Oezyilmaz, "Graphene transport at high carrier densities using a polymer electrolyte gate", Europhys. Lett. **92** (2010).

[84] J. M. Dawlaty, S. Shivaraman, M. Chandrashekhar, F. Rana, and M. G. Spencer, "Measurement of ultrafast carrier dynamics in epitaxial graphene", Appl. Phys. Lett. **92** (2008).

[85] H. Yan, T. Low, W. Zhu, Y. Wu, M. Freitag, X. Li, F. Guinea, P. Avouris, and F. Xia, "Damping pathways of mid-infrared plasmons in graphene nanostructures", Nat. Phot. **7**, 394 (2013).

[86] B. A. Mason and S. Dassarma, "Quasiparticle spectrum of a frohlich polaron in 2 dimensions", Phys. Rev. B **31**, 5223 (1985).

[87] W.-K. Tse and S. Das Sarma, "Phonon-induced many-body renormalization of the electronic properties of graphene", Phys. Rev. Lett. **99** (2007).

[88] J. P. F. LeBlanc, J. P. Carbotte, and E. J. Nicol, "Effect of electron-phonon coupling on energy and density of states renormalizations of dynamically screened graphene", Phys. Rev. B **84** (2011).

[89] J. P. Carbotte, J. P. F. LeBlanc, and P. E. C. Ashby, "Impact of electron-phonon coupling on near-field optical spectra in graphene", Phys. Rev. B **87** (2013).

[90] X. Zhu, W. Wang, W. Yan, M. B. Larsen, P. Boggild, T. G. Pedersen, S. Xiao, J. Zi, and N. A. Mortensen, "Plasmon-phonon coupling in large-area graphene dot and antidot arrays fabricated by nanosphere lithography", Nano Lett. **14**, 2907 (2014).

[91] V. W. Brar, M. S. Jang, M. Sherrott, S. Kim, J. J. Lopez, L. B. Kim, M. Choi, and H. Atwater, "Hybrid surface-phonon-plasmon polariton modes in graphene/monolayer h-bn heterostructures", Nano Lett. **14**, 3876 (2014).

[92] E. H. Hwang, R. Sensarma, and S. Das Sarma, "Plasmon-phonon coupling in graphene", Phys. Rev. B **82** (2010).

[93] M. Jablan, M. Soljacic, and H. Buljan, "Unconventional plasmon-phonon coupling in graphene", Phys. Rev. B **83** (2011).

[94] Z.-Y. Ong and M. V. Fischetti, "Theory of interfacial plasmon-phonon scattering in supported graphene", Phys. Rev. B **86** (2012).

[95] B. Scharf, V. Perebeinos, J. Fabian, and I. Zutic, "Magneto-optical conductivity of graphene on polar substrates", Phys. Rev. B **88** (2013).

[96] S. Fratini and F. Guinea, "Substrate-limited electron dynamics in graphene", Phys. Rev. B **77** (2008).

[97] J. Schiefele, F. Sols, and F. Guinea, "Temperature dependence of the conductivity of graphene on boron nitride", Phys. Rev. B **85** (2012).

[98] X. Li, E. A. Barry, J. M. Zavada, M. B. Nardelli, and K. W. Kim, "Surface polar phonon dominated electron transport in graphene", Appl. Phys. Lett. **97** (2010).

[99] R. Jalabert and S. Dassarma, "Quasiparticle properties of a coupled two-dimensional electron-phonon system", Phys. Rev. B **40**, 9723 (1989).

[100] E. H. Hwang and S. Dassarma, "Plasmon-phonon coupling in one-dimensional semiconductor quantum-wire structures", Phys. Rev. B **52**, R8668 (1995).

[101] E. McCann, "Asymmetry gap in the electronic band structure of bilayer graphene", Phys. Rev. B **74** (2006).

[102] E. McCann, D. S. L. Abergel, and V. I. Fal'ko, "Electrons in bilayer graphene", Solid State Commun. **143**, 110 (2007).

[103] E. H. Hwang, B. Y.-K. Hu, and S. Das Sarma, "Inelastic carrier lifetime in graphene", Phys. Rev. B **76** (2007).

[104] H. Nienhaus, T. U. Kampen, and W. Monch, "PHONONS IN 3C-SIC, 4H-SIC, AND 6H-SIC", Surf. Sci. **324**, L328 (1995).

[105] R. Sensarma, E. H. Hwang, and S. Das Sarma, "Dynamic screening and low-energy collective modes in bilayer graphene", Phys. Rev. B **82** (2010).

[106] O. V. Gamayun, "Dynamical screening in bilayer graphene", Phys. Rev. B **84** (2011).

[107] G. Borghi, M. Polini, R. Asgari, and A. H. MacDonald, "Dynamical response functions and collective modes of bilayer graphene", Phys. Rev. B **80** (2009).

[108] A. Palevski, M. Heiblum, C. P. Umbach, C. M. Knoedler, A. N. Broers, and R. H. Koch, "Lateral tunneling, ballistic transport, and spectroscopy in a two-dimensional electron-gas", Phys. Rev. Lett. **62**, 1776 (1989).

[109] T. Sakamoto, H. Kawaura, T. Baba, and T. Iizuka, "Characteristic length of hot-electron transport in silicon metal-oxide-semiconductor field-effect transistors", Appl. Phys. Lett. **76**, 2618 (2000).

[110] W.-K. Tse, E. H. Hwang, and S. D. Sarma, "Ballistic hot electron transport in graphene", Appl. Phys. Lett. **93** (2008).

[111] M. Koshino and I. F. Hizbullah, "Magnetic susceptibility in three-dimensional nodal semimetals", Phys. Rev. B **93** (2016).

[112] A. A. Soluyanov, D. Gresch, Z. Wang, Q. Wu, M. Troyer, X. Dai, and B. A. Bernevig, "Type-II Weyl semimetals", Nature (London) **527**, 495 (2015).

[113] J. Hofmann, E. Barnes, and S. Das Sarma, "Interacting Dirac liquid in three-dimensional semimetals", Phys. Rev. B **92** (2015).

Appendix A

Optical conductivity of nodal line semimetals

A.1 Comparison with other models

A.1.1 4-band continuum model

In this section, we compare the optical conductivities obtained from the 2-band and 4-band continuum models, and demonstrate that in the frequency range where interband transitions involving higher energy bands are negligible, they give the same results.

Consider the following 4-band continuum model [5, 111]:

$$H = \hbar v(k_x\sigma_x + k_y\sigma_y) + \hbar v k_z \tau_z \sigma_z + \varepsilon_0 \tau_x + \hbar \boldsymbol{v}_t \cdot \boldsymbol{k}\sigma_0. \tag{A.1}$$

The eigenenergies are given by

$$\varepsilon_\pm^2 = \hbar^2 v^2 \left[(k_\rho \pm k_0)^2 + k_z^2\right] + \hbar \boldsymbol{v}_t \cdot \boldsymbol{k}, \tag{A.2}$$

where $\varepsilon_0 = \hbar v k_0$. Thus, ε_- has zero energy solutions forming a nodal line with the radius of k_0. Note that the energy dispersion for the low-energy bands exactly match

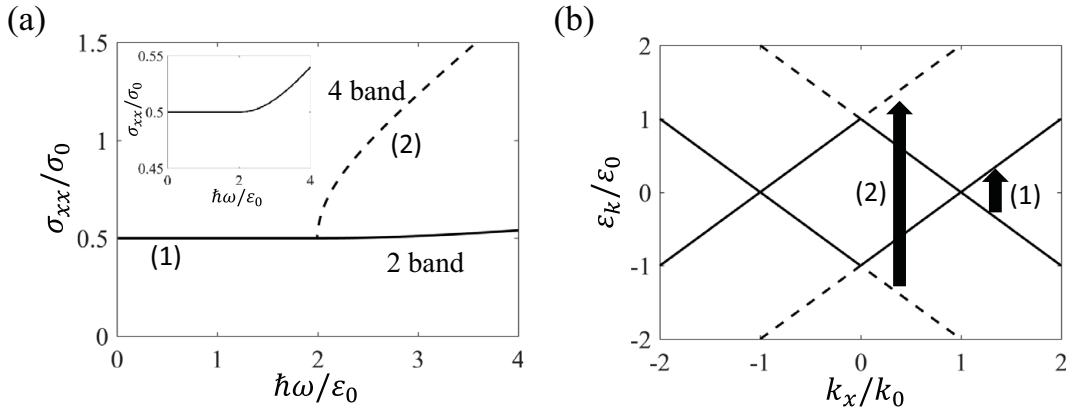

Figure A.1 (a) Optical conductivities for the 2-band (solid) and 4-band (dashed) models in the absence of tilt with zero Fermi energy. (b) Energy dispersions along the k_x axis for the 2-band (solid) and the 4-band (dashed) models. The thick arrows labeled by (1) and (2) represent interband transitions at low frequencies and high frequencies, respectively. The inset to (a) shows an enlarged view in σ_{xx} near $\hbar\omega = 2\varepsilon_0$ for the 2-band model.

with that of the 2-band model [see Fig. A.1 (b)].

Next, consider optical conductivities for the 2-band and 4-band models in the absence of tilt with zero Fermi energy, for simplicity [see Fig. A.1 (a)]. At frequencies $\hbar\omega < 2\varepsilon_0$, the results for both models are in good agreement because the two models have the same low-energy electronic structure. This is true when NLSMs are tilted; a tilt term changes the shape of the band dispersion but not the wave functions, and thus there is no mixing between low and high energy states. At $\hbar\omega > 2\varepsilon_0$, however, the 4-band result strongly deviates from the 2-band result, showing a sharp increase at $\hbar\omega = 2\varepsilon_0$ due to interband transitions between high energy bands that are not captured by the 2-band model [38]. Thus in the frequency range where interband transitions involving high energy bands are negligible, the optical conductivity of NLSMs shows the exactly same qualitative features as described in the main text,

despite the existence of the high energy bands that are not captured by the 2-band model.

A.1.2 2-band lattice model

In this section, we present the optical conductivities obtained from a 2-band lattice model, and demonstrate that at low frequencies, the result is consistent with the corresponding 2-band continuum model.

Consider the following 2-band lattice model:

$$H = t\{m_0 - 2[\cos(k_x a) + \cos(k_y a)]\}\sigma_x + t_z \cos(k_z a)\sigma_y, \tag{A.3}$$

where a is the lattice spacing, and t, t_z and m_0 are material-dependent parameters. For $0 < m_0 < 4$, the Hamiltonian in Eq. (A.3) shows two nodal lines on $k_z = \pm\frac{\pi}{2a}$ planes centered at $k_x = k_y = 0$ in the first Brillouin zone [see Fig. A.2(a)]. The nodal lines touches the k_x and k_y axes at $k_x = \pm k_0$ and $k_y = \pm k_0$, respectively, where $m_0 = 2[\cos(k_0 a) + 1]$. For simplicity, assume that $k_0 a \ll 1$. Then $m_0 \approx 4 - (k_0 a)^2$ and the low-energy continuum Hamiltonian for the nodal lines near $\boldsymbol{k} = (0, 0, \pm\frac{\pi}{2a})$ has the form

$$H = \frac{\hbar v}{k_0}\left(k_\rho^2 - k_0^2\right)\sigma_x \mp \hbar v_z k_z \sigma_y, \tag{A.4}$$

where $\frac{\hbar v}{a} = t k_0 a$, $\frac{\hbar v_z}{a} = t_z$ and $k_\rho = \sqrt{k_x^2 + k_y^2}$. Note that the band dispersion along the in-plane direction is quadratic, unlike the continuum model introduced in the main text [see Eq. (1)] whose dispersion is linear along the in-plane direction. Similarly as in Sec. 3.4, we can obtain the low-frequency optical conductivities as $\sigma_{xx} = \frac{e^2 k_0}{16\hbar}\frac{v}{v_z}$ and $\sigma_{zz} = \frac{e^2 k_0}{32\hbar}\frac{v_z}{v}$ for $\omega < 2vk_0$. This means that the Hamiltonian in Eq. (28) has the same qualitative features with constant optical conductivities at low frequencies as that in Eq. (3.6).

Figure A.2(b) shows the calculated optical conductivities σ_{xx} for the 2-band lattice and continuum models. At low frequencies, the two results are in good agree-

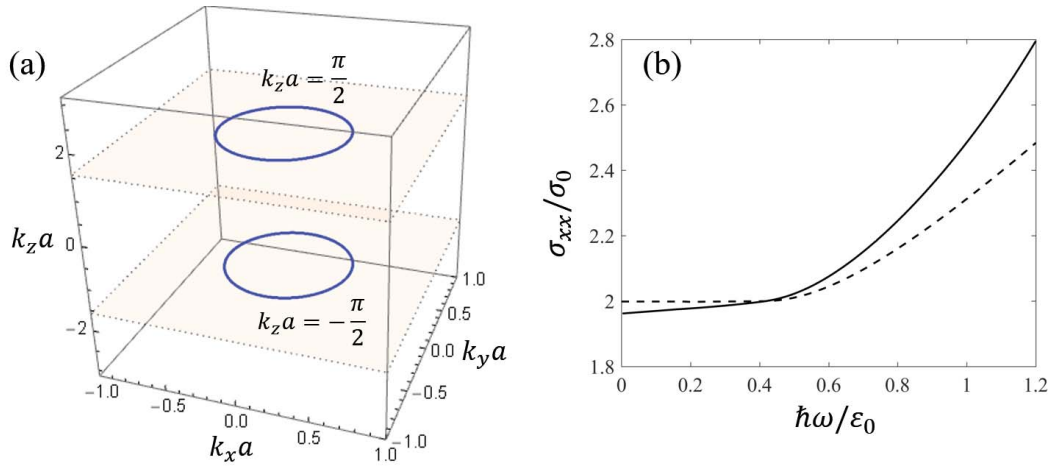

Figure A.2 (a) Nodal lines in the first Brillouin zone for $m_0 = 3.8$. (b) Optical conductivities σ_{xx} for the 2-band lattice (solid) and continuum (dashed) models in the absence of tilt with zero Fermi energy and $m_0 = 3.8$. Here $\sigma_0 = \frac{e^2 k_0}{16\hbar}\frac{v}{v_z}$ and $t = t_z = \hbar v/a$ was used for the calculation. Note that two nodal lines contribute to the optical conductivity and thus σ_{xx} approaches $2\sigma_0$ as $\omega \to 0$.

ment. As the frequency increases, however, the optical conductivity of the lattice model begins to deviate from that of the continuum model because of contributions from the high-energy band structure that cannot be captured by the low-energy continuum model.

A.2 Optical conductivity with different forms of tilt

A.2.1 Out-of-plane tilt

In this section, we consider the effect of the out-of-plane tilt, which is neglected for simplicity in the main text. Here we set the tilt velocity to be $\boldsymbol{v}_t = v_{t,x}\hat{x} + v_{t,z}\hat{z}$. The corresponding Hamiltonian describing the tilt can be written as $H_t = (\Delta_{t,x}\tilde{k}_x + \Delta_{t,z}\tilde{k}_z)\sigma_0$, where $\Delta_{t,i} = \hbar v_{t,i} k_0$ and $\tilde{k}_i = k_i/k_0$. Figures A.3 (a) and (b) show the optical conductivity σ_{xx} with a fixed in-plane tilt energy $\Delta_{t,x} = 0.3\varepsilon_0$ and various

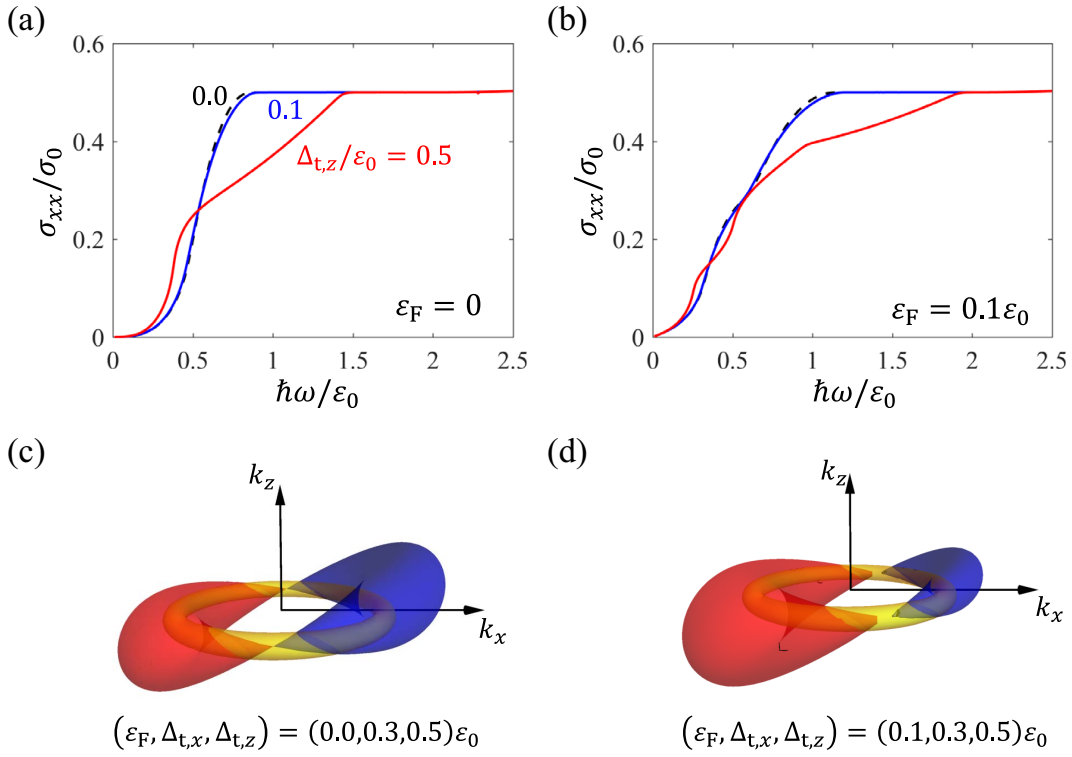

Figure A.3 (a), (b) Optical conductivities with (a) $\varepsilon_F = 0$ and (b) $\varepsilon_F = 0.1\varepsilon_0$ in the presence of both the in-plane ($\Delta_{t,x}$) and out-of-plane ($\Delta_{t,z}$) tilts. (c), (d) Electron and hole pockets exhibiting distorted Dupin cyclide due to the out-of-plane tilt. Note that the out-of-plane tilt just makes the FS asymmetric along the k_z-axis, without changing any essential features such as the point contact between the electron and hole pockets, thus leading to the same qualitative low and high frequency features in the optical conductivity compared with that obtained without the out-of-plane tilt.

out-of-plane tilt energies $\Delta_{t,z}/\varepsilon_0 = 0.0, 0.1, 0.5$. It is important to notice that at low frequencies the characteristic frequency dependence is robust against the change of $\Delta_{t,z}$; σ_{xx} for $\varepsilon_F = 0$ exhibits cubic frequency dependence while for $\varepsilon_F = 0.1\varepsilon_0$, σ_{xx} shows linear behavior, which is consistent with our results in the main text

where we assume $\Delta_{t,z} = 0$. As we increase the frequency, the optical conductivity with $\Delta_{t,z} \neq 0$ begins to deviate from that with $\Delta_{t,z} = 0$ because the distortion of the FS by the out-of-plane tilt leads to a different geometry of the PS allowed for interband transitions. At high frequencies, however, the PS allowed for interband transitions fully covers the FS, leading to the same optical conductivity behavior regardless of the existence of tilt. Note that compared with the FS in the absence of the out-of-plane tilt (see Figs. 3 and 4 in the main text), the out-of-plane tilt simply distorts the electron and hole pockets making the FS asymmetric along the k_z-axis, but without changing any qualitative features such as the point contact between the electron and hole pockets, as shown in Figs. A.3(c) and (d).

A.2.2 Fluctuating in-plane tilt

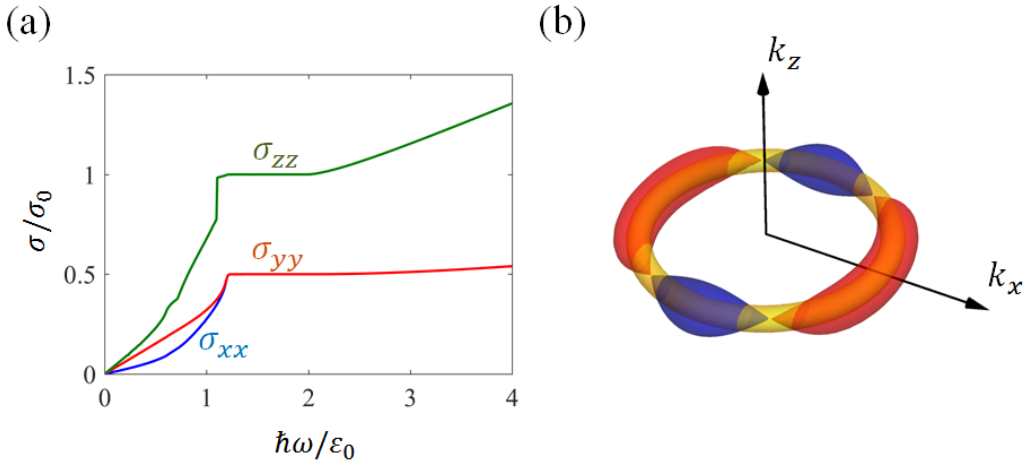

Figure A.4 (a) The optical conductivity in the presence of a fluctuating tilt and (b) the corresponding electron and hole pockets which meet at multiple points. Here we used a tilt term $H_t = \Delta_t \cos\left(\frac{3k_x}{k_0}\right)\sigma_0$ and $\Delta_t = 0.6\varepsilon_0$.

Here we consider the case where the tilt term fluctuates along the nodal line so

that the electron and hole pockets meet at multiple points, as shown in Fig. A.4 (b). In such cases, the FS does not exhibit the Dupin cyclide geometry described in the main text, yet the underlying physics is essentially the same as the case where only a linear tilt exists. Note that at low frequencies, the PS allowed for interband transitions have a similar geometry as the case where only a linear tilt exists, except for the number of the contact points [see Fig. A.4 (b)]. In the presence of multiple contact points, the total conductivity at low frequencies is obtained by summing up all the contributions from each contact point. Note that each contact point can show either linear or cubic scaling behavior at low frequencies depending on the location and the conductivity direction with respect to the tilt, as shown in the main text. If linear and cubic scaling behaviors coexist, the linear behavior becomes dominant over the cubic behavior in the zero frequency limit. In Fig. A.4 (b), the contact points are located away from the $k_x = 0$ plane, and thus optical conductivities contributed from each contact point show linear behavior at low frequencies for σ_{xx}. This leads to a linear behavior of σ_{xx} at low frequencies, as shown in Fig. A.4 (a).

Appendix B

Optical conductivity of multi-Weyl semimetals

B.1 Analytic expressions of optical conductivity for each phase

In this section, we present detailed derivations of the optical conductivities for multi-Weyl semimetals in various phases. We consider the following continuum Hamiltonian introduced in Eq. (4.3) of the main text that describes various phases such as normal insulators (NIs), Weyl semimetals (WSM) and 3D quantum anomalous Hall (QAH) states, along with the transition between them:

$$\begin{aligned} H &= \varepsilon_0 \left[\left(\frac{k_-}{k_0} \right)^J \sigma_+ + \left(\frac{k_+}{k_0} \right)^J \sigma_- \right] + M_z \sigma_z, \\ M_z &= c_1 + c_2 \left(\frac{q_z}{k_0} \right)^n + c_3 \left[\left(\frac{k_x}{k_0} \right)^2 + \left(\frac{k_y}{k_0} \right)^2 \right], \end{aligned} \tag{B.1}$$

where $\sigma_\pm = \frac{1}{2}(\sigma_x \pm i\sigma_y)$, $k_\pm = k_x \pm ik_y$, and q_z is the effective wavevector along the k_z direction. Note that for the WSM phase, $c_1 = 0$, $c_2 = \hbar v_z k_0$ and $c_3 = 0$ with $n = 1$, whereas for the insulator phases such as NI and 3D QAH, $c_1 = \alpha$, $c_2 = \beta k_0^2$

and $c_3 = \gamma k_0^2$ with $n = 2$. For the transition point, $c_1 = 0$, $c_2 = \beta k_0^2$ and $c_3 = \gamma k_0^2$ with $n = 2$.

B.1.1 Longitudinal optical conductivity

Using Eq. (3.8), we can obtain optical conductivities for multi-Weyl semimetals in the non-interacting limit. Note that for the longitudinal conductivity, $M_i^{ss'}(\boldsymbol{k})M_i^{s's}(\boldsymbol{k}) = |M_i^{ss'}(\boldsymbol{k})|^2$ $(i = x, y, z)$ is always real, thus the intraband and interband contributions of the real-part of the optical conductivity in the clean limit can be expressed as

$$\sigma_{ii}^{\text{intra}}(\omega) = -\frac{\pi e^2}{\hbar} \sum_{s=\pm} \int \frac{d^3k}{(2\pi)^3} \frac{\partial f_{s,\boldsymbol{k}}}{\partial \varepsilon_{s,\boldsymbol{k}}} |M_i^{ss}(\boldsymbol{k})|^2 \delta(\hbar\omega), \tag{B.2}$$

and

$$\sigma_{ii}^{\text{inter}}(\omega) = -\frac{\pi e^2}{\hbar} \int \frac{d^3k}{(2\pi)^3} \frac{f_{-,\boldsymbol{k}} - f_{+,\boldsymbol{k}}}{\varepsilon_{-,\boldsymbol{k}} - \varepsilon_{+,\boldsymbol{k}}} |M_i^{-+}(\boldsymbol{k})|^2 \delta(\hbar\omega + \varepsilon_{-,\boldsymbol{k}} - \varepsilon_{+,\boldsymbol{k}}), \tag{B.3}$$

at positive frequencies ($\omega > 0$).

Using this formula, it is straightforward to obtain the longitudinal optical conductivity for multi-Weyl semimetals. Because of the anisotropic energy dispersion, however, it is not trivial to obtain analytic expressions for the optical conductivity. In this section, we set $c_3 = 0$ (or $\gamma = 0$) for simplicity. This approximation works well for the Weyl phase because the linear term in M_z corresponding to the linear dispersion along the k_z direction is dominant over the quadratic mass term associated with γ at low frequencies. In the insulating phases, however, the linear term is absent, and thus neglecting the quadratic γ term is valid only when the effect of the band distortion associated with nonzero γ is small ($m_0 \ll t_x, t_y$). [See Sec. B.2(a) for the effect of γ on the optical conductivity.] To avoid difficulties associated with

anisotropic dispersions, we consider the following coordinate transformation

$$\begin{aligned} k_x &\to k_0 \left(\frac{\rho}{\varepsilon_0}\right)^{\frac{1}{J}} \cos\phi, \\ k_y &\to k_0 \left(\frac{\rho}{\varepsilon_0}\right)^{\frac{1}{J}} \sin\phi, \\ q_z &\to k_0 \left(\frac{z}{c_2}\right)^{\frac{1}{n}}, \end{aligned} \tag{B.4}$$

which transforms the Hamiltonian into the following linear form:

$$H = \rho(e^{-iJ\phi}\sigma_+ + e^{iJ\phi}\sigma_-) + (c_1 + z)\sigma_z. \tag{B.5}$$

Note that the transformed coordinates do not cover the lower hemisphere part (i.e., $q_z < 0$) when n is an even number. We can avoid this problem by taking advantage of the inversion symmetry of the system [$H(q_z) = H(-q_z)$ for even n], allowing us to get the right result by integrating over only the positive part of q_z. In the transformed coordinates, the energy dispersion is given by $E_\pm(\rho, z) = \pm E(\rho, z)$, where $E(\rho, z) = \sqrt{\rho^2 + (c_1 + z)^2}$. The corresponding eigenstate is given by

$$|+; \rho.\phi, z\rangle = \begin{pmatrix} \cos\frac{\theta}{2} \\ \sin\frac{\theta}{2} e^{iJ\phi} \end{pmatrix}, \tag{B.6a}$$

$$|-; \rho.\phi, z\rangle = \begin{pmatrix} -\sin\frac{\theta}{2} \\ \cos\frac{\theta}{2} e^{iJ\phi} \end{pmatrix}, \tag{B.6b}$$

where $\theta = \tan^{-1}\left(\frac{\rho}{c_1+z}\right)$. Note that $\cos\theta = \frac{c_1+z}{E(\rho,z)}$ and $\sin\theta = \frac{\rho}{E(\rho,z)}$.

The Jacobian $\mathcal{J}$ corresponding to this transformation is given by

$$\mathcal{J} = \begin{vmatrix} \frac{\partial k_x}{\partial\rho} & \frac{\partial k_x}{\partial\phi} & \frac{\partial k_x}{\partial z} \\ \frac{\partial k_y}{\partial\rho} & \frac{\partial k_y}{\partial\phi} & \frac{\partial k_y}{\partial z} \\ \frac{\partial q_z}{\partial\rho} & \frac{\partial q_z}{\partial\phi} & \frac{\partial q_z}{\partial z} \end{vmatrix} = \frac{k_0^3 \left(\frac{\rho}{\varepsilon_0}\right)^{\frac{2}{J}} \left(\frac{z}{c_2}\right)^{\frac{1}{n}}}{Jn\rho z} \equiv \mathcal{J}(\rho, z). \tag{B.7}$$

The velocity matrices $\hat{v}_i = \frac{1}{\hbar}\frac{\partial \hat{H}}{\partial k_i}$ can be expressed as

$$\hat{v}_x = \frac{J\varepsilon_0}{\hbar k_0}\left(\frac{\rho}{\varepsilon_0}\right)^{\frac{J-1}{J}} \begin{pmatrix} 0 & e^{-i(J-1)\phi} \\ e^{i(J-1)\phi} & 0 \end{pmatrix}, \tag{B.8a}$$

$$\hat{v}_y = \frac{J\varepsilon_0}{\hbar k_0}\left(\frac{\rho}{\varepsilon_0}\right)^{\frac{J-1}{J}} \begin{pmatrix} 0 & -ie^{-i(J-1)\phi} \\ ie^{i(J-1)\phi} & 0 \end{pmatrix}, \tag{B.8b}$$

$$\hat{v}_z = \frac{nc_2}{\hbar k_0}\left(\frac{z}{c_2}\right)^{\frac{n-1}{n}} \begin{pmatrix} 1 & 0 \\ 0 & -1 \end{pmatrix}. \tag{B.8c}$$

Then, the matrix elements of $M_i^{ss'}(\boldsymbol{k}) = \langle s, \boldsymbol{k}|\hbar\hat{v}_i|s', \boldsymbol{k}\rangle$ used in $\sigma_{xx}(\omega)$ and $\sigma_{zz}(\omega)$ are given by

$$M_x^{++}(\boldsymbol{k}) = \frac{J\varepsilon_0}{k_0}\left(\frac{\rho}{\varepsilon_0}\right)^{\frac{J-1}{J}} \frac{\rho\cos\phi}{E(\rho,z)}, \tag{B.9a}$$

$$M_x^{-+}(\boldsymbol{k}) = \frac{J\varepsilon_0}{k_0}\left(\frac{\rho}{\varepsilon_0}\right)^{\frac{J-1}{J}} \left[\frac{c_1+z}{E(\rho,z)}\cos\phi - i\sin\phi\right], \tag{B.9b}$$

$$M_z^{++}(\boldsymbol{k}) = \frac{nc_2}{k_0}\left(\frac{z}{c_2}\right)^{\frac{n-1}{n}} \frac{c_1+z}{E(\rho,z)}, \tag{B.9c}$$

$$M_z^{-+}(\boldsymbol{k}) = -\frac{nc_2}{k_0}\left(\frac{z}{c_2}\right)^{\frac{n-1}{n}} \frac{\rho}{E(\rho,z)}. \tag{B.9d}$$

After integrating over ρ and ϕ in Eqs. (B.2) and (B.3), we can obtain the integral expressions with respect to z for the longitudinal optical conductivity. The intraband

part at zero temperature for the chemical potential $\mu \geq 0$ is then given by

$$\begin{aligned}
\sigma_{xx}^{\text{intra}}(\omega) &= \frac{\pi e^2}{\hbar}\int_{z_1}^{z_2} C_n dz \int_0^{\infty} d\rho \int_0^{2\pi} d\phi \frac{\mathcal{J}(\rho,z)}{(2\pi)^3}|M_x^{++}(\boldsymbol{k})|^2 \delta(\hbar\omega) \\
&\quad \times\delta\left(\mu - E(\rho,z)\right) \\
&= \frac{e^2}{\hbar}\left(\frac{Jk_0\varepsilon_0^2}{8\pi n\mu}\right)\delta(\hbar\omega)\int_{z_1}^{z_2} C_n \frac{dz}{z}\left(\frac{z}{c_2}\right)^{\frac{1}{n}}\left(\frac{\rho_\mu(z)}{\varepsilon_0}\right)^2 \\
&\quad \times\Theta\left(\mu - |c_1+z|\right), \qquad \text{(B.10a)} \\
\sigma_{zz}^{\text{intra}}(\omega) &= \frac{\pi e^2}{\hbar}\int_{z_1}^{z_2} C_n dz \int_0^{\infty} d\rho \int_0^{2\pi} d\phi \frac{\mathcal{J}(\rho,z)}{(2\pi)^3}|M_z^{++}(\boldsymbol{k})|^2 \\
&\quad \times\delta(\hbar\omega)\delta\left(\mu - E(\rho,z)\right) \\
&= \frac{e^2}{\hbar}\left(\frac{nk_0c_2^2}{4\pi J\mu}\right)\delta(\hbar\omega)\int_{z_1}^{z_2} C_n \frac{dz}{z}\left(\frac{z}{c_2}\right)^{\frac{2n-1}{n}}\left(\frac{c_1+z}{\varepsilon_0}\right)^2 \\
&\quad \times\left(\frac{\rho_\mu(z)}{\varepsilon_0}\right)^{\frac{2(1-J)}{J}}\Theta\left(\mu - |c_1+z|\right), \qquad \text{(B.10b)}
\end{aligned}$$

where $\rho_\mu(z) = \sqrt{\mu^2 - (c_1+z)^2}$ and $\Theta(x)$ is the step function with $\Theta(x) = 1$ for $x > 0$ and 0 otherwise. The integration range is (z_1, z_2)=$(-\infty, \infty)$ for odd n, (z_1, z_2)=$(0, \infty)$ for even n and $c_2 > 0$, and (z_1, z_2)=$(-\infty, 0)$ for even n and $c_2 < 0$, and $C_n = 2$ for even n and $C_n = 1$ for odd n. Here for the ρ integration with a delta function, we use the relation $\delta(f(\rho)) = \frac{1}{|f'(\rho_0)|}\delta(\rho - \rho_0)$, where $f(\rho_0) = 0$.

For the interband part of optical conductivity, we set $\mu = 0$ for simplicity. Note that non-zero μ at zero temperature only gives rise to the Pauli blocking effect, thus the effect of non-zero μ can be taken into account by introducing the step function $\Theta(\hbar\omega - 2|\mu|)$ into the $\mu = 0$ result. [See Sec. B.2(c) for further discussion on the

effect of finite μ.] The interband part at zero temperature with $\mu = 0$ is given by

$$\begin{aligned}
\sigma_{xx}^{\text{inter}}(\omega) &= \frac{\pi e^2}{\hbar}\int_{z_1}^{z_2} C_n dz \int_0^{\infty} d\rho \int_0^{2\pi} d\phi \frac{\mathcal{J}(\rho,z)}{(2\pi)^3}\frac{|M_x^{-+}(\boldsymbol{k})|^2}{2E(\rho,z)} \\
&\quad \times\delta\left(\hbar\omega - 2E(\rho,z)\right) \\
&= \frac{e^2}{\hbar}\left(\frac{Jk_0}{32\pi n}\right)\int_{z_1}^{z_2} C_n \frac{dz}{z}\left(\frac{z}{c_2}\right)^{\frac{1}{n}}\left[\frac{(c_1+z)^2}{(\hbar\omega/2)^2}+1\right] \\
&\quad \times\Theta\left(\frac{\hbar\omega}{2} - |c_1+z|\right), \qquad \text{(B.11a)} \\
\sigma_{zz}^{\text{inter}}(\omega) &= \frac{\pi e^2}{\hbar}\int_{z_1}^{z_2} C_n dz \int_0^{\infty} d\rho \int_0^{2\pi} d\phi \frac{\mathcal{J}(\rho,z)}{(2\pi)^3}\frac{|M_z^{-+}(\boldsymbol{k})|^2}{2E(\rho,z)} \\
&\quad \times\delta\left(\hbar\omega - 2E(\rho,z)\right) \\
&= \frac{e^2}{\hbar}\left(\frac{nk_0}{4\pi J}\right)\left(\frac{c_2}{\hbar\omega}\right)^2\int_{z_1}^{z_2} C_n \frac{dz}{z}\left(\frac{z}{c_2}\right)^{\frac{2n-1}{n}}\left(\frac{\rho_\omega(z)}{\varepsilon_0}\right)^{\frac{2}{J}} \\
&\quad \times\Theta\left(\frac{\hbar\omega}{2} - |c_1+z|\right), \qquad \text{(B.11b)}
\end{aligned}$$

where $\rho_\omega(z) = \sqrt{(\hbar\omega/2)^2 - (c_1+z)^2}$. In the subsequent sections, we present calculated optical conductivity for each phase.

WSM phase

For the WSM phase, $c_1 = 0$, $c_2 = \hbar v_z k_0$, $c_3 = 0$ and $n = 1$. From Eqs. (B.10) and (B.11), the longitudinal optical conductivity is given by

$$\begin{aligned}
\sigma_{xx}(\omega) &= \frac{g_{\text{N}}}{24\pi}\frac{Je^2}{\hbar v_z}\left[\omega\Theta(\hbar\omega - 2|\mu|) + 4\omega_\mu^2\delta(\omega)\right], \qquad \text{(B.12a)} \\
\sigma_{zz}(\omega) &= \frac{g_{\text{N}}}{24\pi}\frac{e^2 v_z}{\hbar v_\parallel^2} A_{zz}^{\text{WSM}}\left(\frac{\omega}{\omega_0}\right)^{\frac{2}{J}-1}\omega_0\Theta(\hbar\omega - 2|\mu|) \\
&\quad + \frac{g_{\text{N}}}{6\pi}\frac{e^2 v_z}{\hbar v_\parallel^2} B_{zz}^{\text{WSM}}\left(\frac{|\omega_\mu|}{\omega_0}\right)^{\frac{2}{J}}\omega_0^2\delta(\omega), \qquad \text{(B.12b)}
\end{aligned}$$

where $\varepsilon_0 = \hbar\omega_0 = \hbar v_\parallel k_0$, $\omega_\mu \equiv \mu/\hbar$, $A_{zz}^{\text{WSM}} = \frac{3\sqrt{\pi}\Gamma\left(\frac{1}{J}\right)}{2^{\frac{2}{J}}J^2\Gamma\left(\frac{1}{J}+\frac{3}{2}\right)}$, and $B_{zz}^{\text{WSM}} = \frac{3\sqrt{\pi}\Gamma\left(\frac{1}{J}\right)}{4J\Gamma\left(\frac{1}{J}+\frac{3}{2}\right)}$. Here, we introduced the number of nodes g_{N}. In the derivation for σ_{zz}, we substitute $\frac{z}{\mu} = \sin\theta$ or $\frac{z}{\hbar\omega/2} = \sin\theta$, and use the relation

$\int_0^{\pi/2} d\theta \cos^m\theta \sin^n\theta = \frac{1}{2}B(\frac{m+1}{2}, \frac{n+1}{2})$ where $B(m,n) = \frac{\Gamma(m)\Gamma(n)}{\Gamma(m+n)}$ is the beta function and $\Gamma(x) = \int_0^\infty dt\, t^{x-1}e^{-t}$ is the gamma function. Note that for $J=1$, $A_{zz}^{\rm WSM}\big|_{J=1} = B_{zz}^{\rm WSM}\big|_{J=1} = 1$ and the result in Eq. (B.12) reduces to that of conventional Weyl semimetals.

The first term in Eq. (B.12) represents the interband transitions, which are forbidden at $\omega < 2|\omega_\mu|$ due to Pauli blocking, whereas the second term represents the intraband transition giving rise to the Drude peak at low frequencies. For the undoped case ($\mu = 0$), the result reduces to Eq. (4.10).

Insulator phase

For both the NI and 3D QAH phases, $c_1 = \alpha$, $c_2 = \beta k_0^2$ and $n = 2$. As discussed, we set $c_3 = 0$ (or $\gamma = 0$) for simplicity. From now on, we consider only the undoped case, $\mu = 0$. The longitudinal optical conductivity is then obtained to be

$$\sigma_{xx}(\omega) = \frac{e^2}{\hbar} G_{xx}(\omega)\,(\hbar\omega - 2|\alpha|)^{\frac{1}{2}}\,\Theta(\hbar\omega - 2|\alpha|), \tag{B.13a}$$

$$\sigma_{zz}(\omega) = \frac{e^2}{\hbar} G_{zz}(\omega)\,(\hbar\omega - 2|\alpha|)^{\frac{1}{J}+\frac{3}{2}}\,\Theta(\hbar\omega - 2|\alpha|), \tag{B.13b}$$

where

$$G_{xx}(\omega) = \frac{J\left(16|\alpha|^2 + 4|\alpha|\hbar\omega + 9(\hbar\omega)^2\right)}{120\sqrt{2}\pi|\beta|^{\frac{1}{2}}(\hbar\omega)^2}, \tag{B.14a}$$

$$G_{zz}(\omega) = \frac{k_0\Gamma\left(\frac{1}{J}\right)}{2^{\frac{2}{J}+\frac{5}{2}}\sqrt{\pi}J^2\Gamma\left(\frac{1}{J}+\frac{5}{2}\right)} \frac{(|\beta|k_0^2)^{\frac{1}{2}}(\hbar\omega + 2|\alpha|)^{\frac{1}{J}}}{\varepsilon_0^{\frac{2}{J}}(\hbar\omega)^2} \times {}_2F_1\left(-\frac{1}{J}, \frac{3}{2}; \frac{1}{J}+\frac{5}{2}; \frac{2|\alpha| - \hbar\omega}{2|\alpha| + \hbar\omega}\right), \tag{B.14b}$$

and ${}_2F_1\,(a,b;c;z) = \frac{\Gamma(c)}{\Gamma(b)\Gamma(c-b)}\int_0^1 dt \frac{t^{b-1}(1-t)^{c-b-1}}{(1-tz)^a}$ is the hypergeometric function. Note that the analytic expressions for the longitudinal conductivities with $\gamma = 0$ have the same form for both NI and 3D QAH phases except for the sign of α: $\alpha > 0$ for the NI phase and $\alpha < 0$ for the 3D QAH phase.

Transition point

For the transition point between the WSM and NI phases or between the WSM and 3D QAH phases, the analytical results can be obtained by taking the limit $\alpha \to 0$ in Eq. (B.13):

$$\sigma_{xx}(\omega) = \frac{e^2}{\hbar} A_{xx} (\hbar\omega)^{\frac{1}{2}}, \tag{B.15a}$$

$$\sigma_{zz}(\omega) = \frac{e^2}{\hbar} A_{zz} (\hbar\omega)^{\frac{2}{J}-\frac{1}{2}}, \tag{B.15b}$$

where

$$A_{xx} = \frac{3J}{40\sqrt{2}\pi|\beta|^{\frac{1}{2}}}, \tag{B.16a}$$

$$A_{zz} = \frac{k_0 \Gamma\left(\frac{1}{J}\right) (|\beta| k_0^2)^{\frac{1}{2}}}{2^{\frac{2}{J}+2} J^2 \Gamma\left(\frac{1}{4}\right) \Gamma\left(\frac{1}{J}+\frac{7}{4}\right) \varepsilon_0^{\frac{2}{J}}}. \tag{B.16b}$$

Here, we used ${}_2F_1(a,b;c;z) = {}_2F_1(b,a;c;z)$, $\Gamma(x)\Gamma(1-x) = \frac{\pi}{\sin \pi x}$ and ${}_2F_1(a,b;1+a-b;-1) = \frac{\Gamma(1+a-b)\Gamma\left(1+\frac{1}{2}a\right)}{\Gamma(1+a)\Gamma\left(1+\frac{1}{2}a-b\right)}$.

B.1.2 Transverse optical conductivity

From Eq. (3.8), the Hall or transverse optical conductivity σ_{xy} for $\mu = 0$ is given by

$$\sigma_{xy}(\omega) = -\frac{ie^2}{\hbar} \int \frac{d^3k}{(2\pi)^3} \frac{f_{+,\boldsymbol{k}} - f_{-,\boldsymbol{k}}}{\varepsilon_{+,\boldsymbol{k}} - \varepsilon_{-,\boldsymbol{k}}} \left[\frac{M_x^{+-}(\boldsymbol{k}) M_y^{-+}(\boldsymbol{k})}{\hbar\omega + \varepsilon_{+,\boldsymbol{k}} - \varepsilon_{-,\boldsymbol{k}}} + \frac{M_x^{-+}(\boldsymbol{k}) M_y^{+-}(\boldsymbol{k})}{\hbar\omega + \varepsilon_{-,\boldsymbol{k}} - \varepsilon_{+,\boldsymbol{k}}} \right]. \tag{B.17}$$

Here, in contrast to the longitudinal optical conductivity, we keep c_3 (or γ) for analytic expressions. Throughout this section, for brevity, the momentum and the energy are normalized by k_0 and ε_0, respectively, or equivalently we set $k_0 = \varepsilon_0 = 1$.

We consider the following coordinate transformation:

$$\begin{aligned} k_x &\to \rho^{\frac{1}{J}} \cos\phi, \\ k_y &\to \rho^{\frac{1}{J}} \sin\phi, \\ k_z &\to k_z, \end{aligned} \tag{B.18}$$

whose Jacobian is given by

$$\mathcal{J} = \frac{\rho^{\frac{2}{J}-1}}{J} \equiv \mathcal{J}(\rho). \tag{B.19}$$

In the transformed coordinate, the Hamiltonian becomes

$$H = \rho(e^{-iJ\phi}\sigma_+ + e^{iJ\phi}\sigma_-) + (c_1 + c_2 q_z^n + c_3\rho^{\frac{2}{J}})\sigma_z, \tag{B.20}$$

and the energy dispersion is given by $E_\pm(\rho, q_z) = \pm E(\rho, q_z)$, where

$$E(r, q_z) = \sqrt{\rho^2 + \left(c_1 + c_2 q_z^n + c_3\rho^{\frac{2}{J}}\right)^2}. \tag{B.21}$$

The corresponding eigenstate is given by

$$|+; \rho.\phi, q_z\rangle = \begin{pmatrix} \cos\frac{\theta}{2} \\ \sin\frac{\theta}{2}e^{iJ\phi} \end{pmatrix}, \tag{B.22a}$$

$$|-; \rho.\phi, q_z\rangle = \begin{pmatrix} -\sin\frac{\theta}{2} \\ \cos\frac{\theta}{2}e^{iJ\phi} \end{pmatrix}, \tag{B.22b}$$

where $\theta = \tan^{-1}\left(\frac{\rho}{m(\rho,q_z)}\right)$ and $m(\rho, q_z) = c_1 + c_2 q_z^n + c_3\rho^{\frac{2}{J}}$. Note that $\cos\theta = \frac{m(\rho,q_z)}{E(\rho,q_z)}$ and $\sin\theta = \frac{\rho}{E(\rho,q_z)}$.

The velocity matrices $\hat{v}_i = \frac{1}{\hbar}\frac{\partial\hat{H}}{\partial k_i}$ can be expressed as

$$\hat{v}_x = \frac{1}{\hbar}\begin{pmatrix} 2c_3\rho^{\frac{1}{J}}\cos\phi & J\rho^{\frac{J-1}{J}}e^{-i(J-1)\phi} \\ J\rho^{\frac{J-1}{J}}e^{i(J-1)\phi} & -2c_3\rho^{\frac{1}{J}}\cos\phi \end{pmatrix}, \tag{B.23a}$$

$$\hat{v}_y = \frac{1}{\hbar}\begin{pmatrix} 2c_3\rho^{\frac{1}{J}}\sin\phi & -iJ\rho^{\frac{J-1}{J}}e^{-i(J-1)\phi} \\ iJ\rho^{\frac{J-1}{J}}e^{i(J-1)\phi} & -2c_3\rho^{\frac{1}{J}}\sin\phi \end{pmatrix}. \tag{B.23b}$$

Then the matrix elements of $M_i^{ss'}(\boldsymbol{k}) = \langle s, \boldsymbol{k}|\hbar\hat{v}_i|s', \boldsymbol{k}\rangle$ used in $\sigma_{xy}(\omega)$ are given by

$$M_x^{+-}(\boldsymbol{k}) = J\left[\rho^{\frac{J-1}{J}}\left(\cos\theta\cos\phi + i\sin\phi\right)\right] - 2c_3\rho^{\frac{1}{J}}\sin\theta\cos\phi, \tag{B.24a}$$

$$M_y^{-+}(\boldsymbol{k}) = J\left[\rho^{\frac{J-1}{J}}\left(\cos\theta\sin\phi + i\cos\phi\right)\right] - 2c_3\rho^{\frac{1}{J}}\sin\theta\sin\phi. \tag{B.24b}$$

Note that

$$\int_0^{2\pi}\frac{d\phi}{2\pi}M_x^{+-}(\boldsymbol{k})M_y^{-+}(\boldsymbol{k})=iJ^2\rho^{\frac{2(J-1)}{J}}\left[\frac{J(c_1+c_2q_z^n)+(J-2)c_3\rho^{\frac{2}{J}}}{E(\rho,q_z)}\right]. \tag{B.25}$$

Then, from Eq. (B.17) the real part of the transverse optical conductivity is given by

$$\begin{aligned}\sigma_{xy}(\omega) &= -\frac{ie^2}{\hbar}\int_0^{\infty}d\rho\int_{-k_c}^{k_c}dk_z\int_0^{2\pi}d\phi\frac{\mathcal{J}(\rho)}{(2\pi)^3}\frac{1}{2E(\rho,q_z)}\\ &\quad\times\left[\frac{M_x^{+-}(\boldsymbol{k})M_y^{-+}(\boldsymbol{k})}{\hbar\omega+2E(\rho,q_z)}+\frac{M_x^{-+}(\boldsymbol{k})M_y^{+-}(\boldsymbol{k})}{\hbar\omega-2E(\rho,q_z)}\right]\\ &= -\frac{e^2}{\hbar}\frac{1}{8\pi^2}\int_0^{\infty}\rho d\rho\int_{-k_c}^{k_c}dk_z\left[\frac{J(c_1+c_2q_z^n)+(J-2)c_3\rho^{\frac{2}{J}}}{E(\rho,q_z)}\right]\\ &\quad\times\left[\frac{1}{E^2(\rho,q_z)-(\hbar\omega/2)^2}\right].\end{aligned} \tag{B.26}$$

Here, we introduce the momentum cutoff k_c along the k_z direction to prevent divergence of the integral. Using these results, we can obtain the real part of the transverse optical conductivity up to second order in ω as $\sigma_{xy}(\omega)\approx\sigma_{xy}^{(0)}+\sigma_{xy}^{(2)}(\omega)$, where

$$\begin{aligned}\sigma_{xy}^{(0)} &= -\frac{e^2}{\hbar}\frac{1}{8\pi^2}\int_{-k_c}^{k_c}dk_z\int_0^{\infty}\rho d\rho\,\frac{J(c_1+c_2q_z^n)+(J-2)c_3\rho^{\frac{2}{J}}}{E^3(\rho,q_z)}\\ &= \frac{e^2}{\hbar}\frac{1}{8\pi^2}\int_{-k_c}^{k_c}dk_z\,\frac{J\left(c_1+c_2q_z^n+c_3\rho^{\frac{2}{J}}\right)}{E(\rho,q_z)}\Bigg|_{\rho\to0}^{\rho\to\infty},\end{aligned} \tag{B.27a}$$

$$\begin{aligned}\sigma_{xy}^{(2)}(\omega) &= -\frac{e^2}{\hbar}\frac{(\hbar\omega)^2}{32\pi^2}\int_{-k_c}^{k_c}dk_z\int_0^{\infty}\rho d\rho\\ &\quad\times\frac{J(c_1+c_2q_z^n)+(J-2)c_3\rho^{\frac{2}{J}}}{E^5(\rho,q_z)}.\end{aligned} \tag{B.27b}$$

From now on, we recover k_0 and ε_0 for clarity.

WSM phase

For the WSM phase, $c_1 = 0$, $c_2 = \hbar v_z k_0$, $c_3 = 0$ and $n = 1$. Then the Hall conductivity for a single Weyl node is given by

$$\sigma_{xy}^{(0)} = -\frac{e^2}{\hbar}\frac{J}{8\pi^2}\int_{-k_c}^{k_c} dk_z \mathrm{sgn}(v_z q_z). \tag{B.28}$$

Note that there always appear multiple Weyl points in the Brillouin zone with the total chirality summing to zero. Here, we consider the simplest case in which two Weyl nodes with opposite chirality are located at $\pm b\hat{\boldsymbol{z}}$, respectively. Assuming that the node with positive chirality is at $k_z = +b\hat{\boldsymbol{z}}$ and the negative one is at $k_z = -b\hat{\boldsymbol{z}}$ with $|b| < k_c$, we find

$$\begin{aligned}\sigma_{xy}^{(0)} &= -\frac{e^2}{\hbar}\frac{J}{8\pi^2}\int_{-k_c}^{k_c} dk_z \left\{\mathrm{sgn}\left[v_z(k_z - b)\right] + \mathrm{sgn}\left[(-v_z)(k_z + b)\right]\right\} &\text{(B.29)}\\ &= J\frac{e^2}{h}\frac{b}{\pi}. &\text{(B.30)}\end{aligned}$$

Here, the first and second terms in the first line represent contributions from the positive and negative chirality nodes, respectively.

Similarly, we can obtain the dynamical part of the Hall conductivity. For a single Weyl node,

$$\begin{aligned}\sigma_{xy}^{(2)}(\omega) &= -\frac{e^2}{\hbar}\frac{J(\hbar\omega)^2}{32\pi^2}\int_{-k_c}^{k_c} dk_z \int_0^\infty \rho d\rho \frac{\hbar v_z q_z}{\left[\rho^2 + (\hbar v_z q_z)^2\right]^{\frac{5}{2}}}\\ &= -\frac{e^2}{\hbar}\frac{J(\hbar\omega)^2}{96\pi^2}\int_{-k_c}^{k_c} dk_z \frac{\mathrm{sgn}\left(v_z q_z\right)}{(\hbar v_z q_z)^2}. &\text{(B.31)}\end{aligned}$$

Then, the total conductivity contributed from the two Weyl nodes is given by

$$\begin{aligned}\sigma_{xy}^{(2)}(\omega) &= -\frac{e^2}{\hbar}\frac{J\omega^2}{96\pi^2 v_z^2}\int_{-k_c}^{k_c} dk_z \left\{\frac{\mathrm{sgn}\left[v_z(k_z - b)\right]}{(k_z - b)^2} + \frac{\mathrm{sgn}\left[(-v_z)(k_z + b)\right]}{(k_z + b)^2}\right\}\\ &= \frac{e^2}{\hbar}\frac{J}{24\pi^2 v_z^2}\frac{b}{k_c^2 - b^2}\omega^2. &\text{(B.32)}\end{aligned}$$

Insulator phase

For both the NI and 3D QAH phases, $c_1 = \alpha$, $c_2 = \beta k_0^2$, $c_3 = \gamma k_0^2$ and $n = 2$. The static part of the Hall conductivity after the integration over ρ is given by

$$\sigma_{xy}^{(0)} = \frac{e^2}{\hbar}\frac{1}{8\pi^2}\int_{-k_c}^{k_c} dk_z \begin{cases} 1 - \mathrm{sgn}[f(q_z)] & (J=1), \\ \frac{2\gamma k_0^2}{\sqrt{(\gamma k_0^2)^2+\varepsilon_0^2}} - 2\mathrm{sgn}[f(q_z)] & (J=2), \end{cases} \tag{B.33}$$

where $f(q_z) = \alpha + \beta q_z^2$. Now, the integral is straightforward. In the NI phase ($\alpha > 0$, $\beta > 0$), $\mathrm{sgn}[f(q_z)] = 1$, thus

$$\sigma_{xy}^{(0)} = \frac{e^2}{\hbar} \begin{cases} 0 & (J=1), \\ \frac{k_c}{2\pi^2}\left(\frac{\gamma k_0^2}{\sqrt{(\gamma k_0^2)^2+\varepsilon_0^2}} - 1\right) & (J=2), \end{cases} \tag{B.34}$$

whereas in the 3D QAH phase ($\alpha < 0$, $\beta < 0$), $\mathrm{sgn}[f(q_z)] = -1$, and so

$$\sigma_{xy}^{(0)} = \frac{e^2}{\hbar} \begin{cases} \frac{k_c}{2\pi^2} & (J=1), \\ \frac{k_c}{2\pi^2}\left(\frac{\gamma k_0^2}{\sqrt{(\gamma k_0^2)^2+\varepsilon_0^2}} + 1\right) & (J=2). \end{cases} \tag{B.35}$$

The results in Eq. (B.34) show that the static Hall conductivity $\sigma_{xy}^{(0)}$ in the NI phase is nonzero for $J = 2$ in contrast to the corresponding lattice result, and that $\sigma_{xy}^{(0)}$ for the $J = 2$ 3D QAH phase in Eq. (B.35) contains material dependent parameters such as γ and ε_0. This is puzzling because the static Hall conductivity characterizing the topological state of the system should have a quantized value. The reason is that the static Hall conductivity for the continuum model is not properly regularized carrying an arbitrary residual value, thus it is not directly experimentally measurable but the difference in this quantity between different electronic states is. Since we know that the static part of the Hall conductivity in the NI phase is necessarily zero, we can directly obtain the residual conductivity to be $\sigma_{xy}^{(0)}$ in the NI phase. It is important to note that for the $J = 2$ 3D QAH phase, after subtracting

the residual conductivity, we obtain $\sigma_{xy}^{(0)}\Big|_{\rm QAH} \to \sigma_{xy}^{(0)}\Big|_{\rm QAH} - \sigma_{xy}^{(0)}\Big|_{\rm NI} = \frac{2e^2}{\hbar}\frac{k_{\rm c}}{2\pi^2}$, which is quantized and consistent with the lattice result. (In general, the static Hall conductivity is proportional to the chirality so that $\sigma_{xy}^{(0)}\Big|_{\rm QAH} \to \frac{Je^2}{\hbar}\frac{k_{\rm c}}{2\pi^2}$.) Note that the continuum model Hall conductivities presented in the figures throughout the chapter (both numerical and analytic results) have this residual conductivity subtracted. In this sense, we choose the momentum cutoff along the k_z direction as $k_{\rm c} = \pi/a$ so that the properly subtracted static Hall conductivity in the 3D QAH phase has the same quantized value as in the lattice model.

Similarly, we can obtain the dynamical part of the Hall conductivity, whose leading order contribution is quadratic in frequency, i.e., $\sigma_{xy}^{(2)} = \frac{e^2}{\hbar}B_{xy}\omega^2$. In the NI phase,

$$B_{xy}^{\rm NI} \approx k_0 \left(\frac{\hbar}{\varepsilon_0}\right)^2 \begin{cases} \frac{\alpha\gamma k_0^2-\varepsilon_0^2}{24\pi\sqrt{\alpha^3\beta k_0}} - \frac{\gamma k_0^2}{12\pi\sqrt{\frac{\beta\left(4\alpha\gamma k_0^2+\varepsilon_0^2\right)}{\gamma}}} & (J=1), \\ \frac{\gamma k_0}{48\pi\alpha^2}\sqrt{\frac{\alpha\left(\gamma^2 k_0^4+\varepsilon_0^2\right)}{\beta}} & (J=2), \end{cases} \tag{B.36}$$

whereas in the 3D QAH phase,

$$B_{xy}^{\rm QAH} \approx k_0 \left(\frac{\hbar}{\varepsilon_0}\right)^2 \begin{cases} \frac{k_{\rm c}\varepsilon_0^2}{96\pi^2 k_0\alpha(\alpha+\beta k_{\rm c}^2)} - \frac{\alpha\gamma k_0^2-\varepsilon_0^2}{24\pi\sqrt{\alpha^3\beta k_0}} & (J=1), \\ \frac{\gamma k_0}{48\pi\alpha^2}\sqrt{\frac{\alpha\left(\gamma^2 k_0^4+\varepsilon_0^2\right)}{\beta}} & (J=2), \end{cases} \tag{B.37}$$

where we take $k_c \to \infty$ limit for simplicity. Note that for $J = 2$, the dynamical part for the 3D QAH phase is given by the same form as that for the NI phase. In addition, $B_{xy}^{\rm NI}$ and $B_{xy}^{\rm QAH}$ are not zero, indicating that the system is a dynamical Hall insulator, even in the NI phase. Deep inside the NI (3D QAH) phase, however, $\lim_{\alpha\to\pm\infty} B_{xy} = 0$, thus the system becomes a trivial insulator (quantized Hall insulator) at finite frequencies.

Transition point

For the transition point between the NI and WSM phases or between the 3D QAH and WSM phases, $c_1 = 0$, $c_2 = \beta k_0^2$, $c_3 = \gamma k_0^2$ and $n = 2$. Then, the transverse optical conductivity is given by the following form:

$$\sigma_{xy}^{\mathrm{NI|WSM}}(\omega) = \frac{e^2}{\hbar}\left[A_{xy}^{\mathrm{NI}} + C_{xy}^{\mathrm{NI|WSM}}\omega^{\nu}\right], \tag{B.38a}$$

$$\sigma_{xy}^{\mathrm{QAH|WSM}}(\omega) = \frac{e^2}{\hbar}\left[\frac{Jk_{\mathrm{c}}}{2\pi^2} + A_{xy}^{\mathrm{NI}} + C_{xy}^{\mathrm{QAH|WSM}}\omega^{\nu}\right], \tag{B.38b}$$

where A_{xy}^{NI} is a residual conductivity for the NI phase given by $A_{xy}^{\mathrm{NI}}\big|_{J=1} = 0$ for $J = 1$ and $A_{xy}^{\mathrm{NI}}\big|_{J=2} = \frac{k_{\mathrm{c}}}{2\pi^2}\left(\frac{\gamma k_0^2}{\sqrt{(\gamma k_0^2)^2+\varepsilon_0^2}} - 1\right)$ for $J = 2$, as shown in Eq. (B.34). As discussed in Sec. B.1.2, the residual term A_{xy}^{NI} should be subtracted for the proper regularization. Here, the exponent $\nu \approx 0.5$ is found numerically from Eq. (B.26) for $J = 1, 2$ with frequency independent coefficients $C_{xy}^{\mathrm{NI|WSM}}$ and $C_{xy}^{\mathrm{QAH|WSM}}$, respectively.

B.2 Effects of the γ term, impurities, chemical potential and tilt

In this section, we discuss the effects of γ, impurities, chemical potential, and tilt on the optical conductivity, focusing on the validity of the characteristic frequency dependence described in this work. We show that the characteristic frequency dependence described in previous sections is not altered below the frequency corresponding to the energy scale of the tilt or impurity potential. Here, we limit our discussion to the range of frequencies below the energy scale that the lattice effect becomes important and the Weyl Hamiltonian is no longer valid.

B.2.1 γ term

In the main text, we obtained the power-law in the longitudinal optical conductivities assuming $\gamma = 0$ in the insulating phases [Eq. (4.12) in the main text] and at the

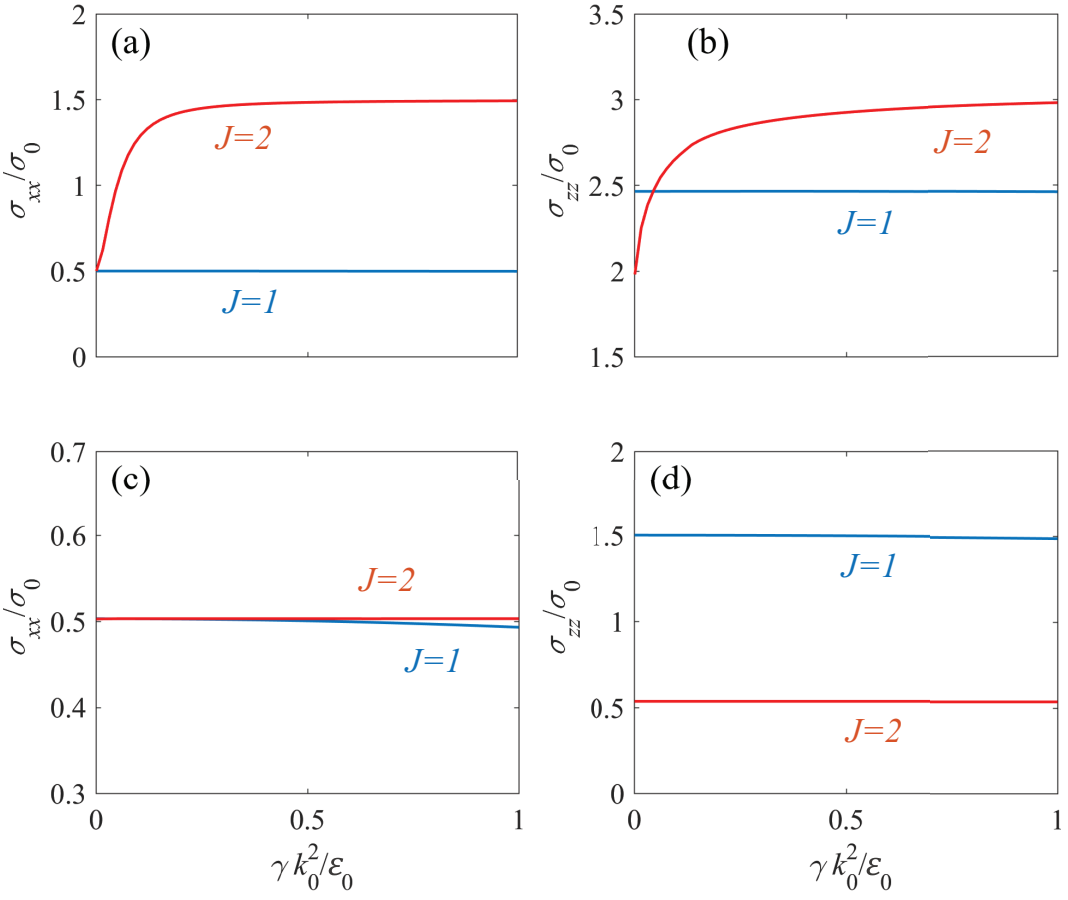

Figure B.1 Power-law exponent of σ_{xx} and σ_{zz} as a function of $\gamma k_0^2/\varepsilon_0$ (a), (b) in the NI phase and (c), (d) at the transition between the NI and WSM phases for $J = 1$ (blue) and $J = 2$ (red). For $J = 2$ in the NI phase, the deviation of the power-law from that obtained within the $\gamma = 0$ approximation is significant because the quadratic in-plane energy dispersion is comparable to the quadratic γ term.

transition point [Eq. (4.14) in the main text]. Figure B.1 shows the deviation of the power-law from that obtained within the $\gamma = 0$ approximation in the NI phase. For $J = 1$, the power-law is robust against the increase of γ because the linear in-plane energy dispersion dominates over the quadratic term associated with γ. For $J = 2$,

however, the deviation of the power-law is significant because the quadratic in-plane energy dispersion is comparable to the quadratic γ term. At the transition point between the NI and WSM phases, the power-law is barely altered by γ for both $J = 1$ and $J = 2$. The same conclusion holds for the QAH phase because the gapped band structure is similar to that of the NI phase, unless a Mexican hat structure appears. Thus, we find that the deviation from the $\gamma = 0$ approximation is significant in the gapped phases for $J = 2$ but not in the gapless phases which extend to low frequency.

B.2.2 Impurities

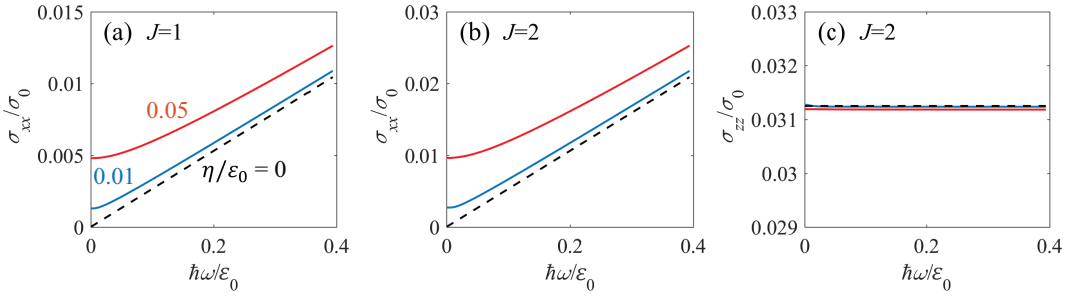

Figure B.2 Calculated longitudinal optical conductivities in the presence of disorder for (a) $J = 1$ and $J = 2$ in the (b) in-plane and (c) out-of-plane directions. Above the frequency scale set by the impurity potential, the characteristic frequency dependence presented in this work remains valid. Here, we set $\mu = 0$ and use several values of the broadening $\eta/\varepsilon_0 = 0, 0.01, 0.05$ for calculation.

The effect of impurities or disorder can be taken into account in a simple form as a finite broadening term η replacing the 0^+ term in Eq. (3.8) in the main text for the Kubo formula. Figure B.2 shows calculated optical conductivities for several values of η which characterizes the strength of the impurity potential. Impurities affect the power-law in the optical conductivity below the frequency range set by the energy

scale of the impurity potential. Above this energy scale, however, the characteristic power-law obtained in the clean limit remains valid. Note that simulating impurity effects with a broadening η is approximate, and strong enough disorder can induce a phase transition, which is beyond the scope of this work.

B.2.3 Chemical potential

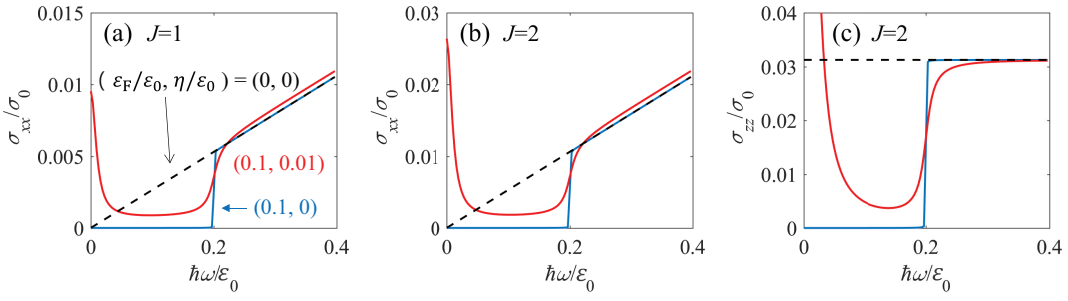

Figure B.3 Calculated longitudinal optical conductivities with chemical potentials $\mu = 0$ (dashed) and $\mu = 0.1\varepsilon_0$ (solid) for (a) $J = 1$ and $J = 2$ in the (b) in-plane and (c) out-of-plane directions. For finite μ, in addition to results with $\eta = 0$ (blue), we present results with non-zero $\eta = 0.01\varepsilon_0$ (red) to induce a Drude peak with a finite width due to impurities. Above the frequency set by the gap with a size of $2|\mu|$, the optical conductivity follows the characteristic frequency dependence described in the main text.

Chemical potentials of m-WSMs do not need to stay at a Weyl node, and they vary depending on materials. Figure B.3 shows calculated optical conductivities with zero and finite chemical potentials. As explained in the main text, a finite chemical potential μ away from a Weyl node produces a gap with a size of $2|\mu|$ due to Pauli blocking in interband transitions and a Drude peak near zero frequency from intraband transitions. Above the gap size, however, the optical conductivity follows the characteristic frequency dependence described in the main text.

B.2.4 Tilt

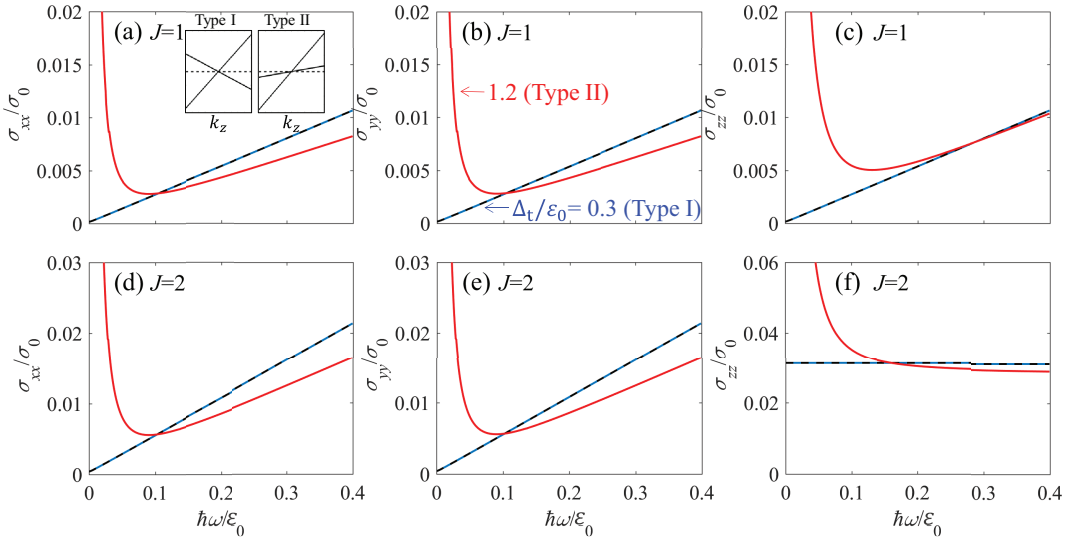

Figure B.4 Calculated longitudinal optical conductivities for (a)-(c) $J = 1$ and (d)-(f) $J = 2$ for several values of tilt $\Delta_t/\varepsilon_0 = 0$ (black dashed), 0.3 (blue solid), 1.2 (red solid). Insets to (c) and (d) show the energy dispersion along the tilt direction. Note that above the frequency set by the tilt energy scale, the frequency scaling of the conductivity described in this work remains valid. Here, $\eta = 0.001\varepsilon_0$ is used for the calculation.

In general, a Weyl node can be tilted breaking particle-hole symmetry. Figure B.4 shows the optical conductivity of tilted multi-Weyl nodes with a tilt term given by $H_t = \Delta_t \tilde{k}_x \sigma_0$ where $\tilde{k}_x = k_x/k_0$. For $J = 1$, tilt hardly affects the optical conductivity unless tilt is large enough that the system becomes type II [112] ($v_t > v_{\|}$ where $\Delta_t = \hbar v_t k_0$). When the system becomes type II Weyl semimetals, the Drude peak becomes significantly enhanced due to the formation of an electron-hole pocket whose size is comparable to the lattice scale ($\sim 1/a$). At sufficiently high frequencies, however, the optical conductivity recovers its original characteristic frequency behavior, as shown in Fig. B.4 (a)-(c). For $J > 1$, even small (linear in-

plane) tilt generates an electron-hole pocket changing the free carrier density of the system, modifying the characteristic frequency dependence below the frequency determined by Fermi energy of the electron-hole pocket created by the tilt. Above this energy scale, however, the frequency scaling of the conductivity described in this work remains valid.

Appendix C

Colllective modes in multi-Weyl semimetalst

C.1 Derivation of the long-wavelength polarization function for the isotropic model

In this section, we show the derivation of the analytical expressions for the zero-temperature polarization function and plasma frequencies in the $q \to 0$ limit. The polarization function for the isotropic model can be written as

$$\Pi(q,\omega) = g \sum_{s,s'=\pm} \Pi_{ss'}(q,\omega), \tag{C.1}$$

where

$$\Pi_{ss'}(q,\omega) = \int \frac{d^3k}{(2\pi)^3} \frac{f_{\boldsymbol{k},s} - f_{\boldsymbol{k}+\boldsymbol{q},s'}}{\hbar\omega + \Delta^{ss'}_{\boldsymbol{k},\boldsymbol{k}+\boldsymbol{q}} + i0^+} F^{ss'}_{\boldsymbol{k},\boldsymbol{k}+\boldsymbol{q}}. \tag{C.2}$$

Note that at zero temperature the Fermi distribution function is given by $f_{\boldsymbol{k},s} = \Theta\left(E_{\mathrm{F}} - E_{\boldsymbol{k},s}\right)$, where $\Theta(x)$ is the step function [$\Theta(x) = 0$ for $x < 0$ and $\Theta(x) = 1$ for $x \geq 0$]. We can break the polarization function into two parts due to intraband transitions and interband transitions, respectively: $\Pi(q,\omega) = \Pi_{\mathrm{intra}}(q,\omega) + \Pi_{\mathrm{inter}}(q,\omega)$,

where $\Pi_{\rm intra}(q,\omega)=\Pi_{++}(q,\omega)+\Pi_{--}(q,\omega)$ and $\Pi_{\rm inter}(q,\omega)=\Pi_{+-}(q,\omega)+\Pi_{-+}(q,\omega)$. For convenience, we use the change of variable $\boldsymbol{k}\to-\boldsymbol{k}-\boldsymbol{q}$ and introduce dimensionless quantities $x=k/k_{\rm F}, y=q/k_{\rm F}, z=\hbar\omega/E_{\rm F}$ and $\Pi(q,\omega)=D(E_{\rm F})\widetilde{\Pi}(y,z)$, where $D(E_{\rm F})$ is the density of states at the Fermi energy given by $D(E_{\rm F})=\frac{gk_0^3}{2\pi^2NE_0}(E_{\rm F}/E_0)^{(3-N)/N}$.

Then we can rewrite $\widetilde{\Pi}_{\rm intra}(q,\omega)$ and $\widetilde{\Pi}_{\rm inter}(q,\omega)$ as

$$\widetilde{\Pi}_{\rm intra}(y,z)=\frac{N}{2}\int_0^1 x^2dx\int_0^\pi\sin\theta d\theta\left(\frac{1}{z-\Delta_+}-\frac{1}{z+\Delta_+}\right)F_+ \tag{C.3}$$

and

$$\widetilde{\Pi}_{\rm inter}(y,z)=\frac{N}{2}\int_1^\infty x^2dx\int_0^\pi\sin\theta d\theta\left(\frac{1}{z-\Delta_-}-\frac{1}{z+\Delta_-}\right)F_- \tag{C.4}$$

where $\Delta_\pm=(x^2+y^2+2xy\cos\theta)^{\frac{N}{2}}\mp x^N$. In the $q\to0$ limit $(z\pm\Delta_\pm)^{-1}\approx z^{-1}\left[1\mp\frac{\Delta_\pm}{z}\pm\left(\frac{\Delta_\pm}{z}\right)^2+\cdots\right]$ and $\Delta_\pm\approx(x^N\mp x^N)+N\cos\theta x^{N-1}y+\frac{1}{2}N\left\{1+(N-2)\cos^2\theta\right\}x^{N-2}y^2+\cdots$. In the presence of chirality the overlap factor is given by $F_\pm=\frac{1\pm\cos\theta'}{2}\approx\frac{1\pm1}{2}\mp\frac{\sin^2\theta}{4x^2}y^2+\cdots$, where $\cos\theta'=\frac{x+y\cos\theta}{\sqrt{x^2+y^2+2xy\cos\theta}}\approx1-\frac{\sin\theta^2}{2x^2}y^2$ whereas in the absence of chirality $F_+=1$ and $F_-=0$. By putting all these equations into Eq. (C.3) and expanding up to the second order in y, we can obtain the long-wavelength polarization function. For the intraband part $\widetilde{\Pi}_{\rm intra}(y,z)$, the polarization functions for the chiral and non-chiral cases are the same up to the second order, given by

$$\widetilde{\Pi}_{\rm intra}(y,z)\approx\frac{N}{2}\int_0^1 x^2dx\int_0^\pi\sin\theta d\theta\frac{2\Delta_+}{z^2}F_+=\frac{N^2y^2}{3z^2}+O(y^3). \tag{C.5}$$

For the interband part $\widetilde{\Pi}_{\rm inter}(y,z)$, note that there is no interband contribution for the non-chiral case due to the absence of interband transitions ($F_-=0$). For the chiral case, $F_-\approx(\sin^2\theta/4x^2)y^2$ and when we expand the integrand only up to the second order, we can approximate $\Delta_-=2x^N$, yielding

$$\begin{aligned}\widetilde{\Pi}_{\text{inter}}y,z) &= \frac{N}{2}\int_1^\infty x^2dx\int_0^\pi \sin\theta d\theta\left(\frac{4x^N}{z^2-(2x^N)^2}\right)\frac{\sin^2\theta}{4x^2}y^2+O(y^3)\\ &= \frac{2Ny^2}{3}\int_1^\infty dx\frac{x^N}{z^2-4x^{2N}}+O(y^3)\\ &= -\frac{N\,{}_2F_1\left(1,\frac{N-1}{2N};\frac{3N-1}{2N};\frac{z^2}{4}\right)}{6(N-1)}y^2+O(y^3)\text{ for }z<2,\end{aligned} \tag{C.6}$$

where ${}_2F_1\left(a,b;c;z\right)=\frac{\Gamma(c)}{\Gamma(b)\Gamma(c-b)}\int_0^1 dt\frac{t^{b-1}(1-t)^{c-b-1}}{(1-tz)^a}$ is the hypergeometric function, which can be obtained after substituting $t=x^{-2N}$.

Thus the full polarizability in the long wavelength limit ($q\to 0$) is given by

$$\widetilde{\Pi}^{\text{nch}}(y,z)=\frac{N^2y^2}{3z^2} \tag{C.7}$$

for the non-chiral case whereas

$$\widetilde{\Pi}^{\text{ch}}(y,z)=\frac{N^2y^2}{3z^2}-\frac{N\,{}_2F_1\left(1,\frac{N-1}{2N};\frac{3N-1}{2N};\frac{z^2}{4}\right)}{6(N-1)}y^2\text{ for }z<2 \tag{C.8}$$

for the chiral case. Note that the polarization function diverges when $N=1$ because a linear band dispersion leads to the divergence of the polarization function at infinite cut-off[113]. By putting Eq. (C.7) and Eq. (C.8) into the dielectric function in Eq. (5.5) in the main text, we arrive at the analytic expressions for the leading-order long-wavelength plasma frequencies given in Eq. (5.8) and Eq. (5.9) in the main text.

C.2 Derivation of the long-wavelength polarization function in the anisotropic model

In this section, we show the derivation of the polarization function for the anisotropic case. Here we consider only the non-chiral case, where the overlap factor is given by $F_+=1$ and $F_-=0$. Note that due to the anisotropic band structure it is no

longer convenient to normalize the polarization function with the density of states as in the isotropic case. Thus for the anisotropic case we normalize the polarization function by $\widetilde{\Pi}(\widetilde{\boldsymbol{q}},\widetilde{\omega}) = \Pi(\boldsymbol{q},\omega)/\mathcal{C}$, where $\mathcal{C} = \frac{g}{(2\pi)^3}\frac{k_0^3}{E_0}$, $\widetilde{\boldsymbol{q}} = \frac{\boldsymbol{q}}{k_0}$ and $\widetilde{\omega} = \frac{\hbar\omega}{E_0}$. In the following, for brevity, the momentum and energy without tilde are considered to be normalized by k_0 and E_0, as in the main text.

We consider the following coordinate transformation:

$$\begin{aligned} k_x &= (r\sin\theta)^{\frac{1}{J}}\cos\phi, \\ k_y &= (r\sin\theta)^{\frac{1}{J}}\sin\phi, \\ k_z &= r\cos\theta. \end{aligned} \tag{C.9}$$

Note that with this coordinate transformation the energy dispersion becomes linear: $E_\pm(r) = \pm r$. The Jacobian corresponding to this transformation is given by $\mathcal{J}(r,\theta) = \frac{1}{J}(r\sin\theta)^{\frac{2-J}{J}}\, r$.

For the non-chiral case, there is no interband contribution, thus we consider only the intraband contribution. With a similar procedure as in the previous section, we can write the polarization function for the in-plane momentum $q_\parallel$ along the y-axis and out-of-plane momentum q_z along the z-axis as

$$\widetilde{\Pi}(q_{\parallel,z},\omega) = \int_0^{E_\mathrm{F}} dr \int_0^{\pi} d\theta \int_0^{2\pi} d\phi \mathcal{J}(r,\theta)\left(\frac{1}{\omega - \Delta_{\parallel,z}} - \frac{1}{\omega + \Delta_{\parallel,z}}\right) \tag{C.10}$$

where

$$\Delta_\parallel = E_{\boldsymbol{k}+\boldsymbol{q}_\parallel} - E_{\boldsymbol{k}} = \sqrt{r^2\cos^2\theta + \left[(r\sin\theta)^{\frac{2}{J}} + 2q_\parallel \sin\phi (r\sin\theta)^{\frac{1}{J}} + q_\parallel^2\right]^J} - r \tag{C.11}$$

and

$$\Delta_z = E_{\boldsymbol{k}+\boldsymbol{q}_z} - E_{\boldsymbol{k}} = \sqrt{r^2 + q_z^2 + 2rq_z\cos\theta} - r. \tag{C.12}$$

In the $q \to 0$ limit, $(\omega \pm \Delta_{\parallel,z})^{-1} \approx \omega^{-1}[1 \mp \frac{\Delta_{\parallel,z}}{\omega} \pm \left(\frac{\Delta_{\parallel,z}}{\omega}\right)^2 + \cdots]$, $\Delta_z \approx q_z\cos\theta + \frac{\sin^2\theta}{2r}q_z^2 + \cdots$ and $\Delta_\parallel \approx A_1 q_\parallel + A_2 q_\parallel^2 + \cdots$ where $A_1 = J\sin\theta\sin\phi(r\sin\theta)^{\frac{J-1}{J}}$ and $A_2 = \frac{1}{4}J\sin\theta(r\sin\theta)^{\frac{J-2}{J}}\left[J\sin^2\phi(\cos 2\theta + 3) + 2\cos 2\phi\right]$.

By putting all these into Eq. (C.10), we get the following polarization functions:

$$\begin{aligned}
\widetilde{\Pi}(q_{\parallel},\omega) &\approx \int_0^{E_{\rm F}} dr \int_0^{\pi} d\theta \int_0^{2\pi} d\phi \mathcal{J}(r,\theta)\frac{2\Delta_{\parallel}}{\omega^2} \\
&\approx \frac{J\pi q_{\parallel}^2}{2\omega^2}\int_0^{E_{\rm F}} dr \int_0^{\pi} d\theta\, r\sin\theta(\cos 2\theta+3) \\
&= \frac{4\pi J E_{\rm F}^2 q_{\parallel}^2}{3\omega^2}, \qquad \text{(C.13)} \\
\widetilde{\Pi}(q_z,\omega) &\approx \int_0^{E_{\rm F}} dr \int_0^{\pi} d\theta \int_0^{2\pi} d\phi \mathcal{J}(r,\theta)\frac{2\Delta_{z}}{\omega^2} \\
&\approx \frac{4\pi q_z^2}{J\omega^2}\int_0^{E_{\rm F}} dr \int_0^{\pi} d\theta\ (r\sin\theta)^{\frac{2-J}{J}}\, r\left(\frac{\sin^2\theta}{2r}\right) \\
&= \frac{\pi^{\frac{3}{2}}\Gamma\left(1+\frac{1}{J}\right)E_{\rm F}^{\frac{2}{J}}}{\Gamma\left(\frac{3}{2}+\frac{1}{J}\right)}\frac{q_z^2}{\omega^2}. \qquad \text{(C.14)}
\end{aligned}$$

Here we use the relation $\int_0^{\pi/2} d\theta \cos^m\theta \sin^n\theta = \frac{1}{2}B(\frac{m+1}{2},\frac{n+1}{2})$ where $B(m,n) = \frac{\Gamma(m)\Gamma(n)}{\Gamma(m+n)}$ is the beta function. Note that linear terms in q_z vanish both in Eq. (C.13) and Eq. (C.14) due to the symmetry of the angular integrals. Combining Eq. (C.4) and the dielectric function in Eq. (5.5) in the main text, we arrive at the analytic expressions for the leading-order long-wavelength plasma frequencies given in Eq. (5.15) and Eq. (5.16) in the main text.

국문초록

위상 준금속에서는 물질의 전도띠와 원자가띠가 선이나 점을 이루면서 만난다. 두 띠가 만나는 지점에서 전자는 질량이 없는 디락입자처럼 행동하기 때문에 디락 물질에서는 기존 물질에서 볼 수 없는 많은 특이한 현상이 나타나게 된다. 본 논문에서는 이러한 디락 물질의 물리적 특성에 기인한 물리적 현상에 대하여 연구하였다.

첫째로 다중 바일 준금속과 선마디 준금속의 광학적 특성에 대해서 연구하였다. 선마디 준금속의 광학적 특성이 페르미면의 기하학적인 구조 및 띠간 전이(interband transition)가 가능한 위상 공간(phase space)의 기하학적인 구조에 따라 크게 바뀔 수 있음을 보였다. 또한 저주파수 영역의 광학전도도의 멱급수 법칙이 페르미면의 구조에 따라 달라질 수 있음을 보였다. 다중 바일 준금속에서는 저주파수 영역에서 광학전도도의 멱급수 법칙이 감음수에 따라 바뀜을 보였다. 결과가 실험적으로 관측될 수 있음을 논의하였고 해당 관측 결과가 광학실험에서 디락 물질의 구조를 파악하는데 중요한 지표가 될 수 있음을 제시하였다.

또한 본 논문에서는 디락 물질내에서 일어나는 상호작용에 의해서 나타나는 현상에 대해서 연구하였다. 특히 플라즈몬 및 플라즈몬과 포논의 결합에 대해서 연구하였다. 우선 다중 바일 준금속에서 플라즈몬이 갖는 특성을 Random Phase Approximation 를 이용하여 얻었다. 이를 통해 다중 바일 준금속의 카이럴리티(chirality)가 플라즈몬 주파수를 적색편이 시킬 수 있음을 보이고 그 결과로 다중 바일 준금속에서 플라즈몬의 란다우 감소(Landau damping)이 일어나지 않음을 보였다. 또한 그래핀의 플라즈몬과 그래핀 기판의 표면 포논이 결합하였 때 생겨나는 준입자 산란에서의 변화에 대해서 연구하였다. 그 결과 플라즈몬-포논 모드의 방출을 통한 새로운 산란 매커니즘이 존재함을 보였다.

주요어: 광학전도도, 플라즈몬, 플라즈몬-포논 결합, 그래핀, 바일 준금속, 다중 바일 준금속, 선마디 준금

학번: 2012-20369